THE EFFECT OF SURFACE WETTABILITY ON FROST GROWTH AND DENSIFICATION ON FLAT PLATES

BY

AMNE EL CHEIKH

DISSERTATION

Submitted in partial fulfillment of the requirements
for the degree of Doctor of Philosophy in Mechanical Engineering
in the Graduate College of the
University of Illinois at Urbana-Champaign, 2013

Urbana, Illinois

Doctoral Committee:

Professor Anthony M. Jacobi, Chair, Director of Research
Professor Dimitrios Kyritsis
Research Professor Predrag S. Hrnjak
Professor Xinlei Wang

ABSTRACT

In addition to important factors like the surrounding air temperature and humidity, and surface temperature, frost growth and densification rates on cold, flat surfaces subject to forced convective heat and mass transfer depend on surface wettability and cooling rate during the condensation phase. If the cooling rate is high during the condensation phase, then the droplet distribution at incipient freezing is dominated by small droplets and a narrow size range. Conversely, if the cooling rate is low during the condensation phase, then the droplet distribution at incipient freezing follows established stationary distributions with a very wide range of droplet sizes. In the present study, the impact of the surface wettability is experimentally and analytically investigated for different cooling rates in the condensation phase.

Aluminum substrates, with coatings that have undergone conversion by plasma-polymerization to alter their wettability, are used to create surfaces that range from completely wetting to hydrophobic, with advancing contact angles as high as 110^{o}. The coated aluminum plates are then subjected to frosting conditions in wind tunnel experiments. The cooling rate during the condensation phase affects the frost thickness and density for hydrophilic and hydrophobic surfaces alike, with the low-cooling-rate condensation phase resulting in a thicker and denser frost layer—with differences exceeding 20% for thickness and density. When the frost growth is preceded by a high-cooling-rate condensation phase, the wettability effect on frost growth rate and densification is small. However, when frost growth is preceded by a low-cooling-rate condensation phase, a significantly denser frost layer grows on the hydrophilic surface. The impact of the surface wettability for a low-cooling-rate condensation phase remains

significant even after 2 hours of frosting. Repeated cycles of defrost and re-frost show the same behavior.

As part of the effort to more fully understand wettability effects on frost growth, a mathematical model is developed. The coupled heat and mass diffusion equations are solved numerically, with special attention directed toward the formulation of the initial and boundary conditions, and to modeling heat and mass transport within the frost layer. Unlike previous models reported in the literature, the current formulation does not erroneously assume saturation at the frost-air interface, nor does it require specification of the super-saturation ratio. Because it is extremely difficult to measure super-saturation at the frost-air interface, prescribing it as a boundary condition vitiates the utility of the model. In the current approach, the heat flux at the frost-substrate interface is specified to close the model. This approach results in a model with much more utility and flexibility. Initial conditions for frost density and thickness are obtained from the droplet distribution on the surface during the condensation phase, providing the first link between wettability and frost growth. The model assumes that the steady-state droplet distribution is achieved on the surface before freezing occurs; therefore, it is only applicable for a low-cooling-rate condensation phase. The model results for frost thickness and density are in good agreement with experimental data for surfaces with varying contact angles. This result makes it clear that the wettability effect on frost growth is primarily due to the distribution of condensate at incipient freezing. Interestingly, adapting the model to use initial conditions commonly adopted in the literature results in fairly good agreement with experiments conducted with a high-cooling-rate condensation phase. This result suggests that previous experiments have been predominately conducted with a high-cooling-rate condensation phase, obfuscating the effects of wettability.

TABLE OF CONTENTS

LIST OF FIGURES

LIST OF TABLES

LIST OF SYMBOLS

ENGLISH SYMBOLS

BF	Blowing Factor, $\ln(1+B)/B$	
B	Mass transfer driving force, $(m_s - m_w)/(m_w - 1)$	
D	mass diffusivity of water in air	(m^2/s)
h	heat transfer coefficient	(W/m^2·K)
h_m	mass transfer coefficient	(m/s)
h_{fg}	latent heat of fusion	(J/kg)
h_{sg}	latent heat of sublimation	(J/kg)
k	thermal conductivity	(W/m·K)
L	plate length	(m)
Le	Lewis number, α/D	(-)
m''	mass flux	(kg/m^2·s)
Nu	Nusselt number, $Nu = \frac{hL}{k_a}$	(-)
Pr	Prandtl number, ν/α	(-)
q''	heat flux	(W/m^2)
Sc	Schmidt number, ν/D	(-)
Sh	Sherwood number	(-)
T	temperature	(K)
U	Darcy velocity	(m/s)

GREEK SYMBOLS

α	thermal diffusivity	(m^2/s)
δ	frost thickness	(m)
ε	mass transfer conductance	(1/s)
ν	kinematic viscosity	(m^2/s)
Φ	porosity	(-)
ρ	density	(kg/m^3)
τ	turtuosity	(-)
ω	relative humidity	(-)

SUBSCRIPTS

a	air
fst	frost
lat	latent
ρ	density
δ	thickness
t	total
s	surface
sat	saturated
sens	sensible
v	vapor

CHAPTER 1

INTRODUCTION

1.1 Literature Review

Frost can grow on heat transfer surfaces that cool air below the freezing point of water, and the resulting frost layer can affect the performance of the heat exchanger. Frosting occurs in heat pumping and refrigeration applications, and frost on the heat transfer surface increases pressure drop (fan power) and decreases heat transfer, because the frost layer blocks the air flow and has a thermal conductivity much lower than that of the heat exchanger material. Energy efficiency is reduced by frost accumulation in these systems, and operation is complicated by the need to defrost the heat exchanger. Commonly, electric heaters or hot-gas from the compressor are used to melt the frost layer, and defrosting results in a further increase in energy consumption.

Many factors including air temperature, humidity, and surface temperature are known to affect frost growth on heat transfer surfaces. These factors have been thoroughly investigated by many researchers (Hermes *et al.* (2009), Lee *et al.* (1997 and 2003), Tao *et al.* (1993), Yang *et al.* (2005), and others). In addition, surface wettability is known to play an important role during the early stages of the frosting cycle. Depending on the surface energy, droplets with different shapes condense and freeze on the surface, therefore causing a change in the frost structure. However, there are contradictions in the literature concerning the variation of the frost density with the surface contact angle. Nikulshina *et al.* (1979), Seki *et al.* (1984), and Hoke *et al.* (2004) found that a denser frost layer forms a hydrophobic surface rather than on a hydrophilic surface during the mature frost growth phase. However, Lee *et al.* (2004) and Shin *et al.* (2003) reported

that a denser frost layer grows on more hydrophilic surfaces. Some recent attempts to use super-hydrophobic coatings in order to make ice-phobic surfaces or delay the frost growth on a heat exchanger surface have been made.

1.1.1 Droplet Size Distribution during Condensation

Frost growth on a cold surface can begin in two ways: it can start with condensation which later freezes and then grows as a frost layer, or it can begin with direct ablimation to form a solid layer on the surface. Hoke *et al.* (2000) examined the early stage of the water vapor nucleation on a cold surface in order to determine the transition point from condensation-frosting to ablimation frosting. Three parameters were thought to control the deposition scenarios: cold surface temperature, contact angle, and degree of saturation. Hoke *et al.* (2000) analyzed the conditions necessary for condensation or direct ice deposition based on the "classical" nucleation theory. Results showed that for ablimation on a clean glass surface, the substrate temperature has to be below -33°C and the absolute humidity ratio should be above 0.15 g/kg.

The condensation-frosting scenario occurs in heat transfer applications in which the cold surface temperature decreases gradually from the water dew point to the freezing point. This mode of operation prevails in heat pumping and refrigeration systems. Therefore, the size distribution of the water droplets condensing on the surface before freezing is important.

Condensate retention on flat surfaces has been widely studied. One of the most important conclusions from experimental observations is the existence of a "steady-state" (stationary) drop-size distribution. In steady state dropwise condensation, droplets may change location but the number of droplets of any diameter remains independent of time. Graham and Griffith (1973) experimentally measured the "steady-state" drop size distribution on a smooth vertical copper

surface of circular shape. However, due to technical difficulties, only drops down to 10 μm were counted and the distribution function below 10 μm was inferred from heat flux measurements. In their experiment, the total area covered by droplets on a 20 mm-diameter surface was 0.82, and the break-point between small drops that grow by condensation and big drops that grow by coalescence was taken as $0.2D_{max}$.

Rose and Glicksman (1973) proposed a model for drop size distribution. Starting from a configuration of randomly spaced, non-overlapping circles on a field of unit area, a growth rate is applied to each of the circles. Then, if the new generation had overlapping circles corresponding to coalescence, they are replaced by a droplet having the total volume of overlapping droplets and placed at their center of mass. The authors used three different initial configurations and three different growth rates and concluded that the area covered by all the circles reaches a steady value of 0.55.

Wu and Maa (1976) suggested a new model based on a population balance by defining death and birth functions that can be related to the growth rate. The model is based on an assumed steady and spatially uniform condensation and results in a total covered area by all drops of 0.9 assuming a maximum radius of 0.01 cm. Maa (1978) modified the model, recognizing that it applied only for small drops growing by direct condensation, and included the size distribution proposed by LeFevre and Rose (1965) to model the growth of big droplets by coalescence.

Another random fractal model was proposed by Wu *et al.* (2001) to simulate the spatial distribution of droplets during condensation in order to find the heat transfer rate during condensation. Unlike Rose's model (1973), the proposed model takes into account the non-

uniformity in the heat flux. The model was compared to experimental data for a wide range of pressure from 5 to 102 kPa.

1.1.2 Frost Growth on Flat Plates

As mentioned earlier, many factors affect the frost growth on flat plates. These factors have been extensively studied. Ostin and Anderson (1991) investigated the factors affecting frost growth on a horizontal plate in forced air streams. Their experiments showed a strong dependence of the frost thickness on the plate temperature and air humidity. However, increasing air velocity had a negligible effect on the frost thickness and mainly influenced the frost layer internally by increasing its density.

Another experimental investigation was undertaken by Han and Ro (1999) to study the frost growth on vertical plates. Measurements were obtained at 3 different locations on the plate (front, middle and rear) at various plate and air temperatures, humidities and Reynolds numbers. It was found that frost thickness and density were largest at the plate front and decreased toward the rear part of the plate. Frost thickness increased with increasing air temperature when the dew point was below 0°C and showed little dependence on the Reynolds number.

Hayashi studied frost growth experimentally and classified frost types into several groups based on their structures (1977). From experimental observations, frost formation was divided into 3 periods: “crystal growth period”, “frost layer period,” and “frost layer full-growth period”. In the “crystal growth period”, rod-type crystals start growing from the cold surface and form a non-homogeneous layer. Then, small branches are generated from the top of the rod-type crystals to form a more uniform layer during the “frost layer growth period”. Finally, as the frost thermal resistance increases, the frost surface temperature increases above the freezing point the top layer

starts melting. The melted water is absorbed into the frost layer which suddenly increases its density and therefore its thermal conductivity. Hayashi used this classification to model the effective thermal conductivity of the frost layer.

Tokura *et al.* (1983) measured the heat and mass transfer coefficients for an air flow over a frosted flat plate. Experimental results were compared to the empirical correlation of heat transfer coefficient for a laminar flow over a dry flat plate. The measured heat transfer coefficient was higher than the correlation prediction due to the surface roughness created by the frost layer. A correlation for the Sherwood number as a function of the Reynolds number was developed, and the heat and mass analogy was used to predict the Nusselt number. Experimental data for the Nusselt number satisfied the Chilton-Colburn analogy.

Mathematical models for frost growth prediction have been predominantly based on solving the heat and mass diffusion equations in the frost layer. They can be classified into two categories based on the boundary conditions used for the mass diffusion equation at the air-frost interface; saturation models and super-saturation models. Saturation models are based on the assumption that the outer edge of the frost layer, the frost-air interface, is at saturation conditions corresponding to the local moist-air conditions; super-saturation models do not impose this boundary condition, with the result that the frost-air interface is super-saturated relative to the local moist-air conditions. One of the earliest saturation models was proposed by Sherif *et al*. (1993). The model uses Euler's method to solve a differential equation for the frost thickness and temperature. The frost density was modeled as a function of the frost surface temperature only as Hayashi suggested. It is well-known that the frost density depends on other factors; however, this simplification is acceptable since the frost surface temperature depends on the same factors (air humidity, air temperature, cold plate temperature). Later, Lee *et al.* (1997) developed another

saturation model for frost formation on cold flat surfaces, based on the assumption that the amount of water vapor absorbed into the frost layer is proportional to the vapor density in that layer. With this simplifying assumption, an analytical solution for the water vapor density and temperature distribution in the frost layer was obtained under quasi-steady conditions. In order to account for frost thickness variation due to the moist air gradually decreasing in water-vapor content at it flowed downstream, the plate was divided into a regular grid. An analytical solution was obtained with the heat conduction and the diffusion equations for each segment of the grid, accounting for changes in moist-air properties along the flow direction. From the model, it was concluded that frost thickness and frost surface temperature increase with increasing air velocity and air relative humidity. Another conclusion, which was in agreement with O'Neal's findings, was that for velocities higher than 2 m/s the frost thickness was uniform along the plate.

Lee e*t al.* (2003) proposed a modification to their earlier model, in which the boundary layer partial differential equations with appropriate boundary conditions are solved for air temperature, humidity, and velocity. The model succeeded in predicting the density of the frost layer to within 10% when compared to experimental data. A significant variation in the frost thickness and density was found between the inlet and the outlet of the channel flow. Cheng and Cheng (2003) suggested a new modification to the previous model (Lee *et al.* 1997) by including the experimental correlation for frost density that was suggested by Hayashi (1977). Similarly, Fossa and Tanda (2002) developed a saturation model that solves for the frost density using Hayashi's correlation, but does not assume that the amount of water vapor absorbed at any location is proportional to the water vapor density. Hermes *et al.* (2009) adopted a similar approach by introducing a new correlation for frost density that is derived from Hayashi's widely used correlation: $\rho_f = 0.227 \exp\left(650 T_{fst,s}\right)$. The new correlation was found to be more

accurate since it includes the dependence of the frost density on both the cold-plate temperature and the frost surface temperature: $\rho_f = a \exp\left(bT_{fst,s} + cT_p\right)$. Results predicted by the model were in good agreement with experimental data. In this work, the plate surface temperature was found to be the most influential factor in the frost layer growth and densification phenomena. Yang and Lee (2005) assumed used another empirical for frost density that includes the effect of many parameters including air velocity, temperature, and humidity, and plate and frost surface temperatures. The main advantage of this approach is that it does not require the knowledge of an initial frost density.

More recently, Na and Webb (2004) performed a laminar boundary layer analysis to ostensibly prove that water vapor at the frost surface is super-saturated not saturated as many other researchers assume. However, their analysis neglects convection and assumes the temperature and concentration profiles in the frost layer are linear. No support for this simplifying assumption was provided. An empirical correlation for the degree of super-saturation at the frost surface as a function of the vapor pressure in the surrounding air and the saturation vapor pressure was found from related experiments. This correlation was used in a super-saturation model by Na and Webb (2004). Initial conditions for frost density and thickness were taken to be 30 kg/m^3 and 20 μm, respectively, as recommended by Jones and Parker (1975). The maximum and minimum frost conductivities were calculated using the 2 limiting models (parallel model and series model). In both models, it is assumed that the frost layer consists of parallel layers of ice and air. For the series model, the ice and air layers are connected in series with regard to the direction of the heat flow. In the parallel model, the layers are connected in parallel arrangement. Then, a new classification of frost types as a function of cold plate

temperature was suggested and used to find a weighing factor to model the variation of frost conductivity between its minimum and maximum values.

Another analysis based on simple models for saturation and super-saturation was performed by Lee and Ro (2005). The saturated model was based on the assumption that the frost-air interface was saturated. The results of this model were in good agreement with experimental data. On the other hand, the super-saturated model was based on an assumption that the frost layer was super-saturated. This approach is more complicated than the saturated model since it requires the knowledge of two important parameters: the degree of super-saturation and the diffusion factor. The degree of super-saturation was used to determine the total mass flux of water-vapor from moist air to the frost layer, while the diffusion factor was used to determine the contribution of the total mass flux to the densification and growth of the frost layer. Different expressions for the diffusion coefficient were investigated to determine which agreed best with experimental data.

Although the argument for super-saturation put forward by Na and Webb is not flawless, it is compelling. Nevertheless, the saturation assumption is still being used, largely because of a lack of clarity in how to prescribe the degree of super-saturation degree at the frost surface. Na and Webb correlated the degree of super-saturation to the actual and saturation vapor pressures of the surrounding air and the saturation vapor pressure at the frost surface temperature ($S_{fs} = 0.808\left(P_{v,\infty}/P_{vs,\infty}\right)\left(P_{vs,fs}/P_{vs,\infty}\right)^{-0.657} - 1$). However, Kandula (2011) suggested that the degree of super-saturation depends on other factors, such as the surface wettability, and therefore found the saturation boundary condition more convenient. In Kandula's model, a correlation for frost density as a function of frost surface temperature and Reynolds number was combined with the governing heat diffusion equation in the frost layer. The resulting partial differential equation

for frost thickness variation with time and location was solved with appropriate initial conditions. The model was compared to data of Yonko and Sepsy (1976), Cheng and Wu (2003), Lee *et al.* (1997), and Hermes *et al.* (2009) and showed good agreement except during the frost crystal growth period. The poor agreement was attributed to the uncertainties in the frost density correlation used at early times in the frosting cycle.

The saturation boundary conditions are still widely used in the literature. One more recent work by Wang *et al.* (2012) suggested a model similar to the one by Lee *et al.* (1997) with a new method to find the initial condition for frost density. The authors claimed that the proposed correlation for initial frost density is more general than Hayashi's widely used correlation since it takes into account three factors; the air, plate, and frost surface temperatures.

1.1.3 Effect of the Surface Wettability on the Frost Growth on Flat Plates

There has been considerable interest in understanding the effect of surface wettability on the frosting process. Seki *et al.* (1984) were among the first to investigate the effect of contact angle on frost growth. Using an experimental approach to the problem, it was concluded that a denser frost layer grew on the more hydrophobic surface (contact angle 110°) as compared to the more hydrophilic surface (contact angle of 43°). Other factors like air humidity and plate surface temperature were also considered. Frost thickness increased faster in more humid environments and for lower surface temperatures. On the other hand, air velocity and temperature were found to have negligible effects on the frost thickness.

More recently, Shin *et al.* (2003) undertook an experimental study to understand the effect of the surface hydrophilicity on frost density and thermal conductivity. Dynamic contact angle measurements were used to characterize the tested surfaces. Three samples of dynamic

contact angles 23°, 55°, and 88° were tested, and frost properties were correlated with time and dynamic contact angle. Results mainly showed a higher frost thickness and lower density on the more hydrophobic surface. However, the difference was only significant over an average duration of 120 minutes.

Hoke *et al.* (2004) proposed a mathematical model that included surface wettability effects on frost growth. The model consists of the energy and mass conservation equations within the frost layer and an expression by Bauer (1993) for the effective conductivity of a fibrous media based on porosity and the average orientation of fibers. Average fiber orientations of 45° and 65° showed good agreement with experimental data for hydrophilic and hydrophobic substrates, respectively. However, in contrast to the conclusions by Shin *et al.* (2003), the frost thickness on the hydrophilic substrate was 23% higher and the frost density 14% lower than on the hydrophobic substrate.

Lee *et al.* (2004) developed frost maps for surfaces with two different wettabilities (23° and 88° dynamic contact angles). In this study, frost was divided into several categories: feather-type, grass-type and plate-type and conditions for each type were specified. Furthermore, it was found that the more hydrophilic surface, having a lower contact angle, shows a lower frost thickness and a higher frost density than the hydrophobic surface.

Kim *et al.* (2011) also adopted an empirical approach to study the effect of the surface contact angle on the frost thickness and density. Experiments were conducted with three surfaces: a bare aluminum surface (CA=75º), a hydrophilic surface (CA=2.5º) and a hydrophobic surface (CA=142º). Frost retardation was observed for the hydrophobic surface but it was not significant. The frost density was higher on the hydrophilic surface and its thickness was lower. Also, less water was retained on the hydrophilic surface after defrosting. However, contrary to

the results by Shin *et al.* (2003), the difference in frost density and thickness remained same even after 120 minutes of the frosting cycle. The difference in defrosting time was found to be insignificant.

1.1.4 Effect of the Surface Wettability on the Frosting of Heat Exchangers

Frosting occurs in heat pumping and refrigeration applications, and frost on the heat transfer surface increases pressure drop (fan power) and decreases heat transfer, because the frost layer blocks the air flow and has a thermal conductivity much lower than that of the heat exchanger material. Many researchers investigated the possibility of altering the surface wettability of the fin surface to retard the frost growth.

Huang *et al.* (2009) investigated the performance of a heat exchanger coated with a hydrophilic anti-frosting coating. The heat exchanger surface was prepared by acid pickling and chemical conversion to get rid of all the contaminants and ensure good adhesion of the coating to the surface. The coating powder, which consists of small particles of 1 micrometer was mixed with a varnish and sprayed to the surface. Experiments showed that the coated heat exchanger surface was free of frost deposition while the uncoated heat exchanger surface was covered by a dense frost layer. However, the performance of most hydrophilic coated heat exchanger degrades after each frosting/defrosting cycle. Therefore, the work was extended to investigate long-term performance of the coating by running repeated cycling tests for more than two months. Results showed that the structure of the frost layer growing on the coated sample was fragile which facilitates the defrosting process and makes it possible by simply applying an external force. In addition, the coating was still performing well at the end of the testing period. However, the arguments about the mechanism that makes the frost layer loose were unclear. One potential

argument could be that the coating absorbs water droplets and retains them in the liquid state even when the temperature drops to below freezing due to the effect of its hydrophilic agent. Nevertheless, the contact angle of the coating could not be measured since the coating surface was rough and liquid water tended to wick into the surface.

Jhee *et al.* (2002) compared the performance of 3 heat exchangers with bare aluminum, hydrophilic and hydrophobic surfaces. Experiments showed that the thermal performance of all three heat exchangers was similar. However, the hydrophobic heat exchanger had a higher defrosting efficiency. In addition, the coated heat exchangers both retained less water than the uncoated one.

Kim and Lee (2012) conducted wet and frosting experiments to compare the thermal-hydraulic performance of three louvered-fin heat exchangers with hydrophilic, hydrophobic and dual surfaces ("where the tube and right side of the fin had a hydrophilic treated surface, and the left side of the fin had hydrophobic treated surface"). The hydrophilic heat exchanger had the highest air-side pressure drop under frosting conditions. In contrast to the results by Jhee *et al.*, the hydrophobic heat exchanger had a lower reduction in heat transfer due to frost retardation. The dual-fin heat exchanger exhibited frost retardation only in the early stage of the experiment, and at the same time produced higher heat transfer rate than the hydrophilic heat exchanger.

More recently, Moallem *et al.* (2012) experimentally investigated the effect of hydrophilic and hydrophobic coatings on the frosting behavior of louvered-fin, microchannel heat exchangers. The frost layers growing on coated fins were clearly different in patterns and types and the frost thickness in front fin leading edges was different for various coated heat exchanger. However, air-side pressure drop was identical for all coils. Both coated heat exchangers had a 15% higher cooling capacity than the uncoated heat exchanger.

Cai *et al.* (2011) proposed a method for restraining frost growth by the use of a hygroscopic (glycerol coating) or a hydrophobic (car wax coating) coating. Experiments showed that frost appeared later on the coated surfaces and had a sparse distribution, lower height and less crystal aggregation. Also, the hygroscopic coating thickness significantly affects the frost height. Therefore, the authors recommended using hygroscopic or hydrophobic coatings for heat exchangers operating under frosting conditions.

1.1.5 Frost Thermal Conductivity

The literature is replete with expressions of frost thermal conductivity. Some are experimental correlations calculated using Fourier's law and based on the measurements of heat flux, temperature gradient and frost thickness. Many of those correlations express the effective frost thermal conductivity as a function of frost density (Ostin and Anderson (1991), Yonko and Sepsy (1967), Lee *et al.* (1997), Sanders (1974) and others).

In addition, theoretical models to predict the effective frost thermal conductivity were developed. Dietenberger (1983) studied the heat transfer mechanisms into the frost layer and provided a review of many existing models and arguments about their validity based on the assumptions taken for their derivation. Dietenberger proposed modeling the frost layer as a random mixture of ice cylinders and spheres. Based on this model, maximum and minimum thermal conductivity expressions were derived and a combined effective thermal conductivity was obtained from the random mixture model of Brialsford and Major. The final expression of thermal conductivity requires the knowledge of the proportion of the frost volume representing ice spheres and ice planes which was found from a curve fit to Pitman and Zuckerman data.

Sahin (1994) modeled the frost layer during the crystal growth period as an array of ice columns surrounded by moist air. The humidity of the air at any cross-section inside the frost layer was assumed to be equal to the saturation humidity at the corresponding temperature. In the proposed model, the frost conductivity not only depends on the frost density, but is also related to the diffusion coefficient of vapor inside the frost layer. Therefore, it depends on the air properties and the cold plate temperature. Higher plate temperature or air temperature results in a denser frost layer with higher thermal conductivity. Nevertheless, higher air humidity reduces the effective frost thermal conductivity due to a decrease in the frost density.

XiangHong (2008) assumed the frost layer is a porous medium in which ice crystals are the porous matrix and moist air is the fluid. The void spaces between the ice crystals were interconnected by pipes. Based on this model, an expression for frost thermal conductivity as a function of air and ice thermal conductivities, porosity, and tortuosity was derived. The proposed model is valid only for frost layers with porosity greater than 0.5, and frost density lower than 450 kg/m^3.

Many researchers performed dimensional analysis to find non-dimensional groups on which the frost thermal conductivity depends. Yang *et al.* (2005) summarized empirical frost property correlations developed earlier than their work in a table with their test conditions. They undertook a dimensional analysis from which it was concluded that the frost properties depend on the air humidity ratio, Reynolds number based on the plate length, Fourier number, and a dimensionless temperature ($T^* = T_a - T_{tp}/T_a - T_p$). Experimental data were used to develop empirical correlations for the non-dimensional frost thickness, density, surface temperature and thermal conductivity. In addition, correlations for the Nusselt and Sherwood numbers for the flow over a frosted flat plate were developed. The applicable range of the empirical correlations

is as follows: the air temperature of 5 to 15°C, air velocity of 1.0 to 2.5 m/s, absolute humidity of 0.00322 to 0.00847 kg/kg_a, and cooling plate temperature of -35 to -15°C.

Barzanoni *et al.* (2012) manipulated the mass and energy conservation equations in non-dimensional form to find a dimensionless group on which the frost properties on a cylinder depend. Then, the least-square error method was used to find the coefficients in the resulting equations. The non-dimensional frost density, thickness, surface temperature and thermal conductivity were related to the Reynolds number, Fourier number, dimensionless air temperature and humidity, and cylinder surface temperature. The frost thickness predictions using the proposed equation at 2 environmental conditions were 18% different than experimental data by Lee and Ro (2001).

Tokura *et al.* (1983) performed a dimensional analysis and correlated the frost thermal conductivity to three non-dimensional groups. The first term is the ratio of the latent heat to the sensible heat, the second represents the ratio of the mass of water vapor transferred to a surface of area x^2 during a time period τ to the mass of water contained in volume x^3, and the third is the Nusselt number. Two correlations were provided based on two groups of experimental data: *group A* measured at low ambient temperature and high humidity and *group B* at high temperature and low humidity.

1.1.6 Summary

In summary, frost growth and densification on a cold surface depends on many factors, mainly air velocity, temperature and humidity, and surface temperature. These factors have been extensively studied by many researchers, and the effect of each factor is well established in the literature. However, the surface wettability is an important parameter which has been neglected

in many studies. Manipulating the surface wettability can significantly affect the frost properties, and therefore understanding and quantifying its effect would help in designing evaporators under frosting conditions. The limited extant studies on this topic show contradictory results, with disagreement on the variation of frost density with the surface contact angle.

The literature is replete with empirical studies on the performance of heat exchangers coated with hydrophilic, hydrophobic or hygroscopic coatings. However, conflicting results exist about the effect of the coating on the thermal and hydraulic performance of the heat exchanger.

1.2 Objectives

The primary objective of this study is to develop a better understanding of the effect of surface wettability on the characteristics of the frost layer growing on a flat vertically oriented plate. This understanding can be used as a guideline for the design of heat exchangers operating under frosting conditions. In order to pursue this overarching goal, the following specific objectives were pursued:

- Investigate of the effect of the surface wettability on the frost growth and densification through experiments using chemically coated aluminum surfaces, with advancing contact angles ranging from complete-wetting to 110° at various initial cooling rates.
- Develop a mathematical model based on solving the heat and mass conservation equations with appropriate boundary conditions for a control volume around the frost layer. Unlike earlier saturation and supersaturation models, the new model will not impose saturation nor specify a degree of supersaturation. Instead, the new model will be based on a specified heat flux in order to find the density gradient at the surface.

- Include the effect of the surface wettability in the model by assuming the frost layer grows from a layer of frozen water droplets, the shape and distribution of which depends on the contact angle.
- Validate the model by comparing the frost thickness and density predictions to experimental results from surfaces that have differing contact angles.

1.3 Thesis Summary

Since the frost growth mechanism depends on many parameters (air velocity, humidity and temperature, cold plate temperature, and surface wettability), the parameter space is too large to be explored solely through experiments. Therefore, a mathematical model for frost growth and densification on flat plates was developed and validated experimentally.

In the next chapter, the surface wettability effect is experimentally investigated by testing treated aluminum plates in a wind tunnel. The advancing contact angle of the tested samples ranges from 0^{o} (complete-wetting) to 110^{o} (hydrophobic). In chapter 3, a droplet count on the various specimens described in chapter 2 is performed to obtain drop-size distributions. Then, experimental data on the droplet distribution are compared to the power-law curve fit provided by Graham (1973), which is widely used in the literature. In chapter 4, a mathematical model based on solving the heat and mass balance equations with appropriate boundary conditions is developed and its predictions of the frost density and thickness variation are compared to experimental data. The model assumes that condensation precedes the frost growth mechanism, and therefore, the surface wettability impact is included in the model through initial conditions for frost density and thickness. The summary and conclusions are presented in the last chapter.

1.4 Figures and Tables

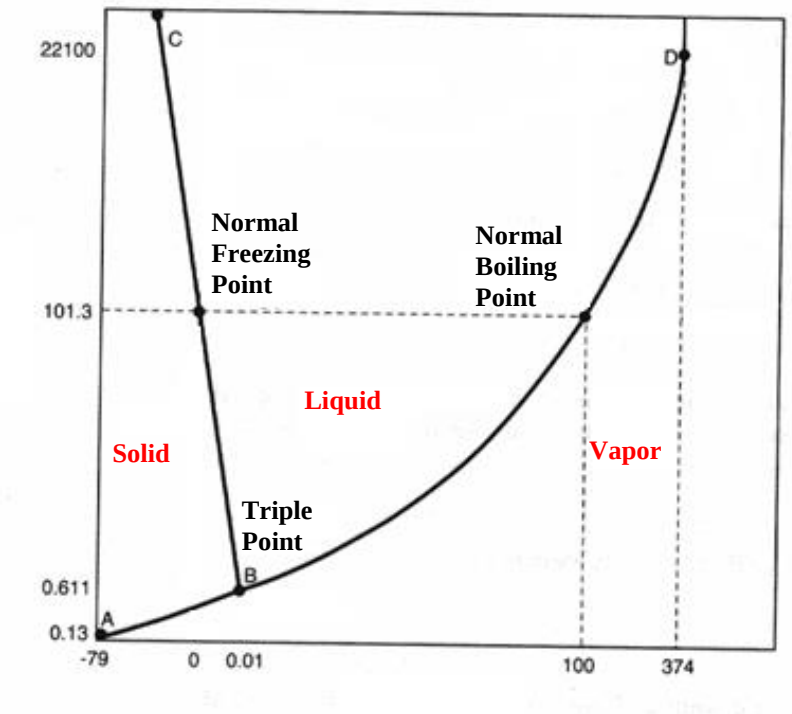

Figure 1.1 Phase diagram of water (Sciencetime, 2012)

CHAPTER 2

EFFECT OF SURFACE WETTABILITY ON THE FROST GROWTH ON VERTICAL FLAT PLATES

An experimental study to investigate the effect of the surface wettability on the properties of the frost layer growing on a flat vertical plate was undertaken. The specimens consist of aluminum plates chemically coated to manipulate their surface wettability. Experiments were conducted in a closed-loop wind tunnel at various air temperatures and humidities. Images of the frost layer were recorded in order to measure the thickness of the frost layer. The frost mass was recorded, and the frost density was computed based on the measured frost properties.

2.1 Experimental Methods

2.1.1 Description of Specimens

In this study, a total number of 4 aluminum plates of thickness 2 mm with different surface wettability were used in the experiments. Their distinguishing contact angles are presented in Table 2.1. The 4 specimens consist of a completely wetting, a hydrophilic, an untreated aluminum (Θ_A ~ 85° and Θ_R ~ 42°), and a hydrophobic surface. The hydrophilic/hydrophobic surfaces were prepared by inorganic conversion coating of a bare aluminum surface with hydrophilic/hydrophobic polymer sealer. The static, advancing and receding contact angles (Θ_S, Θ_A and Θ_R) were measured using a CAM200 (KSV Instruments) optical goniometer (accuracy of $\pm 0.5^0$) to characterize the surface wettability. The equilibrium contact angles were measured at different positions on these surfaces by the sessile drop method.

The method consists of placing a droplet with a specified volume (30 μl in this work) on the surface using a syringe, and taking side images of the droplet to trace its contour. The angle that the deposited droplet creates with the solid is the static contact angle of the surface. The advancing and receding contact angles were measured by initially placing a droplet of water on the surface, and then injecting water in or withdrawing water at a very small rate (0.3-0.5 μl/s). The standard deviations in the measurement of the advancing and receding contact angles were 4° and 8°, respectively.

2.1.2 Experimental Apparatus and Procedure

In order to investigate the effect of surface wettability on the frost growth on flat plates, frost was grown on aluminum surfaces placed in a closed-loop wind tunnel. A schematic of the experimental apparatus is shown in Figure 2.1. As the figure suggests, the airflow was conditioned with a precooler and a cool-mist humidifier to the desired temperature and humidity. A blower was used to draw the conditioned air flow through honeycomb flow straighteners and a 6:1 area contraction to the test section. A hydrostatic temperature bath was used to provide a coolant flow to a 20-mm thick aluminum plate of cross-sectional area 9x15cm. Small channels (D=5 mm) were drilled in the aluminum plate parallel to the 15cm length side. The channels were evenly spaced with 5mm spacing. The surface temperature at various locations on the plate was measured using 8 thermocouples (±0.15 ºC) and was found to be uniform within ±0.5ºC. The 2-mm thick specimen was secured to the thick aluminum chilled surface using double-sided thermal tape of thickness 0.16 mm and conductivity 0.7 W/m·K. A heat flux sensor (Omega HFS-3, ±5 W/m^2) with a thermal resistance 0.00176 K·m^2/W was secured between the chilled surface and the tested plate and used to measure the total heat flux transferred from the

surrounding air to the cold plate. The bottom and sides of the chilled aluminum surface were well insulated so that frost grew only on the tested sample. Then, the chilled plate was placed in the wind tunnel test section with a vertical orientation.

The airflow was circulated in the wind tunnel while bringing it to the desired temperature, velocity, and relative humidity. Steady-state prevailed when the temperature and relative humidity of the air flow entering the test section of the wind tunnel varied by 0.2ºC and 2% respectively for a period of at least 1 minute. The relative humidity of the air was measured upstream and downstream of the specimen using relative humidity data loggers (Omega, OM-62) (± 2%). In addition, 2 grids of 4 type-T thermocouples were used to measure the air temperature upstream and downstream of the test section. Since the tested sample area was small (6x4 cm), the effect of the heat transfer from the surrounding air to the frost layer on the air properties was insignificant, and the change in air temperature and humidity between upstream and downstream of the test section was less than 2%. The air velocity was measured using a hot wire anemometer (Omega, HHF2005HW) with an accuracy of ±5%.

After the air properties reached steady-state, the coolant flow was circulated inside passages drilled through the cooled aluminum plate. Initially, the plate temperature was decreased to below the water dewpoint and condensation occurred on the specimen. Two cooling schemes were investigated; a high and a low rate (Figure 2.2). When the cooling rate was high, small droplets condensed on the surface (for less than 1 minute), but plate temperature decreased fast to below freezing point. In that case, the initial layer of frost consisted of small droplets of nearly uniform sizes (with diameters less than 400μm) and shapes (Figure 2.3). On the other hand, when the cooling rate was very low, the condensation phase was relatively long (15

minutes) and the droplet distribution on the surface was allowed to reach steady-state, after which the number of droplets of each size remains fixed.

In the absence of an accurate method to calculate the time required to reach steady-state condensation, an estimate of the time required for a droplet to grow from the minimum to the maximum diameter was determined. Graham (1969) developed a relationship between the diameter, *D*, and the time, *t*, required for a droplet to grow by condensation (not taking into account the possibility of coalescence with neighboring droplets) from the minimum diameter to *D*.

$$1/2k\,(D^2 - D_{min}^2) + 2/h_i(D - D_{min}) = 4t\Delta T/\rho h_{fg} \qquad (2.1)$$

$$h_i = (2\alpha/(2-\alpha))(MW/2\pi\bar{R}T_s)^{0.5}\, h_{fg}^2/T_s v_g \qquad (2.2)$$

Where $\Delta T = T_s - T_w$

The term α in Equation 2.2 is called the condensation coefficient which was assumed to be independent of pressure and equal to 1 by Graham (1969). For condensation on a plate (with T_w=5°C) over which an airflow of temperature 15°C is flowing, it takes around 65 seconds for a droplet diameter to increase from 1μm to 3mm (assumed to be D_{max}). The steady-state drop size distribution on a surface is achieved after droplets grow by coalescence and direct condensation, and some droplets depart from the surface after they reach the critical droplet size D_{max}. Therefore, during the high-cooling-rate experiments, the condensation period was shorter than the time required for a droplet to reach the maximum diameter. On the other hand, during the low-cooling-rate experiments, condensation was allowed for more than 12 minutes to ensure that the steady-state drop size distribution is achieved on the surface.

The frosting period was assumed to start when all the droplets on the surface were frozen. Images of the frozen droplets on the surface were recorded in order to find the droplet distribution function required in the mathematical model (developed in chapter 3).

When frosting began, rod-type frost crystals started growing vertically on top of the frozen droplets and finally branches grew horizontally from the frost rods. The frost mass was recorded at regular intervals of 30 minutes using an electronic balance (±0.001g), and images of the frost layer were recorded to find the frost thickness. The frost mass and thickness measurements were used to calculate the frost average density variation throughout the two-hour frosting cycle.

2.2 Data Reduction and Interpretation

As shown in Figure 2.4, image processing was used to trace the frost edge and the thickness of the frost layer was integrated along the plate length to find the average frost thickness (See Appendix A for details about the image processing procedure). The frost density was calculated by dividing the frost mass measured with a balance by the frost volume. Since the frost thickness variation along the plate was not significant during the mature frost growth period, the layer was assumed to have a uniform thickness. The frost volume was computed by multiplying the frost layer thickness by the plate surface area.

2.3 Results and Discussion

2.3.1 Effect of Cooling Rate on Frost Thickness and Density

The hydrophobic sample was tested under the conditions summarized in run 1 of Table 2.2. During the first experiment with a high cooling rate (HCR), the coolant solution temperature

was decreased to the desired plate temperature. Then, the solution was circulated inside the thick aluminum plate, so the tested plate temperature decreased fast. As shown in Figure 2.4, small droplets appeared on the surface and froze before they had the chance of growing by direct condensation or coalescence. The same scenario occurs in refrigeration applications where air temperature is below the water freezing point; therefore, making the condensation period short.

In contrast, the low-cooling-rate experiment required decreasing the coolant temperature slowly from room temperature to below the water dewpoint, then below freezing point (Figure 2.2). In this case, droplets condensing on the surface had enough time to coalesce and grow until steady-state condensation prevailed (Figure 2.5). This process closely simulates the frost growth process on an evaporator used in heat pumping applications.

As shown in Figures 2.6 and 2.7, the condensation-period cooling rate has a significant effect on the frost thickness and density. It can be concluded that the higher the cooling rate, the lower the resulting frost thickness and density. Allowing condensation to reach a steady-state drop-size distribution results in a higher initial frost thermal conductivity and a higher surface area of droplets having a wide range of diameters; this promotes mass transfer and results in a higher frost density.

2.3.2 Effect of Surface Wettability on Frost Thickness and Density

The surface wettability and cooling rate are two interrelated parameters that affect the frost growth on vertically oriented flat surfaces. Both parameters have a strong impact on the initial frost density and thickness determined through analyzing the initial layer of frozen droplets on the surface. In Figures 2.8 and 2.9, the variation of frost thickness and density respectively are plotted for all three tested surfaces at both cooling rates.

The effect of the cooling rate on frost density is significant for hydrophilic, hydrophobic and uncoated surfaces. However, its impact on frost thickness is less important. In addition, at high cooling rates, the wettability influence on both frost thickness and density is insignificant. At the high cooling rate, the initial frost layer consists of very small frozen droplets of approximately uniform size and distribution (Figure 2.4), unlike the low-cooling-rate case where larger proportion of the surface is occupied by big droplets (with diameter larger than 0.2 D_{max}) (Figure 2.5). Consequently, the role of the droplet shape is not important.

2.3.3 Effect of Repeated Cycling on Frost Thickness and Density

In most applications, periodic defrosting is used to melt the frost layer deposited on the heat transfer surface. Three common methods can be used to defrost an evaporator; off-cycle defrost, electric defrost and hot-gas defrost. The first method (off-cycle defrost) consists of simply turning off the refrigeration system while keeping the air flow, and therefore it is only useful when the air temperature is above the water freezing point. Electric defrost requires a special design of the evaporator incorporating passages through the fins where electric heaters are installed and used to raise the surface temperature above the freezing point. In the last method (hot-gas defrost), the refrigerant flow through the evaporator is interrupted and a hot gas is supplied instead to melt the frost layer. In the present study, a warm ethylene glycol and water solution was supplied through the passages of the 50-mm thick aluminum plate to increase the tested plate temperature. Therefore, the defrost process is similar to the hot-gas method, but using a liquid solution (ethylene glycol and water) with a lower temperature than a typical defrost gas supply.

Depending on the amount of heat supplied to the surface during defrosting, some residual water can remain on the surface at the beginning of the next frosting cycle. The defrosting process was carried out by supplying a solution of water and ethylene glycol at room temperature (22°C) through the same passages where coolant was supplied during the frosting process. The air supply was turned off and the defrosting process was terminated when all the frost had melted and the plate temperature reached a value of 5 °C. Limited experiments were conducted using the off-cycle defrosting method and no significant discrepancies in frost density and thickness during the second frosting cycles were found when comparing the two methods of defrosting.

As in the wettability experiments, the repeated cycling of frosting and defrosting was carried out for both the low and high cooling rates. As shown in Figure 2.10 and 2.11, at the low cooling rate (LCR), the cycle to cycle variations are very small. The main reason for this invariance in frost thickness and density with cycle is that condensation is allowed until the steady-state droplet distribution is achieved. Subsequently, the residual water on the surfcae from the previous cycle does not alter the distribution of frozen droplets on the surface at the beginning of the frosting cycle.

In contrast, at high cooling rate where condensation period is short, there are cycle to cycle variations in density and thickness. The water retained on the tested surface after defrosting freezes at the beginning of the second cycle causing a higher initial frost density, thermal conductivity and surface area of droplets (Figure 2.12 and 2.13). The surface wettability has a significant impact on the melt water drainage from the surface during defrosting. As shown in Figure 2.14 to 2.17, the cycle to cycle variations in frost thickness and density are less significant for the hydrophobic (sample 4) surface as compared to the uncoated surface (sample 3). Moreover, the cycle to cycle variations in frost properties on the complete-wetting surface

(sample 1) are insignificant (see Figures 2.13, 2.18, and 2.19). This result can be explained from the findings of Liu and Jacobi (2006) concerning the effect of surface wettability on water drainage and condensate retention on evaporators. Super-hydrophilic surfaces have an improved water drainage behavior due to filmwise manner of water retention; therefore, the impact of residual water on the surface from the previous frosting cycle is less significant for hydrophilic surfaces.

2.4 Conclusions

In this chapter, experimental data for frost mass, thickness, and density on vertically oriented flat surfaces with differing surface wettability were reported. The effect of wettability is isolated through a careful set of experiments. The significant experimental findings are summarized as follows:

(1) At a high cooling rate, the surface wettability effect on frost thickness and density can be neglected.

(2) At low cooling rates, a denser frost layer grows on more hydrophilic surfaces.

(3) Cycle-to-cycle variations of frost thickness and density are only important at a high cooling rate. An increase of 10% in thickness and 20% in density is observed from the first to second frosting cycle for the uncoated aluminum surface. However, the cycle to cycle variations are less significant for the hydrophobic surface with an 5% increase in thickness and 10% increase in density.

(4) The increase in frost thickness and density for the complete-wetting surface is insignificant to it improved water drainage behavior.

(5) Density and thickness changes from third cycle on become insignificant for all surfaces.

2.5 Figures and Tables

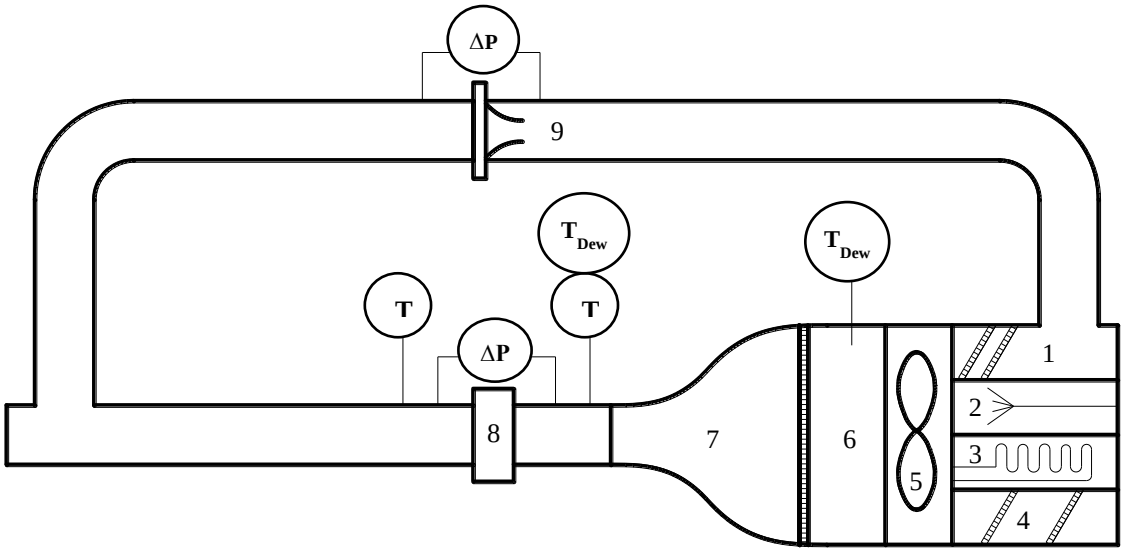

Figure 2.1a Experimental apparatus. (1- pre-heaters, 2- cool-mist humidifier, 3- pre-cooler, 4- after heaters, 5- blower, 6- mixing chamber, 7- contraction, 8- test section, 9- orifice plate)

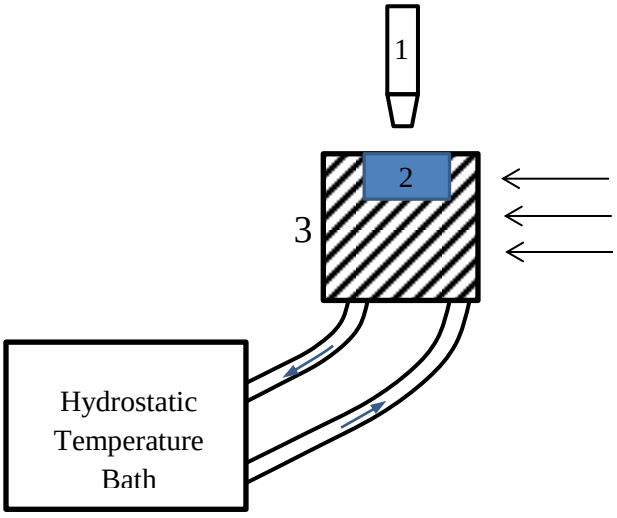

Figure 2.1b Test section (1- CCD camera used to take frost edge images, 2- tested sample, 3- insulated part of the chilled plate)

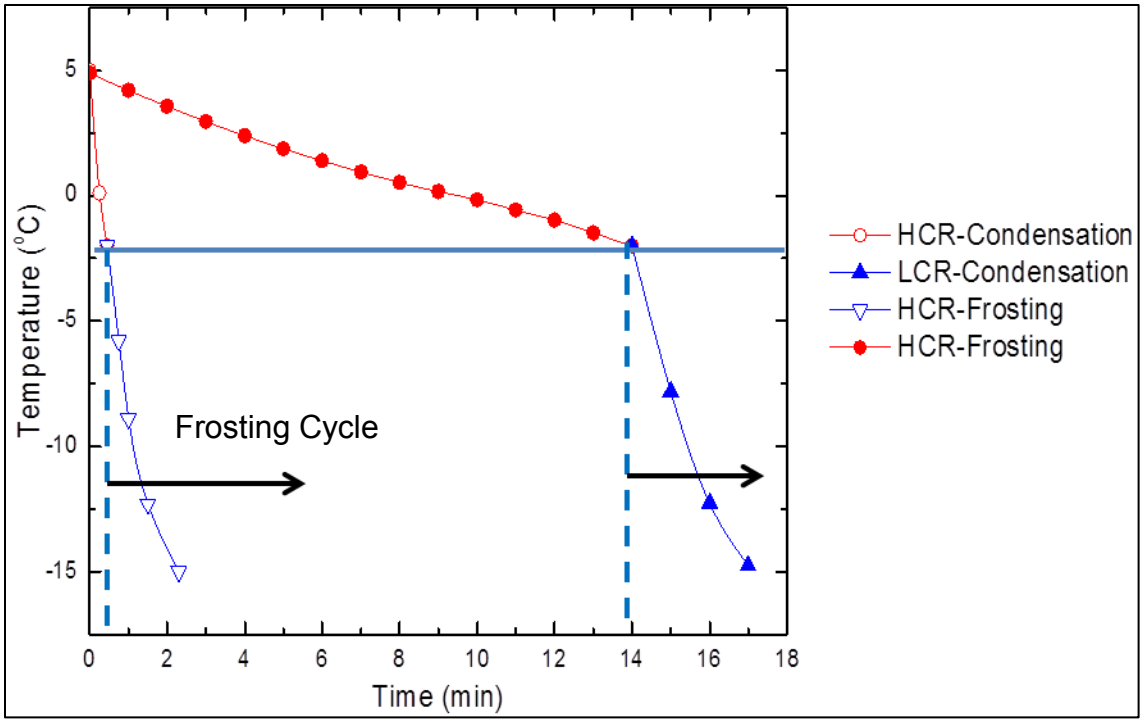

Figure 2.2 Variation of plate temperature with time at high and low cooling rates

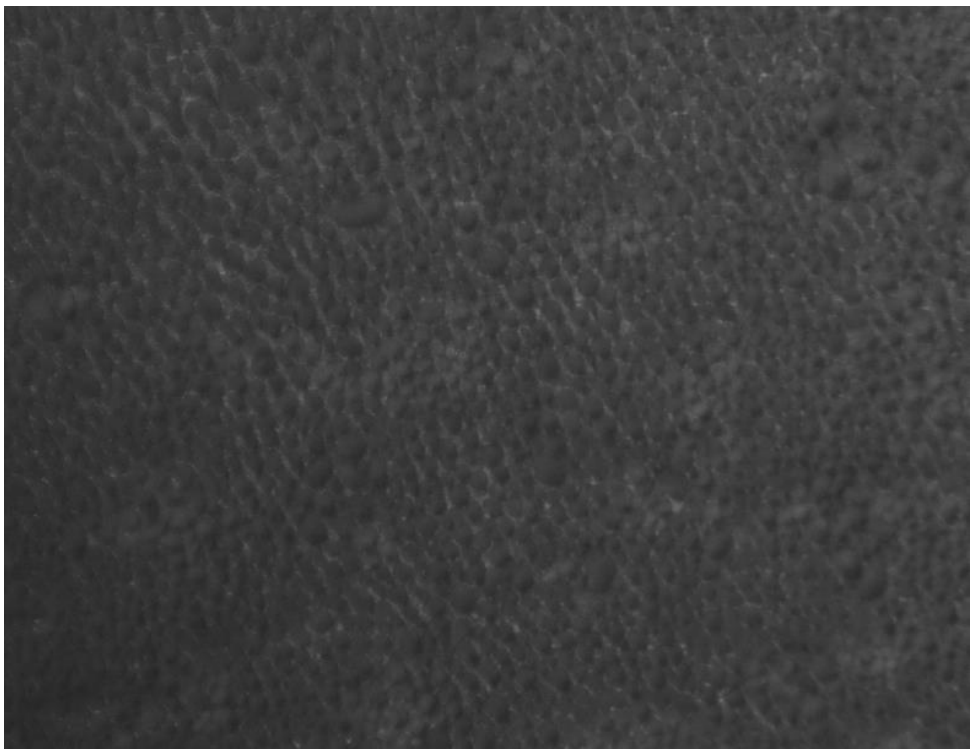

Figure 2.3 Frozen droplets on a hydrophobic sample at HCR

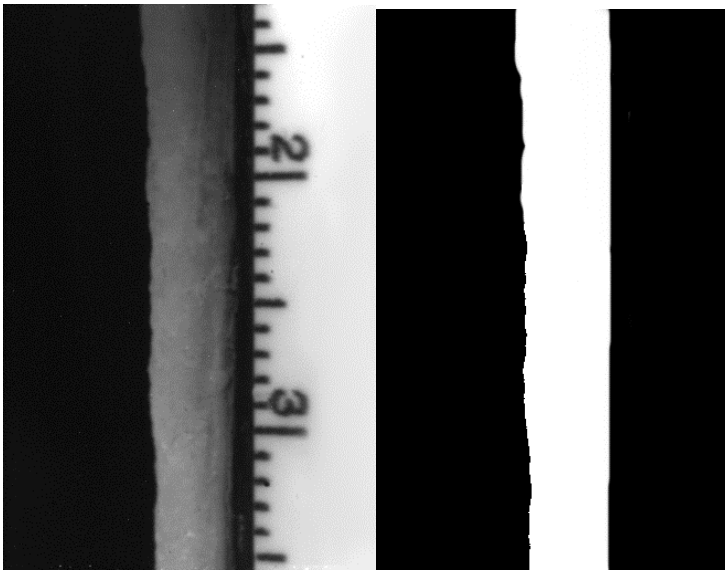

Figure 2.4 Original (left) and processed (right) frost thickness image

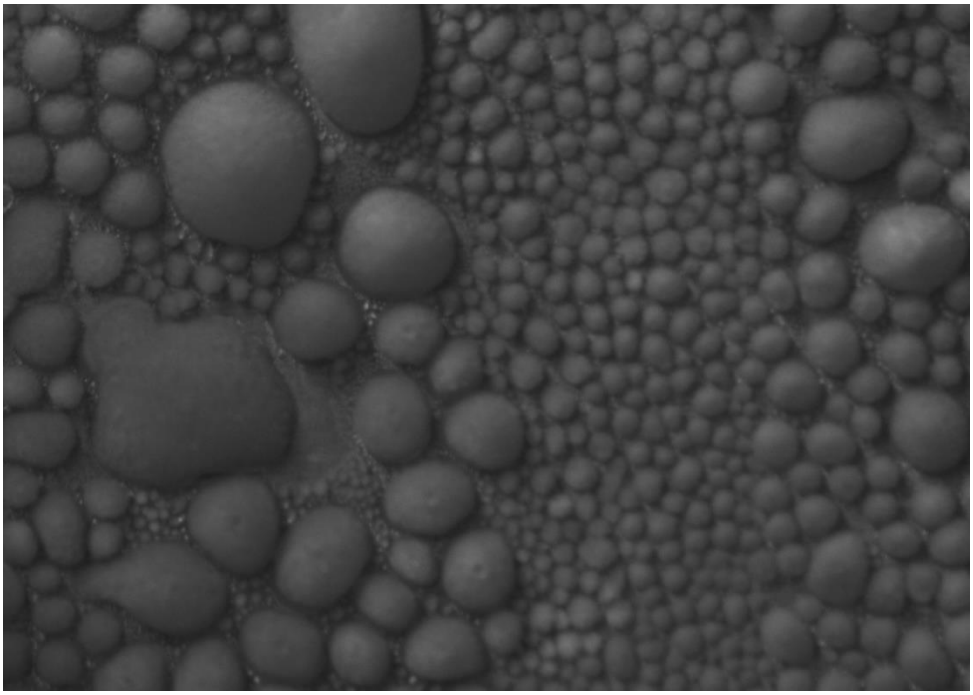

Figure 2.5 Frozen droplets on a hydrophobic sample at LCR

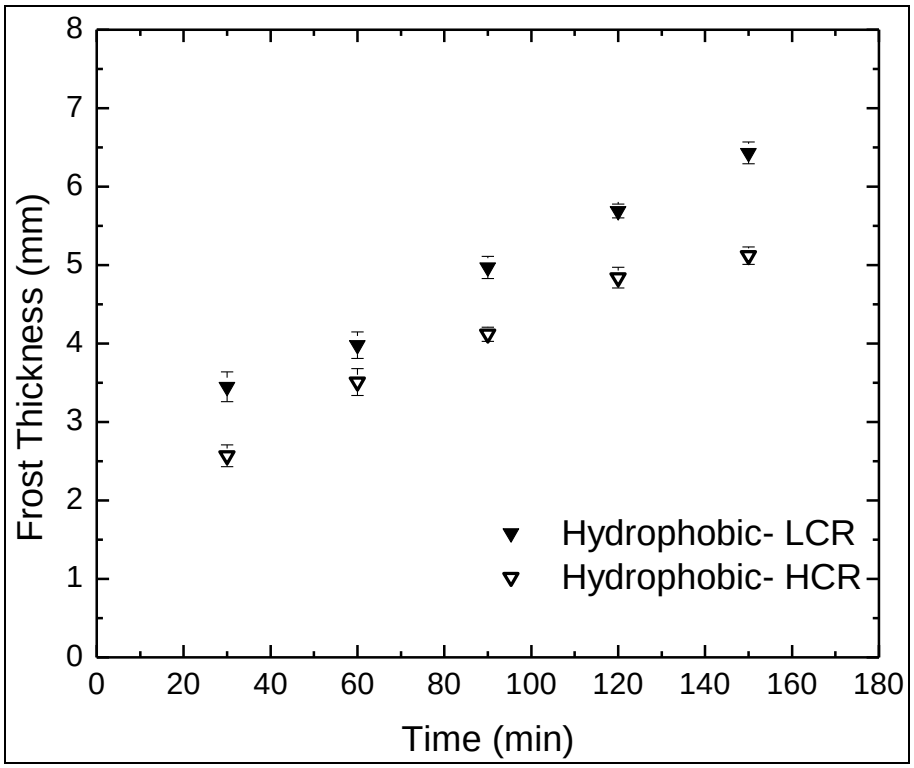

Figure 2.6 Effect of cooling rate on frost thickness at conditions of run 2 (Table 2.1)

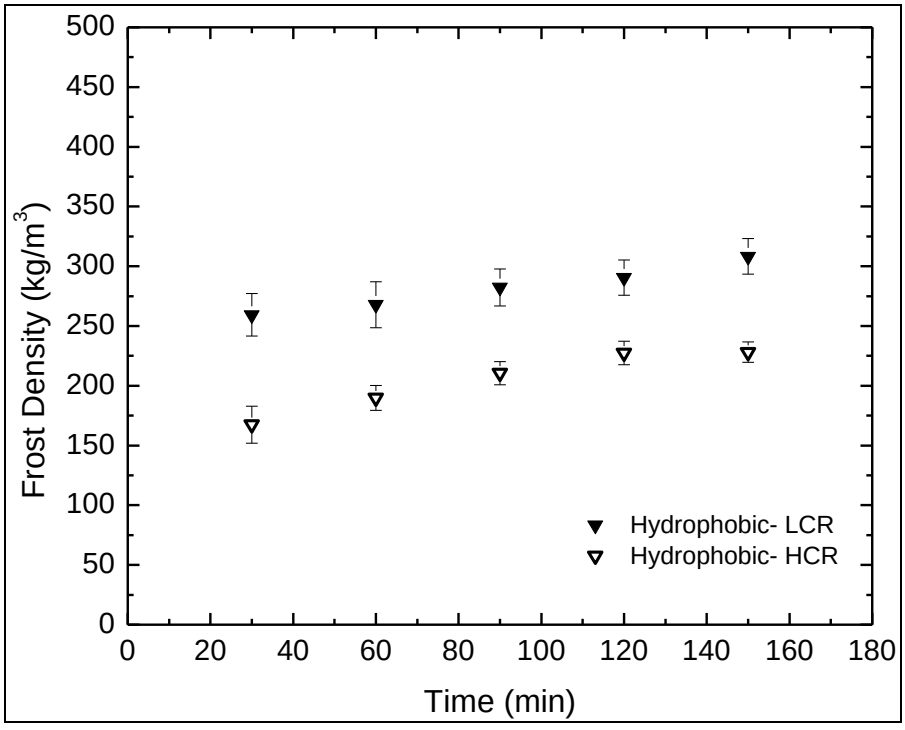

Figure 2.7 Effect of cooling rate on frost density at conditions of run 2 (Table 2.2)

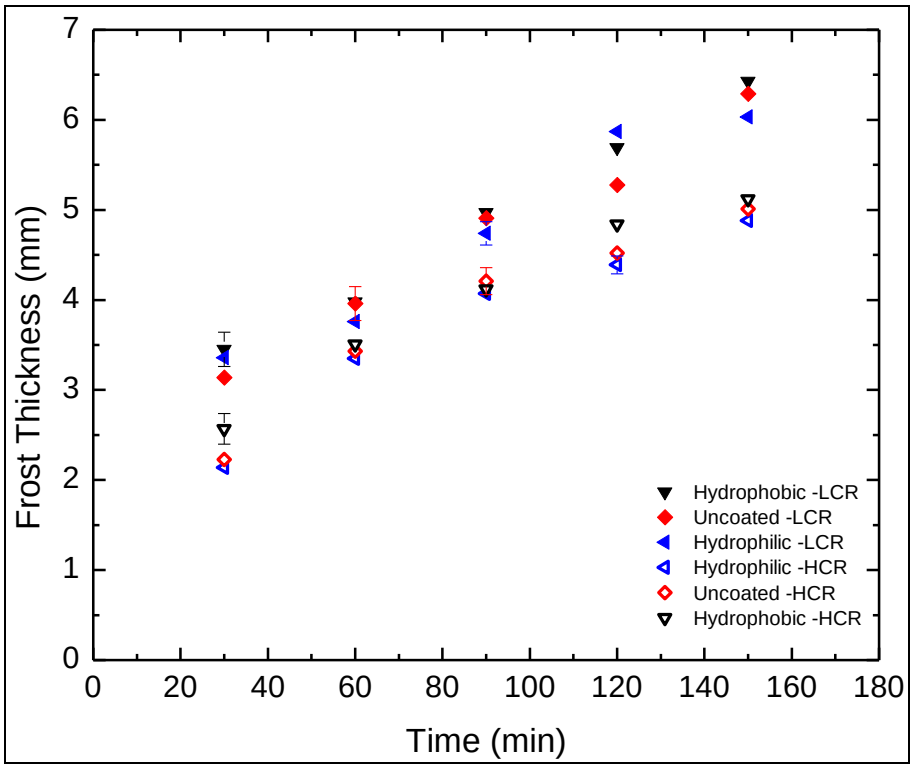

Figure 2.8 Effect of surface wettability on frost thickness at high and low cooling rates at conditions of run 1 (Table 2.2)

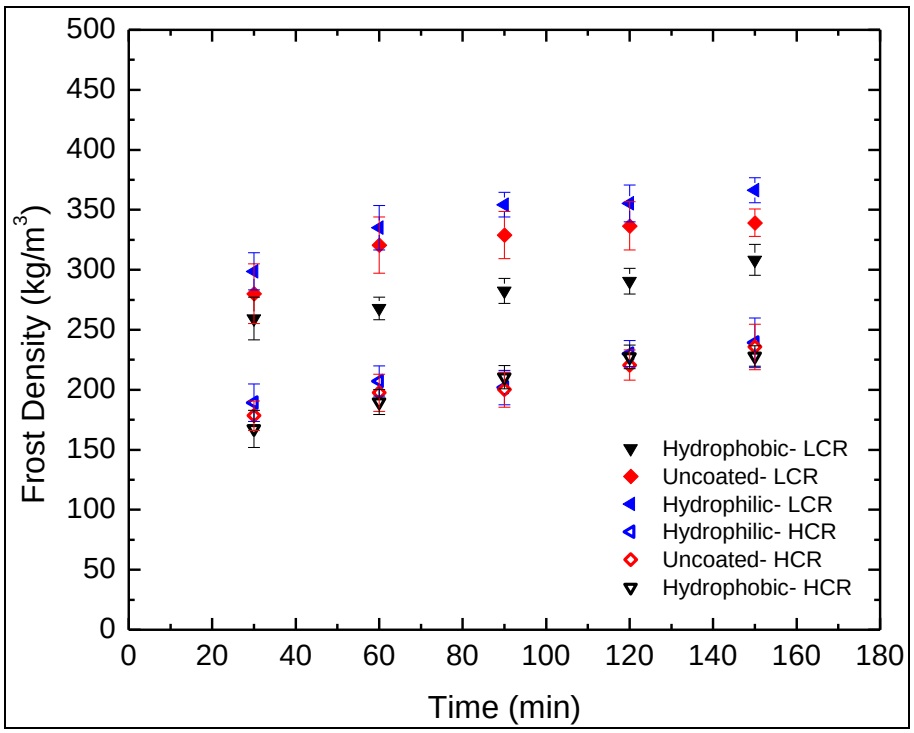

Figure 2.9 Effect of surface wettability on frost density at high and low cooling rates at conditions of run 1 (Table 2.2)

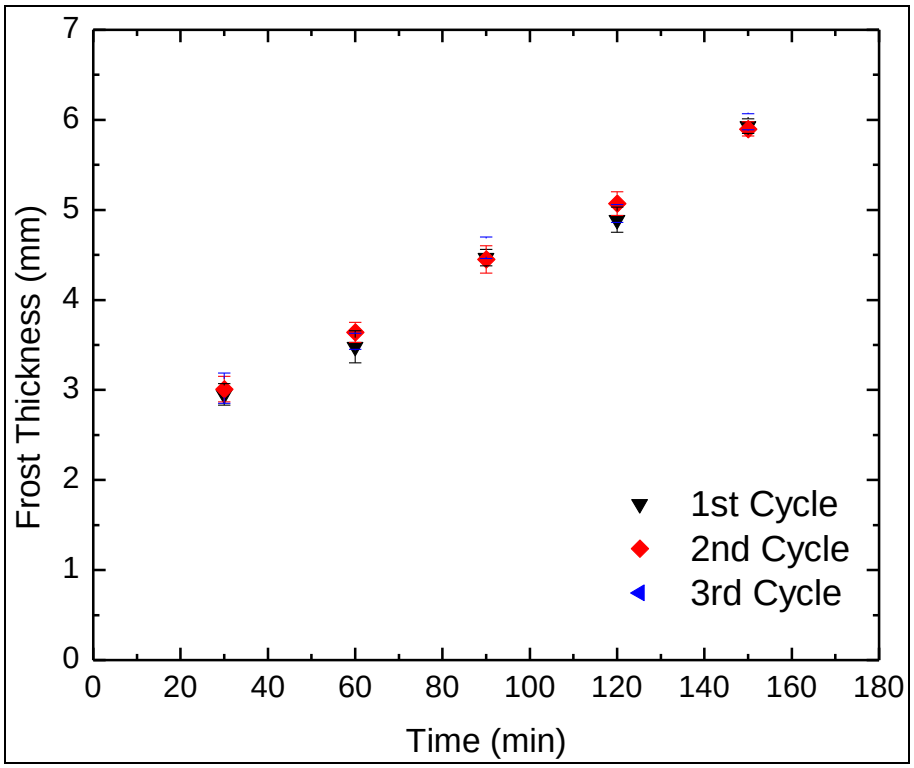

Figure 2.10 Cycle to cycle variation of frost thickness for the hydrophobic surface at LCR at conditions of run 2 (table 2.1)

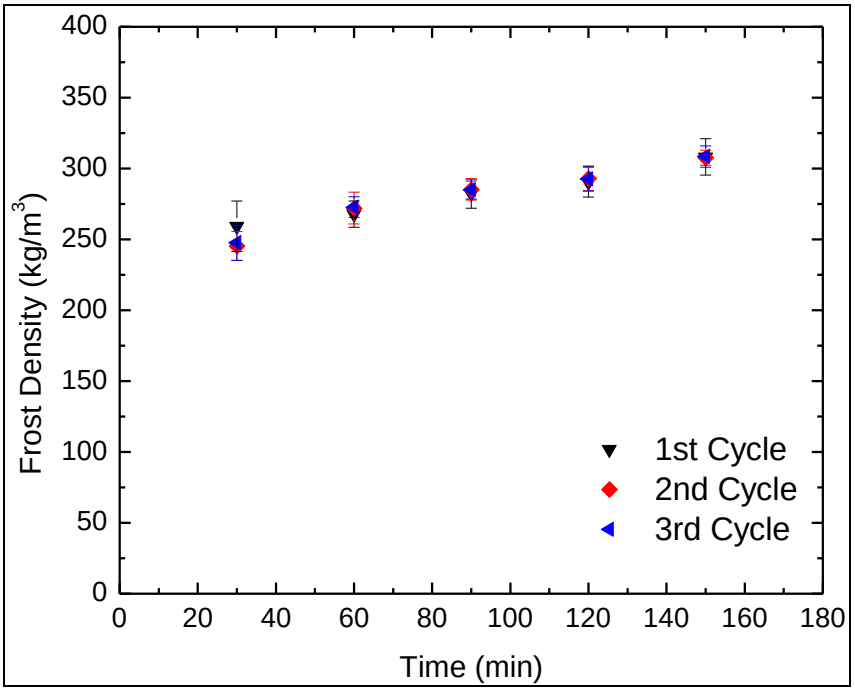

Figure 2.11 Cycle to cycle variation of frost density for the hydrophobic surface at LCR at conditions of run 2 (Table 2.2)

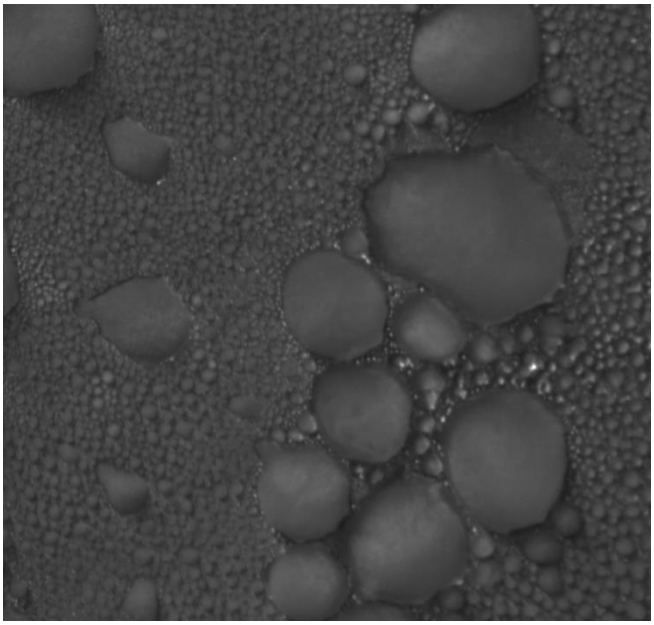

Figure 2.12 Frozen droplets on a hydrophobic surface at the beginning of the second frosting cycle (HCR)

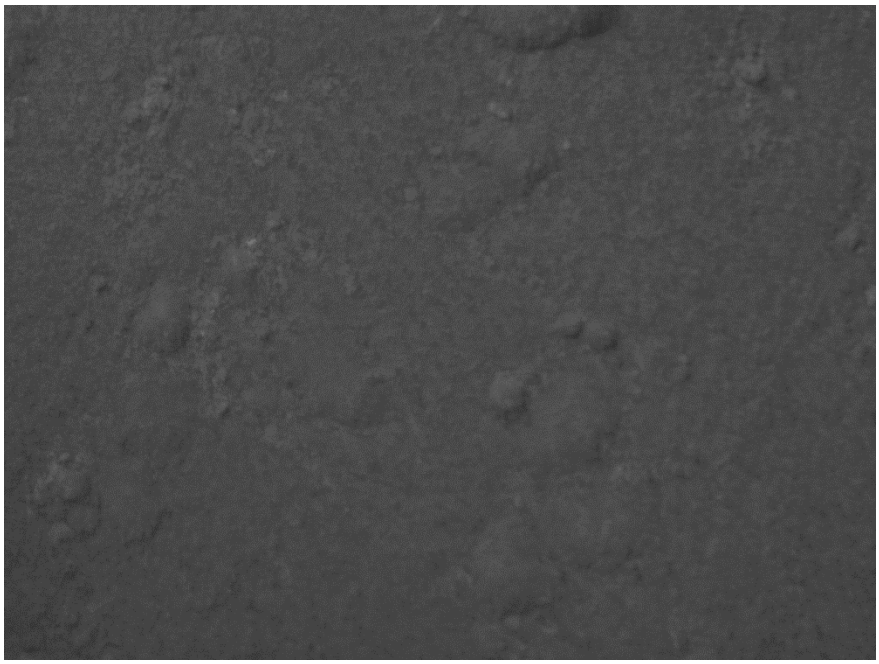

Figure 2.13 Frozen water film on a complete-wetting surface at the beginning of the second frosting cycle (HCR)

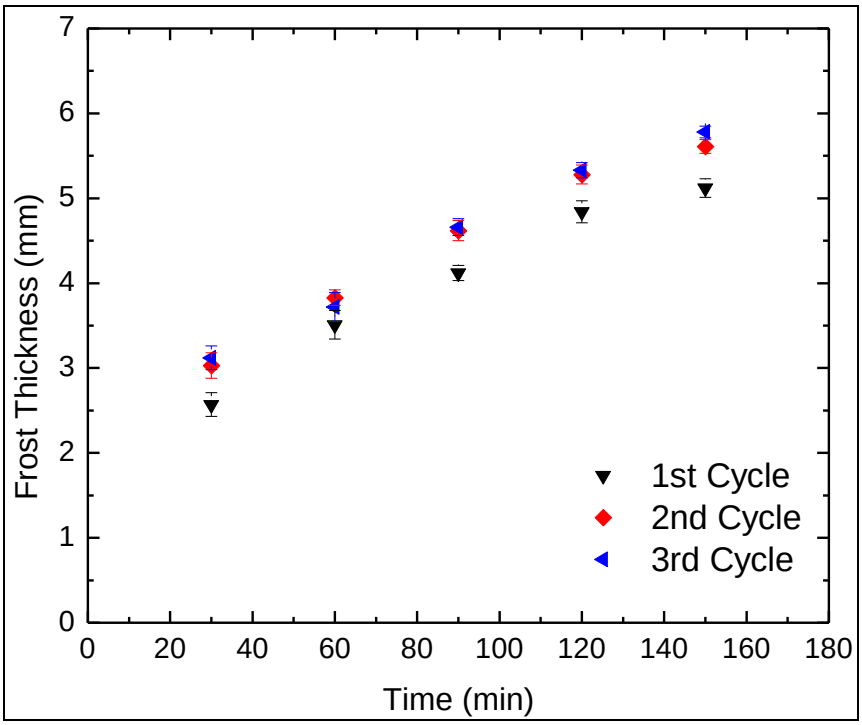

Figure 2.14 Cycle to cycle variation of frost thickness for the hydrophobic surface at HCR at conditions of run 1 (Table 2.2)

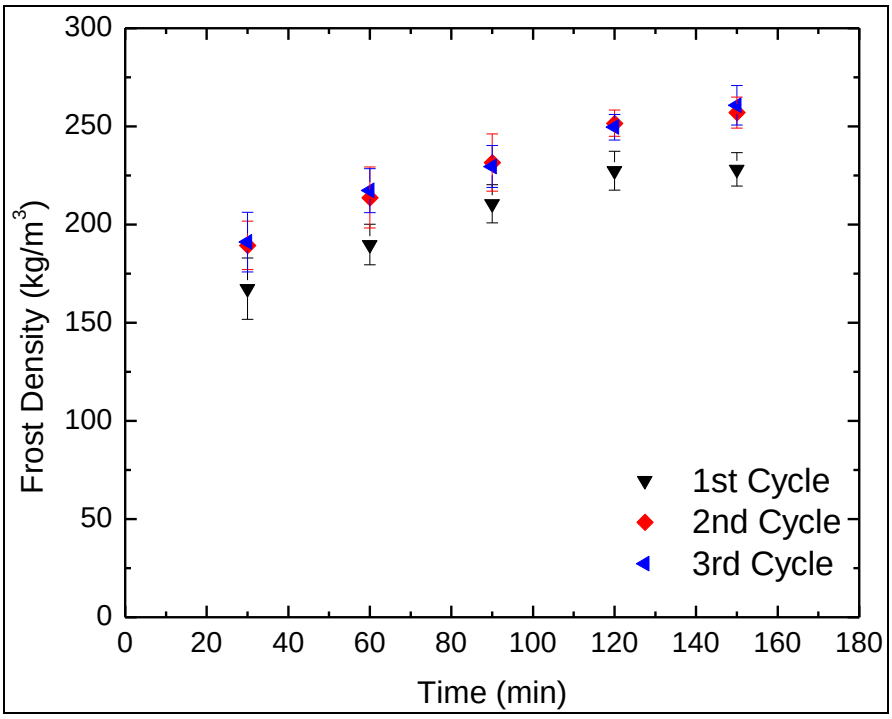

Figure 2.15 Cycle to cycle variation of frost density for the hydrophobic surface at HCR at conditions of run 1 (Table 2.2)

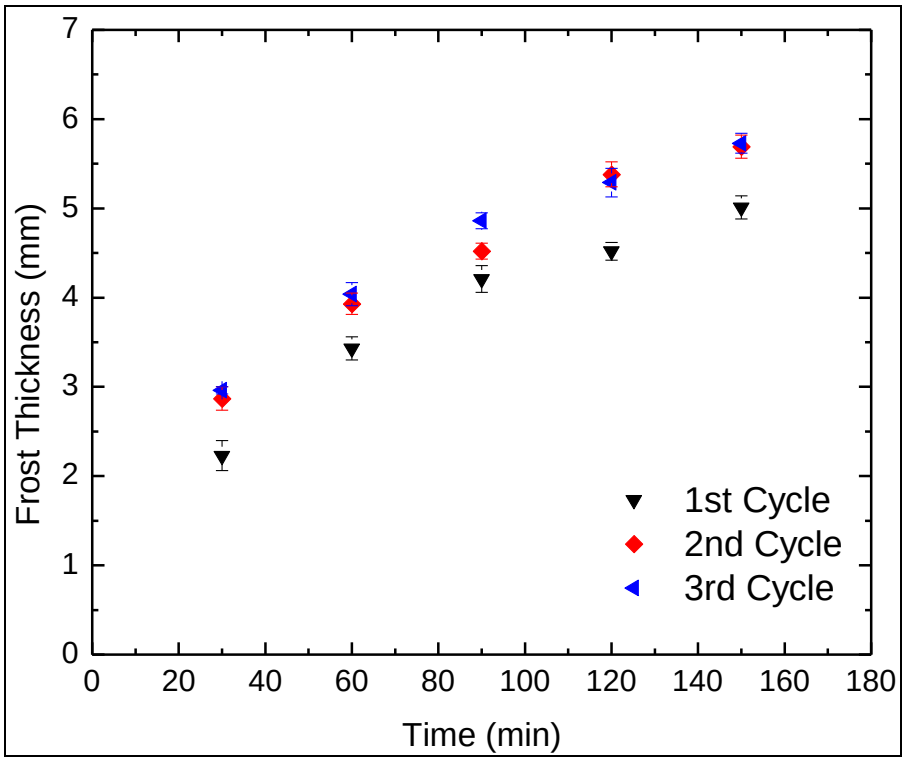

Figure 2.16 Cycle to cycle variation of frost thickness for the uncoated aluminum surface at HCR at conditions of run 1 (Table 2.2)

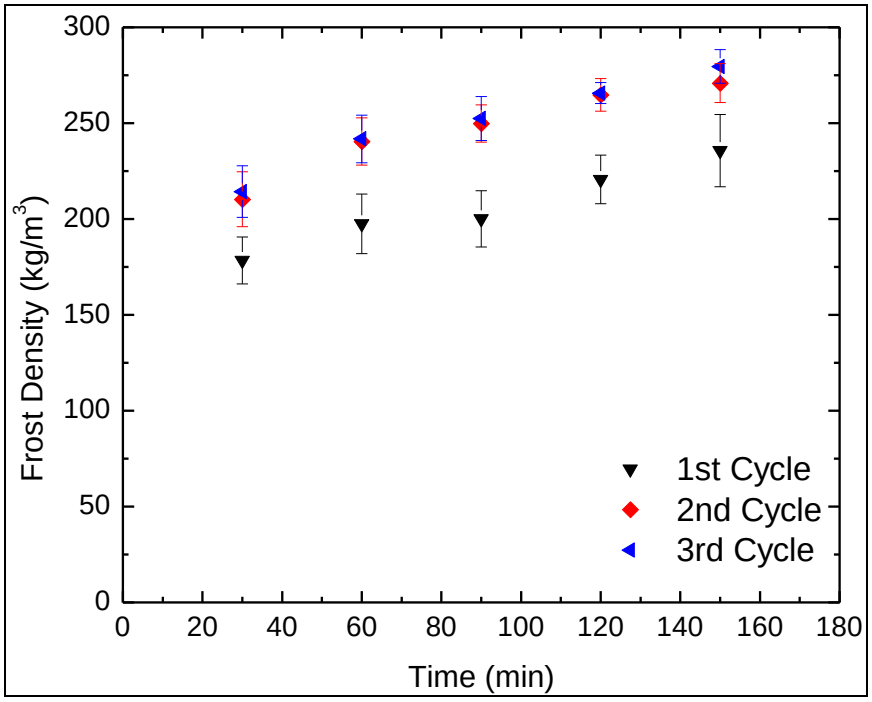

Figure 2.17 Cycle to cycle variation of frost density for the uncoated aluminum surface at HCR at conditions of run 1 (Table 2.2)

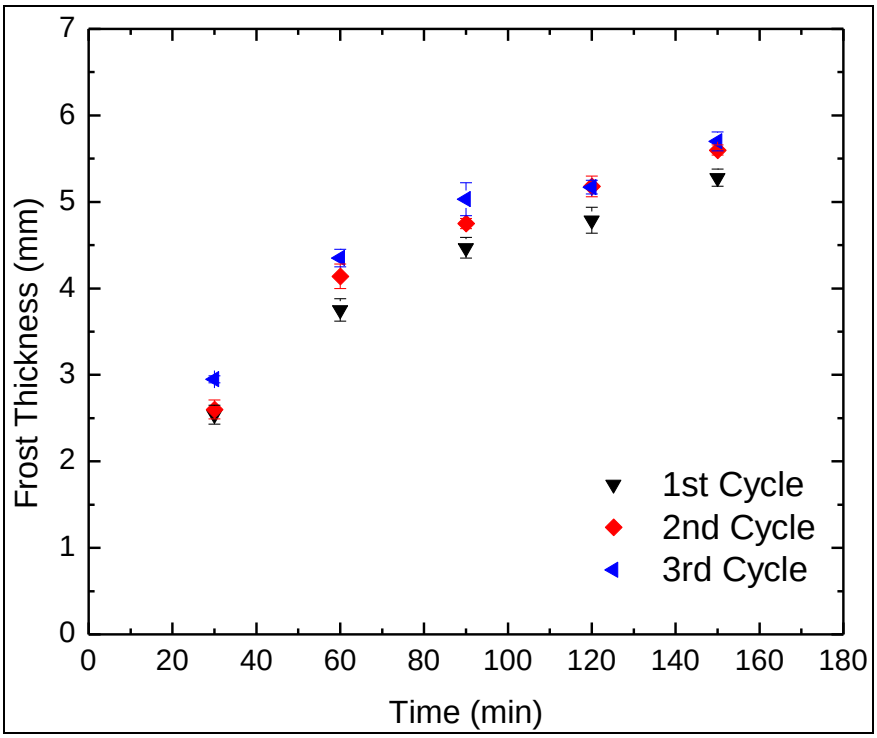

Figure 2.18 Cycle to cycle variation of frost thickness for the complete-wetting surface at HCR at conditions of run 1 (Table 2.2)

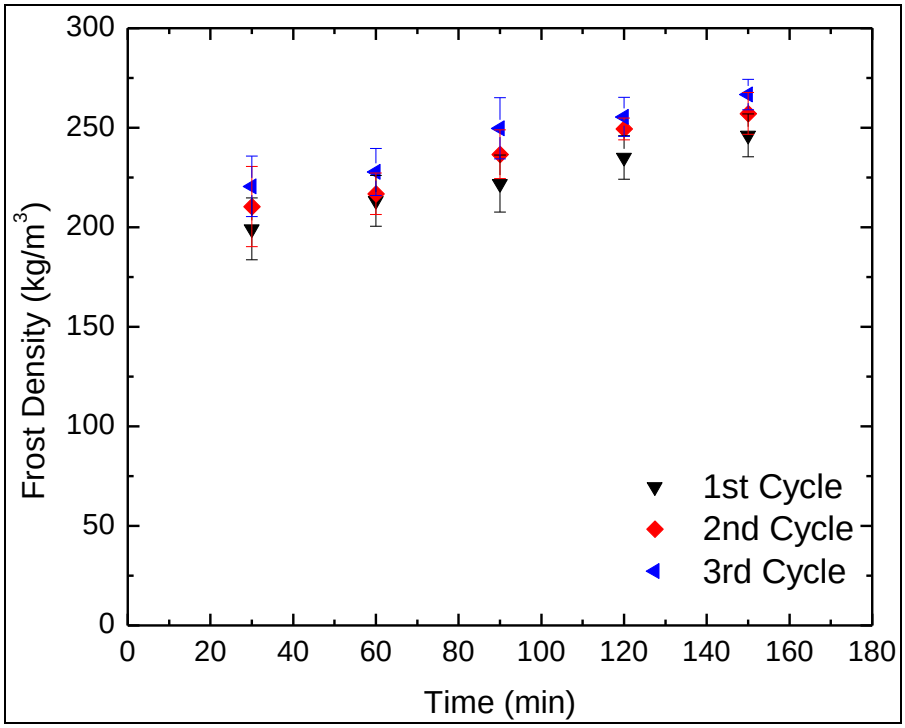

Figure 2.19 Cycle to cycle variation of frost density for the complete-wetting surface at HCR at conditions of run 1 (Table 2.2)

Table 2.1 Equilibrium, advancing, and receding contact angles of the 5 samples

Sample	**1**	**2**	**3**	**4**
Surface	**Complete-Wetting**	**Hydrophilic**	**Uncoated**	**Hydrophobic**
Equilibrium $\boldsymbol{\theta_s}$	0	49.9	60.4	103.9
Advancing $\boldsymbol{\theta_A}$	0	65.3	85.2	110.2
Receding $\boldsymbol{\theta_R}$	0	21.7	42.1	65.8
$\boldsymbol{\theta_A}$- $\boldsymbol{\theta_R}$	0	43.6	43.1	50.4

Table 2.2 Experimental conditions used to investigate the effect of different parameters on the frost growth rate

Run	**1**	**2**
Air Temperature (ºC)	**17**	**10**
Relative Humidity (%)	**60**	**70**
Plate Temperature (ºC)	**-15**	**-12**
Air Velocity (m/s)	**1.1**	**1.1**

CHAPTER 3

CONDENSATE DISTRIBUTION ON SURFACES WITH DIFFERENT WETTABILITIES

In a condensation-frosting scenario, frosting is initiated by the nucleation of the ice phase from the liquid phase in the condensed droplets. During the early frost growth period, ice crystals in the shape of rods start growing in the vertical direction on top of the frozen droplets. This period is followed by a mature frost growth period during which small branches start growing from the rods and the frost layer becomes uniform.

3.1 Data Reduction and Interpretation

After the steady-state condensate distribution is realized on the surface, plate temperature is further decreased below the water freezing point. First, bigger droplets freeze, and later smaller ones follow. Bigger droplets are at lower pressures than smaller ones; therefore, as shown in the phase diagram of water (Figure 1.1), their freezing temperature is higher. However, from experimental observations, it takes less than 2 minutes for the entire population of droplets ranging in size from the minimum (taken to be 10μm) to the maximum diameter to freeze even when the cooling rate is low. Therefore, the droplets freezing process is assumed to be instantaneous and the early frost growth period is assumed to start when rod-shaped crystals grow from the frozen droplets. As discussed in chapter 2, images of the frozen droplets on the surface are recorded immediately after all the water droplets on the surface are frozen. An image of frozen droplets on an uncoated aluminum surface is shown in Figure 3.1, and the processed

image used to perform a droplet count on the surface is shown in Figure 3.2. Details on the image processing methodology are provided in Appendix A.

During drop counting, 10 drop sizes ranging from the smallest diameter to the departure size were selected. All droplets with diameters within 20% of the selected diameter were considered to be of that size. The droplet count performed on 10 images was averaged to find the experimental droplet distribution function for the surface. Due to limitations in the camera used to take the droplet pictures, the smallest droplet that could be accurately traced and counted had a diameter of 400 microns.

3.2 Results and Discussion

3.2.1 Graham's Distribution Function

Graham (1969) suggested a droplet distribution function based on a detailed photographic study of condensation on flat copper surfaces. The proposed distribution is a logarithmic function that changes slope when drop sizes become large. According to Graham, there are four possible stages of droplet development during condensation: the nucleation stage, the condensation-coalescence stage, the coalescence stage, and the departure stage. As indicated by El-Sherbini and Jacobi (2003), the growth of small drops (with diameters less than 10μm) is dominated by condensation, while the growth of larger drops is more influenced by coalescence. The transition in droplet distribution from small to large droplets occurred at a diameter of $0.2D_{max}$ (Graham, 1969). Therefore, the size distribution can be expressed as:

$$n_s(d) = Q_s d^{b_s} \quad \text{for } d_{min} \leq d \leq 0.2d_{max} \tag{3.1}$$

$$n_b(d) = Q_b d^{b_b} \quad \text{for } 0.2d_{max} < d \leq d_{max} \tag{3.2}$$

As shown by El-sherbini and Jacobi (2003), previous investigators have reported different values of the coefficients (b_s, b_b, Q_s, Q_b,). However, Graham (1969) and one of the distributions of Tanasawa and Ochiai (1973) agreed on a value of bs, of the distribution function for small droplets of -2.73. Therefore, the three other constants (b_b, Q_s, Q_b,) remain undetermined. El-Sherbini and Jacobi used the area ratios covered by small and big droplets to determine the remaining coefficients as follows:

$$A_{cov,s} = \int_{D_{min}}^{0.2D_{max}} n_s \, (\pi/4) D_s^2 dD_s \tag{3.3}$$

$$A_{cov,b} = \int_{0.2D_{max}}^{D_{max}} n_b \, (\pi/4) D_b^2 dD_b \tag{3.4}$$

Equations 3.3 and 3.4 were combined with the continuity of the size distribution at D=0. $2D_{max}$ (Equation 3.5) to find the values of (b_b, Q_s, Q_b,).

$$Q_b(0.2D_{\max})^{b_b} = Q_s(0.2D_{\max})^{b_s} \tag{3.5}$$

The area ratios covered by small and big droplets were calculated from the droplet count discussed in Section 3.1.

3.2.2 Effect of Area Ratios Covered by Small/big Droplets

Since only droplets with diameters higher than 400μm were counted, it was necessary to check the impact the decrease in the small area covered ratio resulting from neglecting very small droplets. Therefore, a parametric study was done in order to investigate the effect of the covered area ratios on the initial conditions predicted by the proposed method. As shown in Figures 3.3 and 3.4. The covered area ratios have a significant effect on the density distribution inside the layer of frozen droplets. The higher the values of the area ratios covered by small and

big droplets, the higher the initial frost density. The effect of the area covered by small droplets is only important near the wall, but the area covered by big droplets is significant in the entire layer of frozen droplets. The contribution of the small droplets (with diameters less than 400μm) to the total mass of water condensate on the surface and to the area covered ratio is small (less than 2%). Therefore, it will result in a marginal decrease in the initial density near the wall and does not affect the accuracy of the model. Moreover, Hoke *et al.* (2004) observed that very small droplets evaporate at the moment of freezing and merge with the neighboring bigger droplets. Hence, it is justified not to take into account their impact on the area covered ratio after freezing occurs.

3.2.3 Experimental Droplet Count

As discussed earlier, four samples ranging from complete-wetting to hydrophobic with ACA of 110º were tested. Condensed droplets on hydrophobic surfaces had spherical cap shape (Figures 3.5 and 3.6). However, on more hydrophilic and uncoated aluminum surfaces, the droplets had highly irregular shapes after they coalesced with neighboring droplets (Figures 3.1 and 3.7). For droplets with irregular shapes, an equivalent diameter of a circle having the same base area of the droplet was calculated. On the other hand, surfaces with very low contact angles are completely wetted by the condensed droplets and form a thin film of frozen water at the beginning of the frosting cycle (Figure 3.8).

Graham's size distribution function was developed based on experimental data for droplets of spherical shapes. Therefore, as expected the agreement between the droplet count and the distribution function for hydrophobic sample 4 is very good as shown in Figure 3.8. In addition, the logarithmic function proposed by Graham works fairly well for uncoated

Aluminum surface (sample 3). However, for the hydrophilic sample (sample 2), as shown in Figure 3.10, an adjustment was required to the coefficients calculated using the method described in section 2.3.1. The adjusted power law curve fits were as follows:

$$n_s(d) = 11227d^{-1.914} \quad \text{for } 10\mu m \leq d \leq 0.9\, mm \tag{3.6}$$

$$n_b(d) = 108.96d^{-1.225} \quad \text{for } 0.9mm < d \leq 3mm \tag{3.7}$$

Moreover, the point separating the coalescence and departure stages is not very clear from the droplet count results performed in this study. Graham's observations showed that the separation point falls in the range of 500 to 1000 microns, and his final drop size distribution at atmospheric pressure had a change in slope at 20% of the maximum diameter. Nevertheless, there was no separation point in his data during low-pressure condensation. In order to check the impact of the separation point on the present model predictions, the hydrophobic surface droplet count data were fitted with one single linear fit and the initial frost density variation was calculated using the method presented in Section 4.2.3. Then, the impact of the initial conditions on the frost density predictions of the mathematical model for frost growth (presented in Chapter 4) was examined. As shown in Figure 3.12, the change in the calculated initial frost density (less than 8%) resulted in an insignificant impact on the predicted frost density. Therefore, it was found more convenient to use Graham's distribution function since it is more general.

3.3 Conclusions

In this chapter, a droplet counting procedure for frozen droplets on surfaces with various wettabilities was performed. Results were compared to the logarithmic function suggested by Graham (1975) and widely used for predicting the steady-state condensate distribution on a surface.

The mathematical function was in good agreement with experimental data for hydrophobic and uncoated aluminum surfaces (samples 3 and 4). However, an adjustment was required for the hydrophilic surface (sample 2), mainly due to the highly irregular shapes of the droplets after coalescence. The validated distributions will be used (in chapter 4) to find initial conditions for frost thickness and density required in modeling frost growth on vertically oriented flat surfaces.

3.4 Figures and Tables

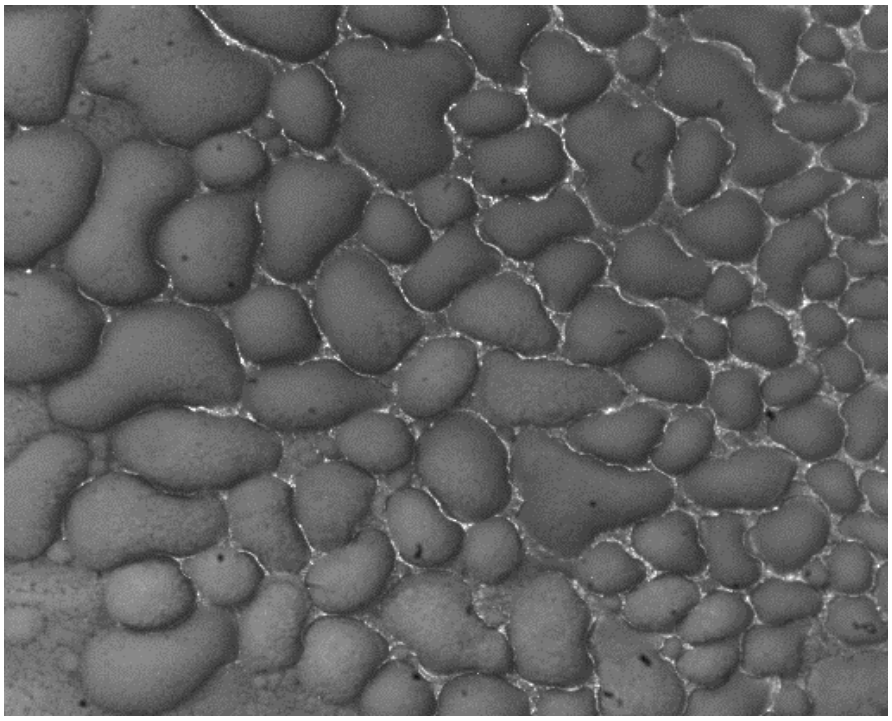

Figure 3.1 Original image of frozen droplets on a uncoated aluminum surface

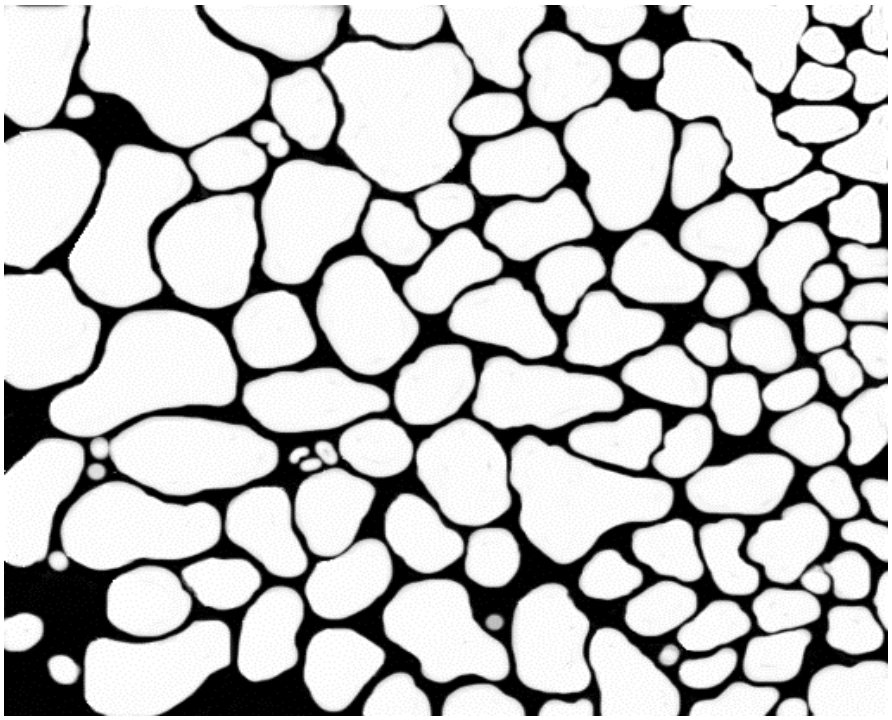

Figure 3.2 Processed image of frozen droplets on an uncoated aluminum surface

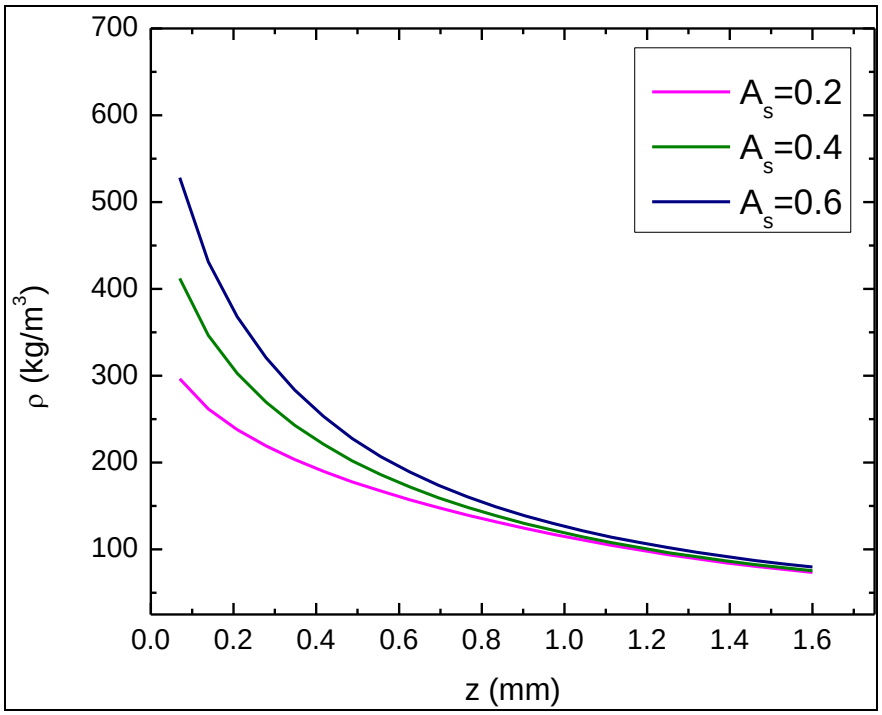

Figure 3.3 Effect of area covered by small droplets on initial frost density

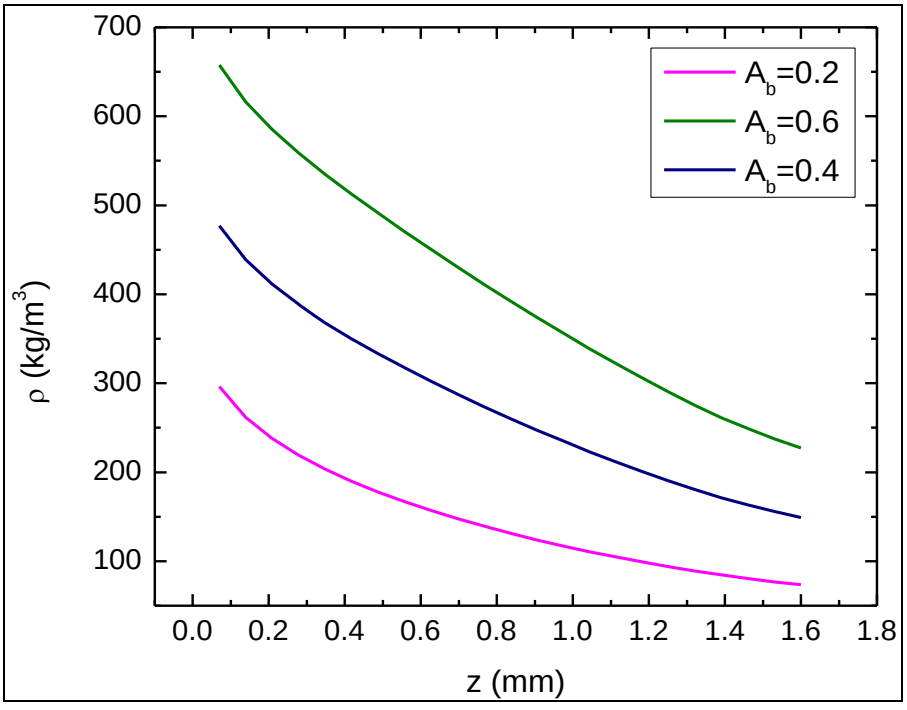

Figure 3.4 Effect of area covered by big droplets on initial frost density

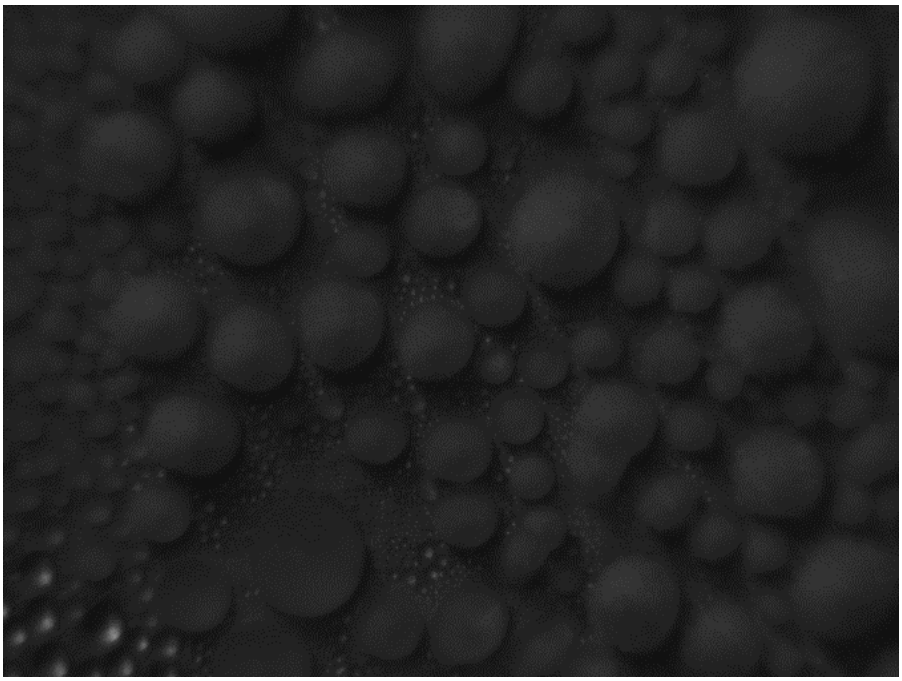

Figure 3.5 Original image of frozen droplets on a hydrophobic surface (sample 4)

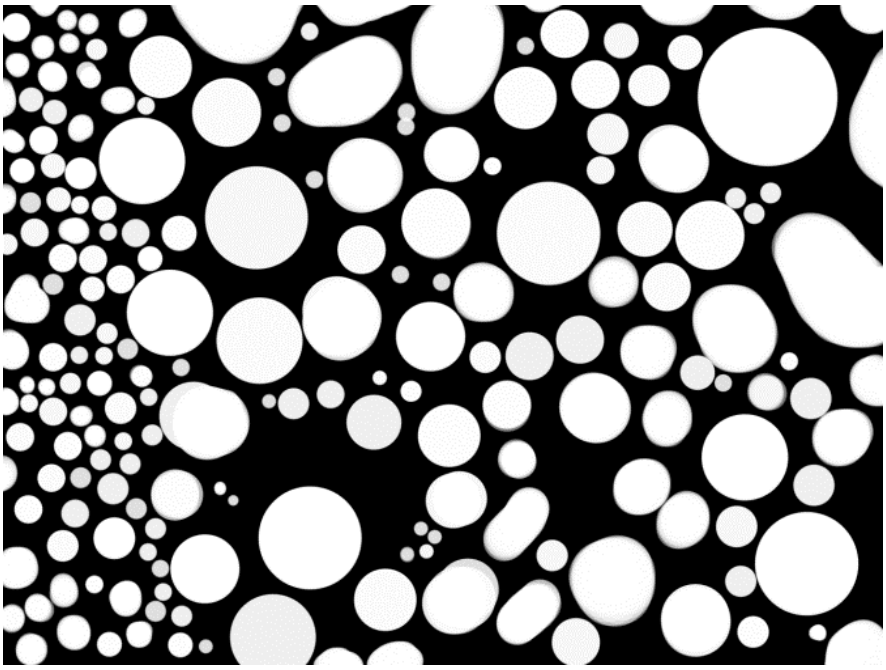

Figure 3.6 Processed image of frozen droplets on a hydrophobic surface (sample 4)

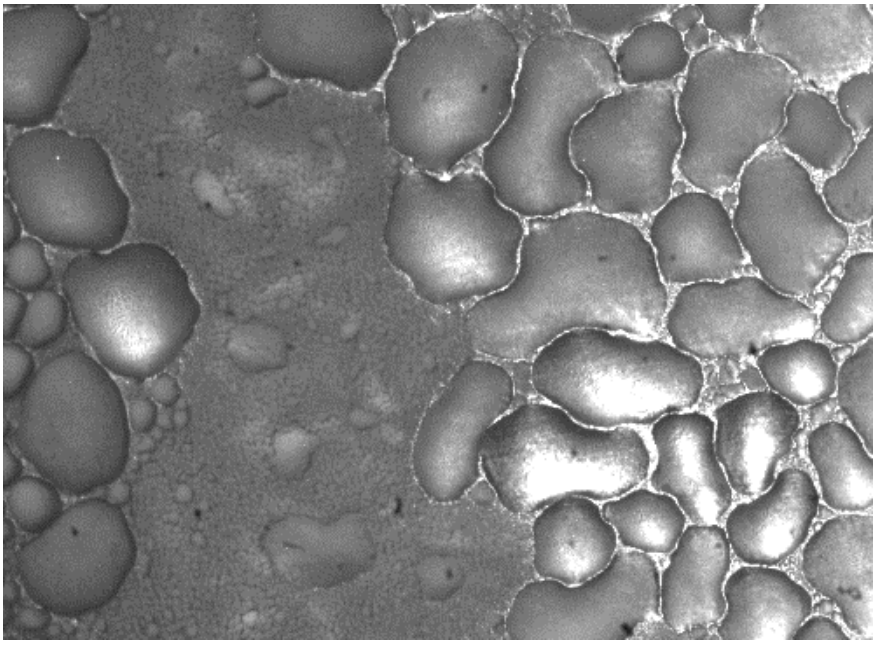

Figure 3.7 Original image of frozen droplets on a hydrophilic surface (sample2)

Figure 3.8 Original image of frozen water film on a complete-wetting surface (sample1)

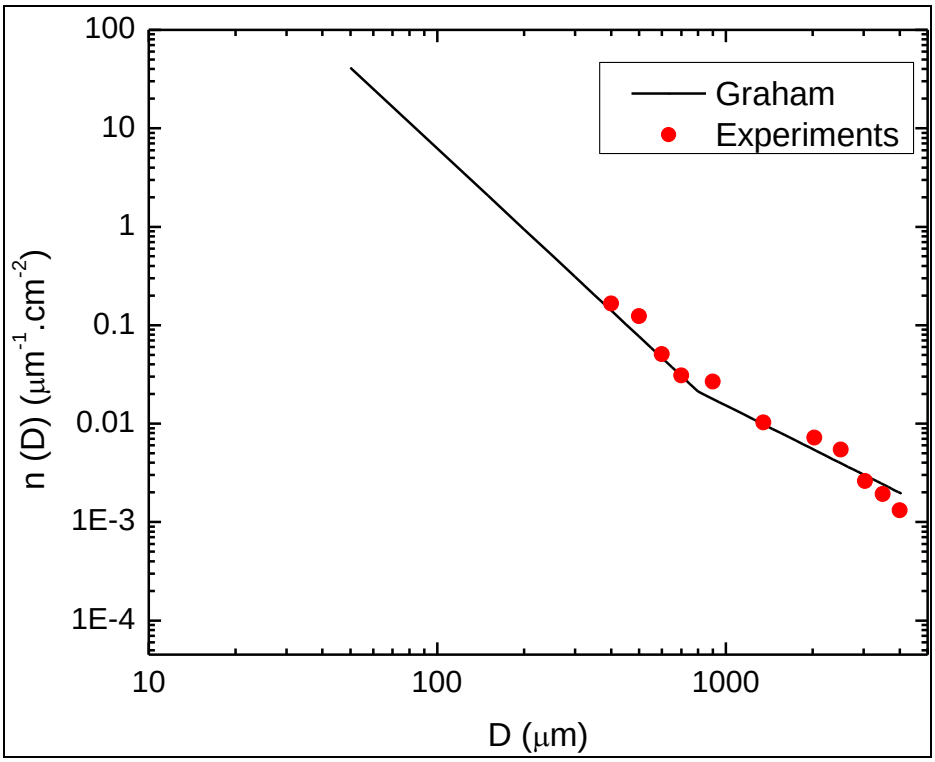

Figure 3.9 Droplet distribution on an uncoated aluminum surface (sample 3)

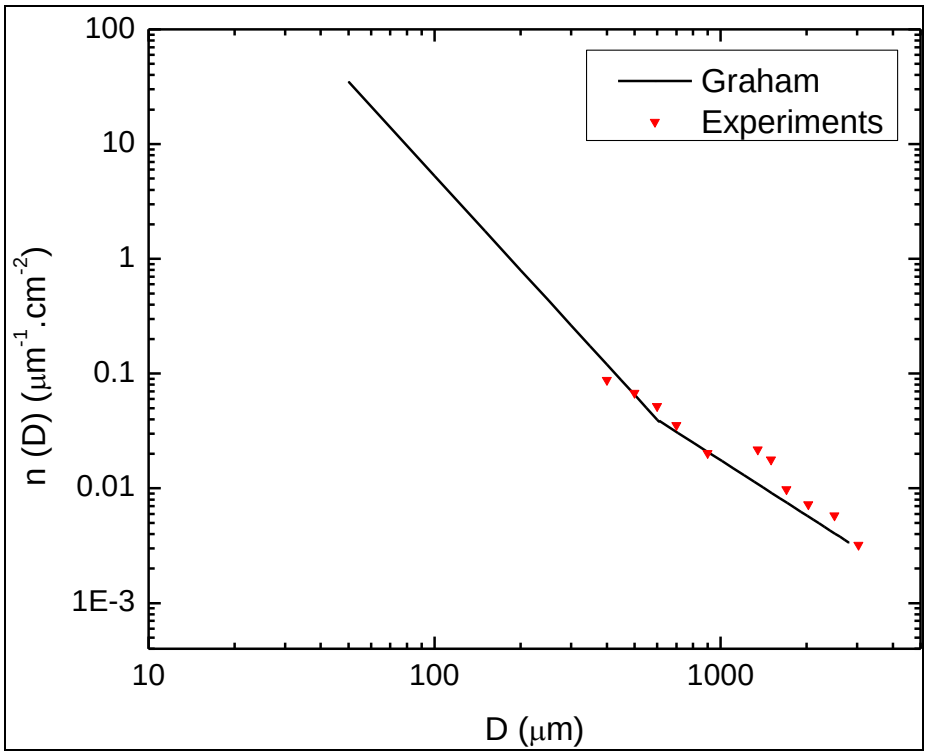

Figure 3.10 Droplet distribution on a hydrophobic surface (sample 4)

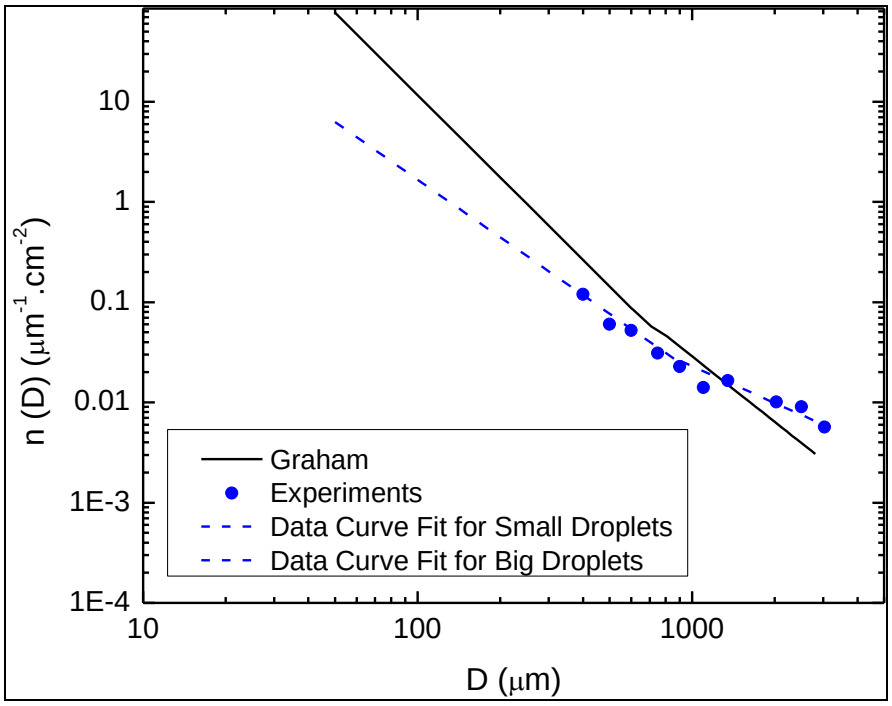

Figure 3.11 Droplet distribution on a hydrophilic surface (sample 2)

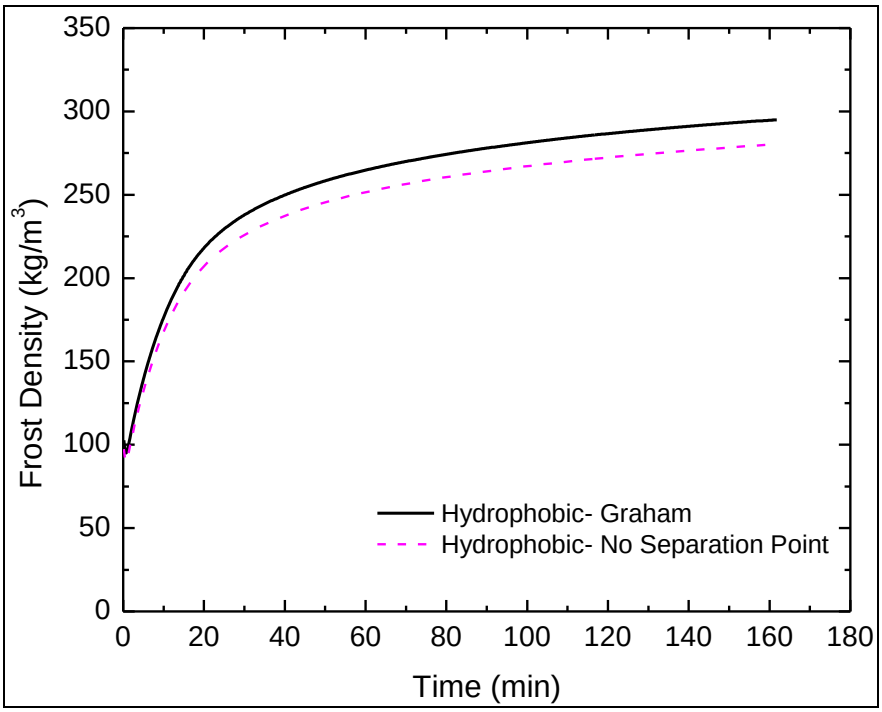

Figure 3.12 Comparison of frost density calculated using Graham's distribution and a linear curve fit of the droplet count data performed in this work

CHAPTER 4

MATHEMATICAL MODEL FOR FROST GROWTH ON VERTICALLY ORIENTED FLAT PLATES

Based on the assumption of dropwise condensation, a new model for frost growth and densification on a flat, vertically oriented surface was developed. The model assumes that the frost layer is initiated from a population of frozen droplets that accumulated on the surface during the condensation phase. Therefore, the surface wettability effects are taken into account in the model through the initial conditions for frost density and thickness.

4.1 Frost Growth Modeling

The physical situation for the growth and densification of a frost layer on a cold surface is shown schematically in Figure 4.1. As moist air passes above a cold surface with temperature below the freezing point of water, frost crystals start forming on the surface. The "crystal growth period" is followed by "frost layer growth period" during which a frost layer grows by ablimation (Hayashi, 1977). The frost growth involves simultaneous heat and mass transfer driven by the temperature and water mole fraction differences between the frost layer and the surrounding air. The total heat flux can be divided into sensible and latent components. The latent heat flux is directly related to the mass flux of water vapor that deposits on the frost surface, therefore contributing to its growth. On the other hand, the gradient in the partial density of water vapor at the frost surface causes diffusion of water vapor into the frost layer, therefore increasing its density.

4.2 Mathematical Formulation

4.2.1 Heat and Mass Conservation Equations

Assuming that the frost density and effective thermal conductivity vary within the frost layer (in the z-direction), a control volume analysis is performed in order to relate the frost growth to the air properties and cold plate temperature.

The total heat flux transferred from air to the frost layer can be divided into a sensible and a latent heat flux as follows:

$$q_a'' = q_{lat,t}'' + q_{sens}'' \tag{4.1}$$

$$q_{sens}'' = h\left(T_a - T_{fst,s}\right) \tag{4.2}$$

$$q_{lat,t}'' = m_{t,s}'' h_{sg} \tag{4.3}$$

The total water mass flux at the frost surface is divided into 2 components; m_δ'' which contributes to thickening the frost layer, and $m_{\rho,s}''$ which diffuses into the frost layer and contributes to its densification.

$$m_{t,s}'' = m_\delta'' + m_{\rho,s}'' = h_m \rho_a \left(\omega_a - \omega_{fst,s}\right) \tag{4.4}$$

$$m_\delta'' = \rho_{fst}\left(d\delta_{fst}/dt\right) \tag{4.5}$$

$$m_{\rho,s}'' = D_{eff}(d\rho_v/dz)\big|_{z=\delta} \tag{4.6}$$

Similarly, in order to calculate the frost density in different locations within the frost layer, the local diffusive mass flux is needed at different locations:

$$m_{\rho,z}'' = D_{eff}(d\rho_v/dz)\big|_z \tag{4.7}$$

In order to examine the contribution of the bulk vapor motion to the water-vapor diffusion inside the frost layer, the blowing factor, *BF*, was calculated. The blowing factor is related to the ratio of the actual to the zero-velocity solution to diffusion through a stationary medium (Mills, 2001). For air flowing with a velocity of 1 m/s above a frost layer, the blowing factor was found to be approximately 1.004. Therefore, all the mass diffused inside the frost layer was attributed to Fickian diffusion and the presence of diffusional velocities was neglected.

Then a mass balance on a differential control volume within the frost layer of thickness *dz* (shown in Figure 4.2) relates the local frost density change rate to the gradient of the diffusive mass flux as follows:

$$\partial m''_{\rho,z}/\partial z = \partial \rho_{fst}(z)/\partial t \tag{4.8}$$

The frost growth was assumed quasi-steady and transient effects were neglected in both the heat and mass conservation equations. A linear driving force model for mass diffusion of water vapor was used to model the vapor density variation in the frost layer as follows:

$$D_{eff}(\partial^2 \rho_v/\partial z^2) + U\,\partial \rho_v/\partial z = \varepsilon_{fst}\left(\rho_v - \rho_{v,sat}\right) \tag{4.9}$$

Where *U* is the Darcy velocity given by

$$U = 1/\rho_v \int \varepsilon_{fst}\left(\rho_v - \rho_{v,sat}\right)dz \tag{4.10}$$

and the effective diffusion coefficient D_{eff} was computed by multiplying the diffusion coefficient of water in air by the porosity, Φ, and the tortuosity, τ. The tortuosity factor was obtained from a model by Zehnder (Na and Webb, 2004):

$$D_{eff}(z) = D\Phi(\mathrm{z})\tau(z) \tag{4.11a}$$

$$\tau\,(z) = 1 - \sqrt{1 - \Phi(\mathrm{z})}/\Phi(\mathrm{z}) \tag{4.11b}$$

Inspection of equation (4.9) makes it clear that ε_{fst} is a mass transfer coefficient multiplied by a ratio of area to volume. The mass transfer conductance, ε_{fst}, depends mainly on the frost structure, and therefore detailed investigation is required to determine the appropriate value of this parameter.

The Darcian term in the mass balance equation (Equation 4.9) was found to be 2 orders of magnitude lower than the other terms. Therefore, this term can be neglected without affecting the accuracy of the model.

The porosity of the frost layer can be related to the frost density as follows:

$$\rho_{fst}(z) = \Phi(\mathrm{z})\rho_a + (1 - \Phi(\mathrm{z}))\rho_i \tag{4.12}$$

A balance between the heat transfer by conduction in the frost layer and the latent heat transfer due to the phase change can be expressed as:

$$k_{fst}\left(d^2T_{fst}/dz^2\right) = -\varepsilon_{fst}h_{sg}\left(\rho_v - \rho_{v,sat}\right) \tag{4.13}$$

An empirical correlation by O'Neal and Tree (1985) was used to relate the frost thermal conductivity was to its density:

$$k_{fst} = 0.001202\rho_{fst}^{0.963} \tag{4.14}$$

Where k_{fst} is in W/m·K and ρ_{fst} is in kg/m^3.

The average heat transfer coefficient, *h*, for laminar flow over a smooth, flat was determined from the following (Incropera, 2002):

$$Nu = 0.664Re^{1/2}Pr^{1/3} \tag{4.15}$$

The boundary layer suction effect was neglected in the model since the Darcy velocity was determined to be negligible.

The analogy between heat and mass transfer was invoked as $Sh=Nu(Sc/Pr)^{1/3}$ to find the mass transfer coefficient h_m .

4.2.2 Boundary Conditions

Equations (9) and (13) require boundary conditions of water vapor density and frost temperature at the cold plate and the frost surface. A fixed temperature was prescribed at the cold plate and the frost surface temperature was related to the total heat flux from the surrounding air to the frost layer from an energy balance at the frost surface as shown in Figure 4.3:

$$\text{At z = 0, } T = T_w \tag{4.16a}$$

$$\text{At z = } \delta, \; k_{fst}(dT/dz)|_{z=\delta} = q_a'' - q_{lat,\rho}'' = q_a'' - m_\rho'' h_{sg} \tag{4.16b}$$

For the water vapor density, the boundary conditions can be written as:

1- The no-flux boundary conditions at the cold plate: $d\rho_v/dz|_{z=0} = 0$ (4.17)

2- The total heat flux transferred from the frost layer to the surrounding air was used to find the gradient of the water-vapor density at the surface as follows:

$$q_a'' = m_{t,s}'' h_{sg} + h\left(T_a - T_{fst,s}\right) \tag{4.18a}$$

$$D_{eff}(\partial\rho_v/\partial z)|_{z=\delta} = m_{t,s}'' - \rho_{fst}\left(d\delta_{fst}/dt\right) \tag{4.18b}$$

4.2.3 Initial Conditions

All processes were assumed to be quasi-steady. Equations (4.5) and (4.8) were discretized using a finite-difference forward scheme. Therefore, two initial conditions for frost density and thickness were required. Assuming that the condensed droplets freeze instantly and that the frosting process starts (time=0) right after all the droplets turn into ice. Then, the initial

density and thickness are directly related to the frozen droplet distribution on the surface. Therefore, initial conditions strongly depend on the cooling rate unless condensation is allowed until the "steady-state" distribution of droplets occurs. In this case, decreasing the cooling rate any further will not affect the frosting process, since the number of droplets of each size remains same as the condensation process continues.

The present model is based on the assumption that the steady-state droplet distribution is achieved before the plate temperature decreases to below the water freezing point. The droplet distribution suggested by Graham (1973) and validated in chapter 3 was used to find the initial frost density variation inside the layer of frozen droplets. The droplet shape on vertical surfaces was determined based on the work of El-Sherbini and Jacobi (2003). The maximum droplet diameter was calculated from a balance between the gravity and surface tension forces and therefore mainly depends on the surface wettability and orientation. Figure 4.4 shows a comparison between the maximum droplet size calculated using El-Sherbini's method (2003) and the size of the largest condensed droplet on the tested samples. The discrepancy between experimental data and the model can be attributed to the irregular water droplet shape after it coalesces with neighboring droplets, therefore affecting the surface tension force since it depends on the contact line shape.

The frost density variation from the cold surface (z = 0) to the maximum droplet height (z= z_{max}) was calculated by dividing the mass of frozen water by the total volume occupied by the droplets.

$$\rho_{fst}(z) = \rho_{ice}/z \int_0^z \left(A_c(y)/\ A_{Proj}\right) dy \qquad (4.19)$$

4.2.4 Numerical scheme

The governing equations (4.5), (4.8), (4.9) and (4.13) were discretized and solved simultaneously with the algebraic equations using a commercial software package, Engineering Equation Solver (EES[1]). A sensitivity analysis was used to determine the effect of the time interval and number of grid points on the final results. Based on the analysis, a time step of 10 seconds and 20 grid points were adopted. Based on the analysis, a time step of 10 seconds and 20 grid points were adopted since a further increase in the grid size or decrease in the time step does not change the frost density and thickness predictions by more than 1%. At each time step, iterations were performed until the relative changes in the density, thickness and temperature were less than 10^{-6}.

4.3 Results and Discussion

The effect of the boundary conditions for frost temperature and water vapor-density are discussed in the following subsections. Subsection 4.3.1 discusses the model predictions of frost thickness, density and water vapor density assuming saturation conditions prevail at both the cold plate and frost-air interface. The impact of the mass transfer conductance, ε_{fst}, on the frost layer properties is discussed in details in subsection 4.3.2. Then, a simplified model of the frost layer as a porous medium of ice rods separated by air gaps is proposed to determine the parameter ε_{fst}. Finally, the model predictions are validated by comparing them to experimental data of frost thickness and density on samples with various wettabilities.

[1] Publisher: F-Chart Software, 1992

4.3.1 Saturation Boundary Conditions

Most theoretical models for frost growth on flat surfaces assume that the water-vapor is saturated at both the cold surface and the frost-air interface (z=0 and z=δ, respectively):

$$\rho_v|_{z=0} = \rho_{v,sat}(T = T_w) \tag{4.20a}$$

$$\rho_v|_{z=\delta} = \rho_{v,sat}(T = T_{fst,s}) \tag{4.20b}$$

However, these assumptions do not have any physical basis and were not validated experimentally. Therefore, it was found convenient to check the validity of the saturation boundary conditions in the present frost growth model. For this purpose, equations (4.18a) and (4.18b) were replaced by equations (4.20a) and (4.20b). The saturation model results for frost density and thickness were within the expected range determined from earlier experimental data (See Chapter 2). However, as shown in Figure 4.6, the water-vapor density at any location within the frost layer was lower than the saturated water-vapor density at the corresponding local temperature. For such a situation, mass transfer should occur from the frost layer to the surrounding air. However, the frost layer is growing. Thus, the boundary condition that water vapor is saturated at the cold plate and the frost-air interface is physically impossible.

4.3.2 Parametric Study on the Mass Transfer Conductance

The main parameter that is required in the linear driving force model is the constant of proportionality ε_{fst}, which is a mass transfer conductance. As an initial step, a parametric study was used to determine the effect of ε_{fst} on the predicted frost properties mainly density and thickness. Later, a simplified model of the frost layer as a porous medium was used to relate ε_{fst} to the frost structure parameters.

4.3.2.1 Effect of ε_{fst} on Water Vapor Density

The property which is affected most by ε_{fst} is the water-vapor density. As shown in Figure 4.7, very low values of ε_{fst} produce unrealistic values of ρ_v. This parametric study shows that ε_{fst} has to be on the order of 100 s^{-1} for the model to give realistic frost and water-vapor properties.

For a fixed value of ε_{fst}=100 s^{-1}, the water-vapor density and the saturation density were plotted inside the frost layer. As shown in Figure 4.8, the water-vapor density is higher than the saturation vapor density at the corresponding temperature. Also, for any positive value of ε_{fst}, the water-vapor density is always greater than the saturation density. Therefore, the water-vapor at the frost surface and the cold plate is super-saturated and again it is clear that using the saturated boundary conditions leads to a significant error in the water-vapor density prediction.

Another important conclusion is that the water-vapor density distribution inside the frost layer is not linear. The linearity assumption was one of the key simplifications used in the boundary analysis conducted by Na and Webb (2004). This assumption was not justified in their proposed study and oversimplifies the frost growth phenomenon.

4.3.2.2 Effect of ε_{fst} on Frost Thickness and Density

Figures 4.9 and Figure 4.10 show the variation of the frost thickness and density with time as predicted by the present model for different values of ε_{fst}. For these results, the plate temperature was -20°C, air temperature 5°C, and air relative humidity was 60%. It can be concluded that the model is not highly sensitive to the value of ε_{fst} as long as this parameter varies within the range predicted in the earlier section. Moreover, results show that the lower the

mass transfer conductance ε_{fst}, the higher the frost thickness and the lower the density. The mass balance within a frost layer is mainly between advection and diffusion (Darcy velocity was found to be negligible). When the mass transfer coefficient decreases, the amount of water vapor diffusing into the frost layer decreases, therefore lowering its density. However, the mass transfer coefficient inside a time-changing structure like the frost layer is not constant with time. Therefore, a model is required to relate ε_{fst} to parameters describing the frost morphology including porosity and crystal shapes and sizes.

4.3.3 Modeling Mass Transfer Conductance

The morphology of snow crystals based on accurate imaging techniques was investigated by Libbrecht (1999). Mainly, two different crystal shapes were found: plate-like and column-like crystals. However, different variants of the shapes exist under each of the two big categories. Kobayashi *et al.* found that the snow crystals exhibited different shapes based on the surrounding air temperature and "excess vapor density" (Kobayashi, 1987). Nevertheless, the formation of snow crystals is different from frost growth since it does not occur on a substrate. In addition, the air temperature range of interest for studying the snow properties is restricted to below 0ºC, which is relatively lower than the temperatures in the applications of interest. Therefore, in the absence of studies on the frost crystal shapes, images inside frost layers at different environmental conditions were taken and analyzed.

Frost growth starts when condensed water droplets on the surface freeze as shown in Figure 4.11. Later, crystals of hexagonal shapes grow from the frozen droplets (Figure 4.12 and 4.13). Finally, branching form the hexagonal tubes occurs and a dendritic structure continues to develop in the last phase of the frosting process. Images in different planes of the frost layer

prove the existence of two main crystal shapes: hexagonal plate-type crystals and needle column-type crystals. Experiments to determine the frost crystal shapes and sizes were limited to the environmental conditions summarized Table 4.2. As shown in Figure 4.13, the hexagonal plate type crystals were more dominant for all the tested conditions. Therefore, assuming that the frost layer consists of rods with regular hexagonal cross-section of side length (a) and of height $\boldsymbol{\gamma}$, and the space between the rods is filled with air as shown in Fig. 11, a simplified frost structure model is developed as follows.

Therefore, assuming that the frost layer consists of rods with regular hexagonal cross-section of side length (a) and of height $\boldsymbol{\gamma}$, and the space between the rods is filled with air as shown in Figure 4.14, a simplified frost structure model is developed as follows.

The porosity (Ø) and surface area to volume ratio (β) can be related to the hexagon side length (a) and the spacing between rods (L) as follows:

$$\Phi = \left(L^2 - 3\sqrt{3}/2\, a^2\right)\gamma / L^2\gamma \tag{4.21}$$

$$\beta = A_s/V = 6a\gamma/L^2\gamma \tag{4.22}$$

Combining equations (4.21) and (4.22), the porosity can be expressed as a function of the surface area to volume ratio and the side length of the hexagon as follows:

$$\Phi = 1 - \sqrt{3}/4\,\beta a \tag{4.23}$$

Correlations for the heat transfer coefficient over an array of circular cylinders for different Reynolds number ranges were developed by Zhukauskas (1987).

$$Nu_d = CRe_d^{0.4}Pr^{0.37} \text{ for } 1 \leq Re_d \leq 40 \tag{4.24}$$

Phanikumar and Mahajan (2002) discussed the use of the same correlation for flow over bodies of different cross-section. Their investigation showed that the Reynolds number exponent variation with cross-sectional area is insignificant. Then, they used the same correlation with a different constant coefficient, *C*, to account for the non-circular fiber cross-section in metal foams. In the absence of a value for the coefficient, *C*, for hexagonal rods, the same value suggested by Zhukauskas (0.75) for circular tubes was used.

Therefore, knowing an average side length of the hexagon and the porosity, the area to volume ratio β can be calculated and used along with the heat and mass analogy to find the mass transfer conductance ε_{fst}.

The variation of ε_{fst} with porosity for different values of the crystal side length is shown in Figure 4.15. The model predictions fall within the range found from the parametric study. The values of ε_{fst} were always on the order of 100 or higher for all the crystal sizes measured from images similar to Figure 4.13. Therefore, the simplified model of frost as a porous medium succeeds in predicting values of ε_{fst} that fall within the range expected from the parametric study results presented in sections 4.3.2.1 and 4.3.2.2.

Nawaz *et al.* (2012) conducted an experimental study on the thermal-hydraulic performance of metal foam heat exchangers and found that equation 4.24 underpredicts the heat transfer coefficient in metal foams. Therefore, the new correlation proposed by Nawaz *et al.* (2012) was also used to predict the mass transfer conductance in the frost layer modeled as a porous medium. The increase in ε_{fst} did not have a significant impact on the frost growth model thickness and density predictions (less than 5%).

4.3.4 Frost Thickness and Density

The model was used to predict frost thickness and density at various environmental conditions summarized in Table 4.1. As shown in Figures 4.16 and 4.17, there is an excellent agreement between the model and experimental data for a hydrophobic surface with advancing contact angle of 110º. The frosting process can be divided into 2 stages: the early frost growth period and the mature frost growth period. As analyzed by Hayashi (1973), during the early frost growth period, the frost density can decrease depending on the properties of the surrounding air and the plate temperature. The current model predicts a decrease in the frost density during the first 5 minutes of the frosting cycle (Figure 4.18). This can be explained by a faster increase in the frost thickness due to the formation of rod-type crystals on top of the frozen droplets. Later, during the mature frost growth period, the density increases due to branching from the rod-type crystals.

4.3.4.1 Effect of Air Temperature and Humidity

A comparison of the frost thickness and density (from Figures 4.16 and 4.17) at conditions of run 2 and 3 reveals that the frost thickness increases when the air humidity increases. This increase in density is mainly due to an increase in the water vapor density gradient in the concentration boundary layer. Therefore, the amount of water entering the frost layer becomes larger. On the other hand, when the air temperature increases, the time required for water vapor molecules to freeze decreases. In this case, plate-type crystals of high density are formed without allowing small branching from the main crystal. This effect is successfully predicted by the model in conditions of runs 1 and 2.

4.3.4.2 Effect of Cold Plate Temperature

Another important parameter that affects the frost growth on a flat plate is the plate temperature. As shown in Figures 4.19 and 4.20, decreasing the plate temperature results in a decrease in frost density. When the plate temperature decreases, the diffusion coefficient inside the frost layer decreases. Subsequently, the fraction of water vapor depositing on the frost surface increases, therefore increasing the frost thickness and lowering its density.

4.3.5 Surface Wettability Effect

The main parameter that existing frosting models do not take into consideration is the surface wettability. Based on the proposed model, the surface wettability mainly affects the initial condition for frost thickness and density. Therefore, based on the droplet distributions on a hydrophobic surface (ACA=110º), an uncoated aluminum surface (ACA=85º), and a hydrophilic surface (ACA=65º), the appropriate initial conditions for frost thickness and density were calculated. In Figure 4.21, the initial density is plotted from the cold plate surface (z=0) to the maximum height of droplets on the surface. The hydrophilic surface has a higher area covered by condensed droplets than both the uncoated and the hydrophobic samples. Therefore, it has the maximum density near the surface (z=0). However, since the droplets on the hydrophilic surface are mainly smaller than the uncoated surface and due to curvature effects, the density inside the layer of frozen droplets decreases faster. The hydrophobic surface has the lowest total area ratio covered by condensed droplets and therefore has the smallest density near the surface. In addition, the maximum droplet height on the hydrophobic surface is significantly higher than more hydrophilic surfaces, which makes the initial thickness higher on this surface.

The evolution of frost thickness and density with time for all 3 surfaces (at conditions of run1) are presented in Figure 4.22 and 4.23. In addition, since the model assumes dropwise condensation on the surface, it does not apply for complete-wetting surfaces (CA=0^o). Therefore, only experimental data for a complete-wetting surface are presented. Results show that initially a denser frost layer grows on the complete-wetting surface. A denser layer has a higher thermal conductivity Therefore, the more hydrophilic the surface, the denser the frost layer growing on it. The model successfully predicts the effect of the surface wettability on frost thickness and density. However, the model is constrained by the assumption of steady-state size distribution of frozen droplets at the beginning of the frosting cycle.

At high cooling rates, small droplets of approximately uniform size and shape freeze on the surface. Therefore, the initial frost thickness is much lower than the low cooling rate initial thickness. Consequently, initial conditions of frost thickness and density (20 μm and 30 kg/m^3 respectively) suggested by Parker and Jones (1975) were used in the model to simulate the initial droplet distribution at high cooling rates. As shown in Figures 4.24 and 4.25, using Parker and Jones initial conditions, the model results are in good agreement with the high cooling rate scheme experimental results of frost thickness and density.

4.4 Conclusions

In this chapter, a model for frost growth on flat plates was presented. The model assumes that the steady-state droplet size distribution suggested by Graham (1973) is realized on the surface prior to freezing. Model predictions were compared to experimental data for frost thickness and density on vertically oriented flat surfaces with differing surface wettability. The significant findings are summarized as follows:

(1) Assuming saturation boundary condition for water vapor at the frost surface results in a water vapor density that is lower than the saturation density at the corresponding temperature. Therefore, it is phyically impossible for the frost layer to grow under such conditions: the assumption is invalid.

(2) Unlike super-saturation models that depend strongly on the prescribed value of the super-saturation degree, the current model is less sensitive to the value of the mass transfer conductance ε_{fst}.

(3) A parametric study shows that the mass transfer conductance ε_{fst} has to be on the order of 100 or higher for the water vapor density inside the frost layer to have realistic values.

(4) During the early frost growth period, the model predicts a decrease in density under certain environmental conditions which agrees with the experimental findings by Hayashi (1977).

(5) Under the same conditions, the frost layer growing on a hydrophilic sample has higher density as compared to more hydrophobic samples.

(6) The effect of the surface wettability becomes less significant after two hours of the frosting cycle.

(7) Parker and Jones intial conditions of frost thickness and density work well for predicting the evolution of frost properties at high initial cooling rates.

4.5 Figures and Tables

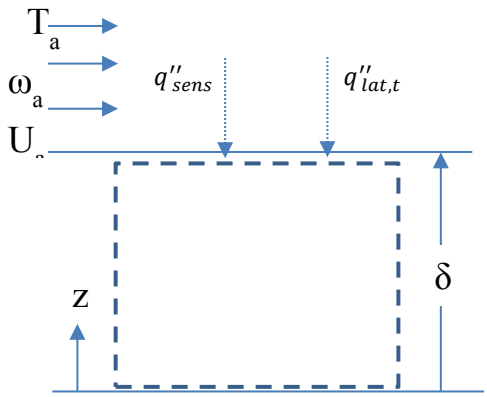

Figure 4.1 Heat balance on the frost layer

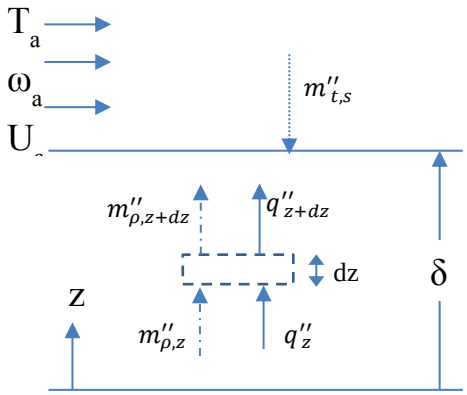

Figure 4.2 Mass balance within the frost layer

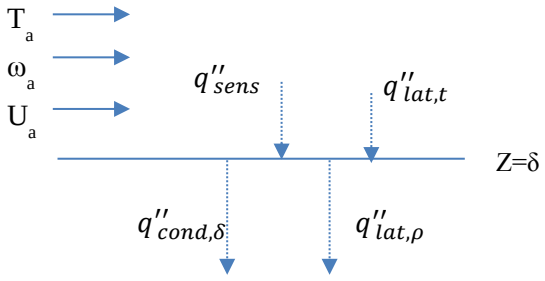

Figure 4.3 Heat balance at the frost surface

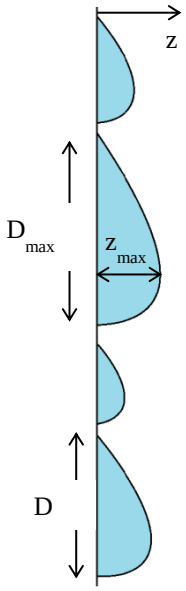

Figure 4.4 Droplet distribution

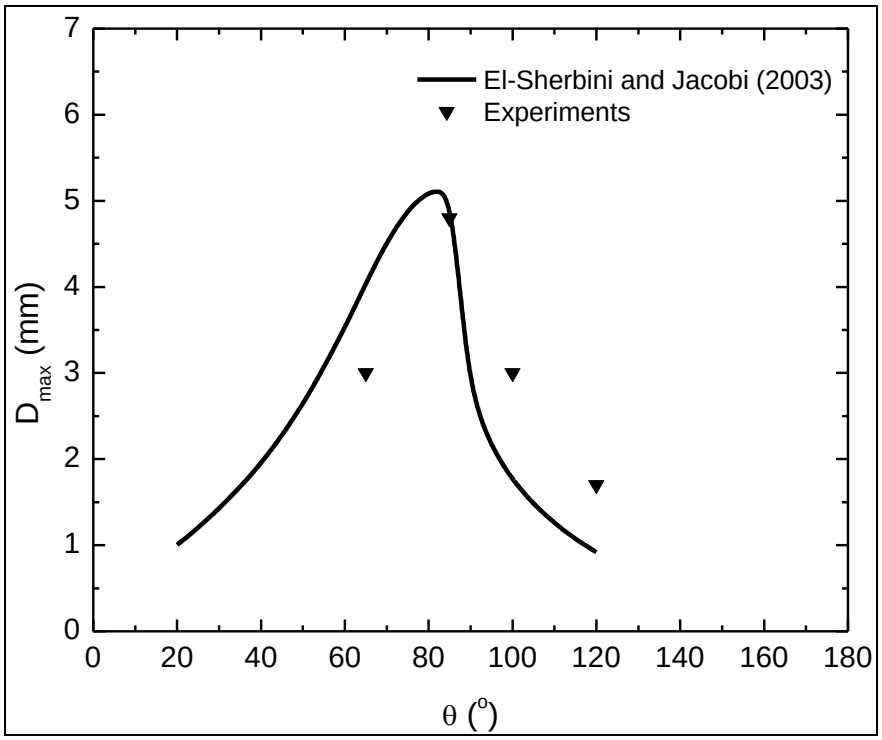

Figure 4.5 Maximum droplet diameter

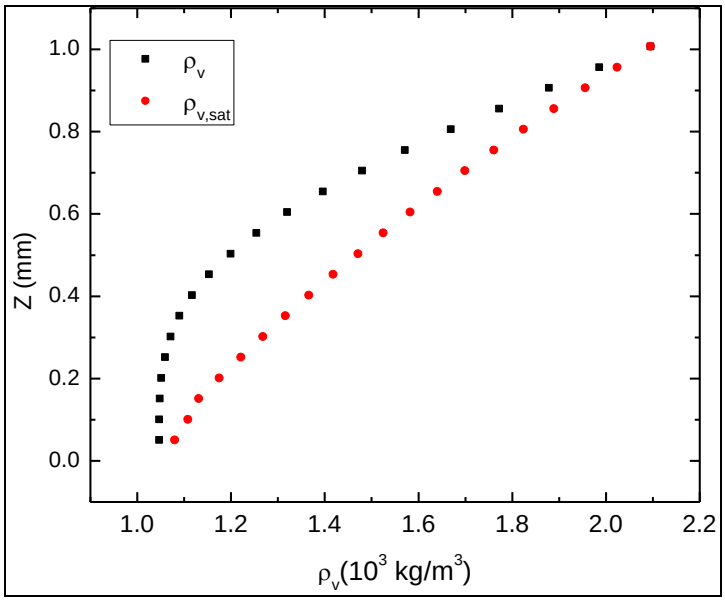

Figure 4.6 Water-vapor density variation within the frost layer

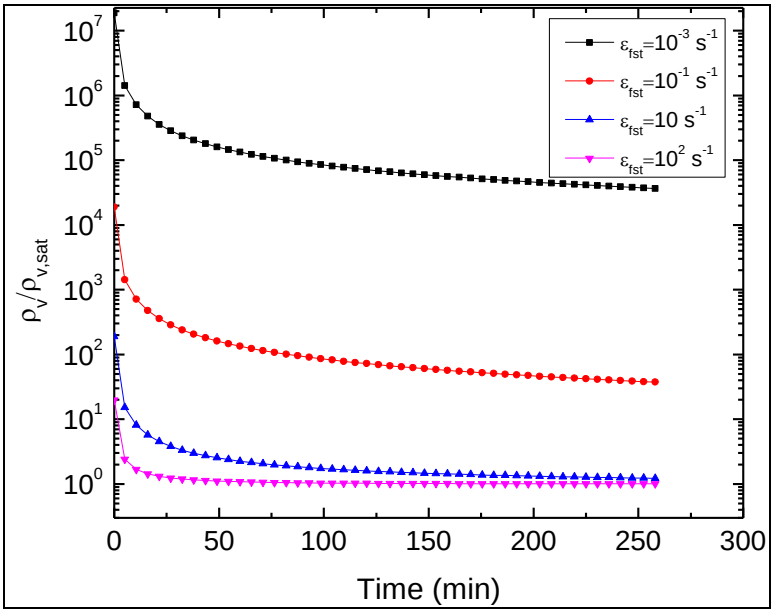

Figure 4.7 Water vapor density at the center of the frost layer for various values of ε_{fst}

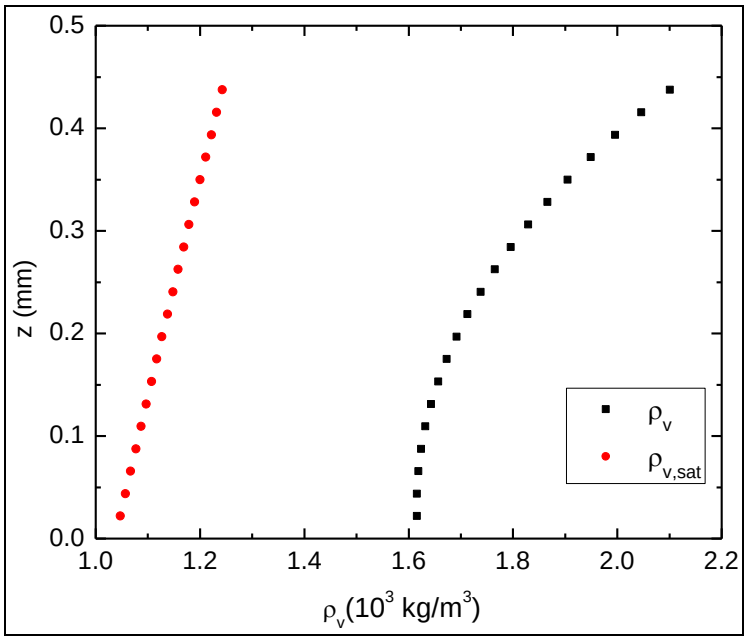

Figure 4.8 Water-vapor density variation within the frost layer

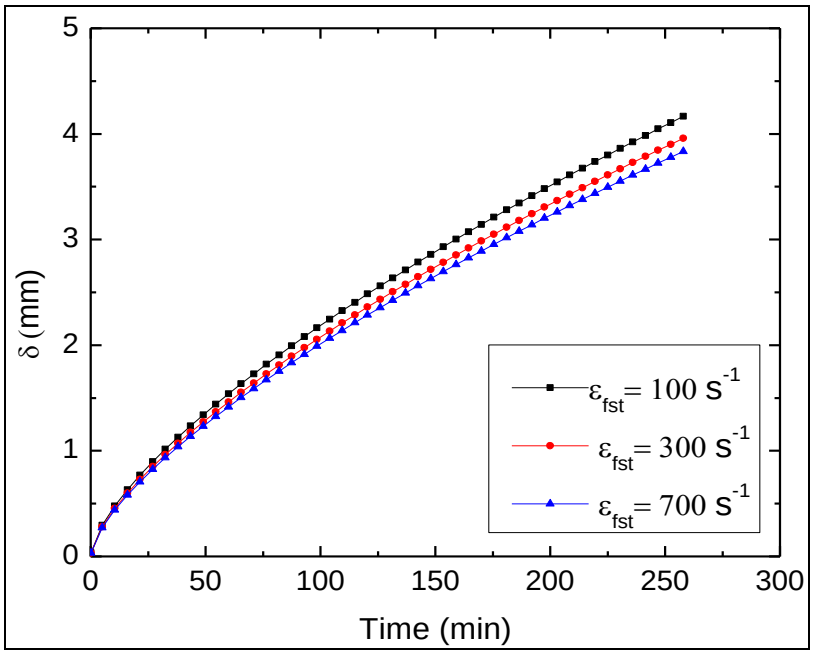

Figure 4.9 Variation of frost thickness with ε_{fst}

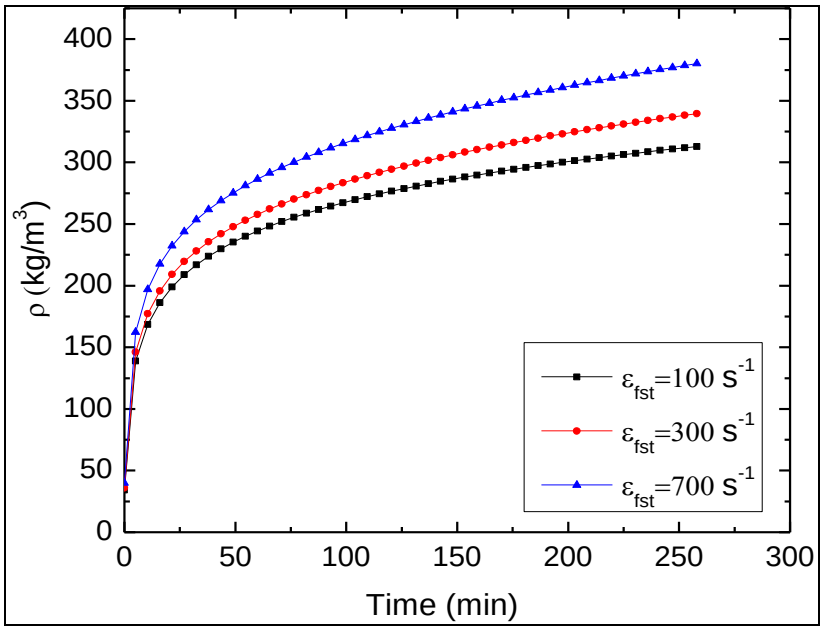

Figure 4.10 Variation of frost Density with ε_{fst}

Figure 4.11 Frozen droplets on a cold surface

Figure 4.12 Frost crystals growing on top of the frozen droplets

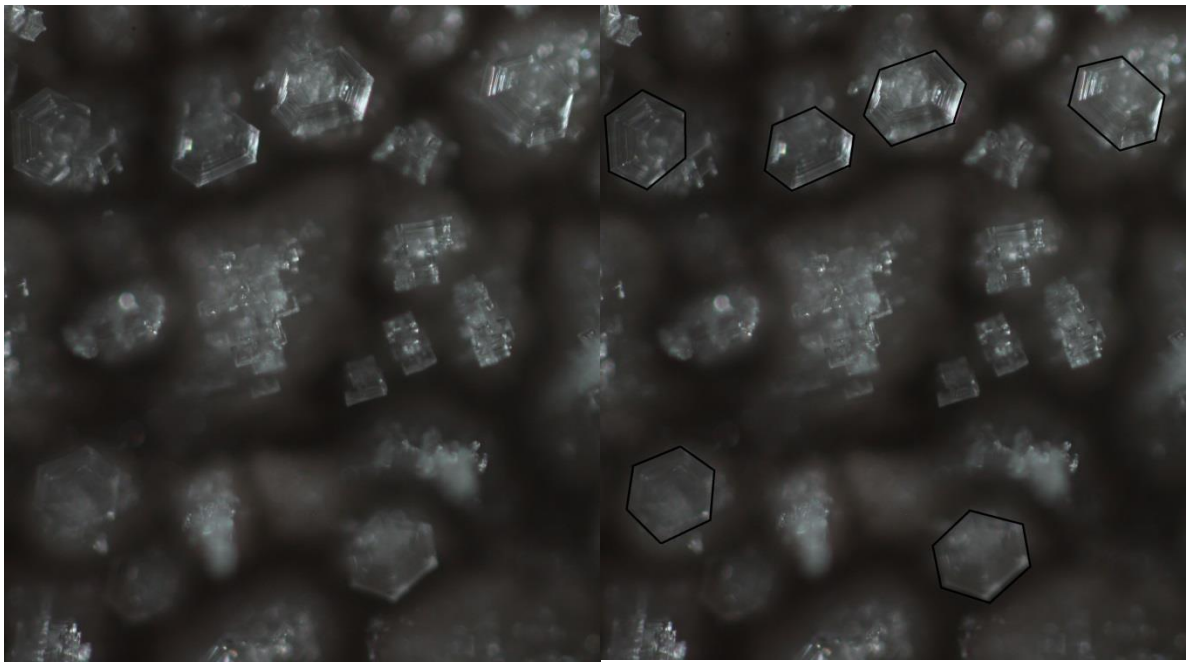

Figure 4.13 Original image of frost crystals (Left) and image with traced crystal edges (right)

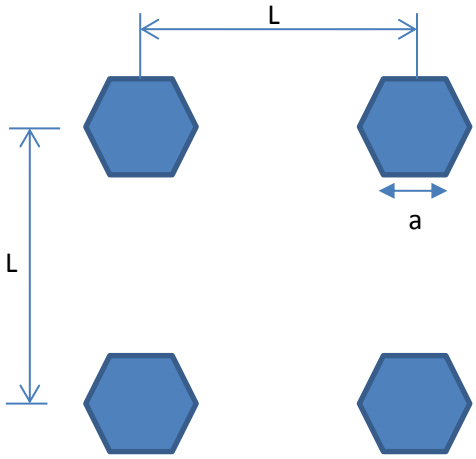

Figure 4.14 Top view for the frost layer modeled as a porous medium

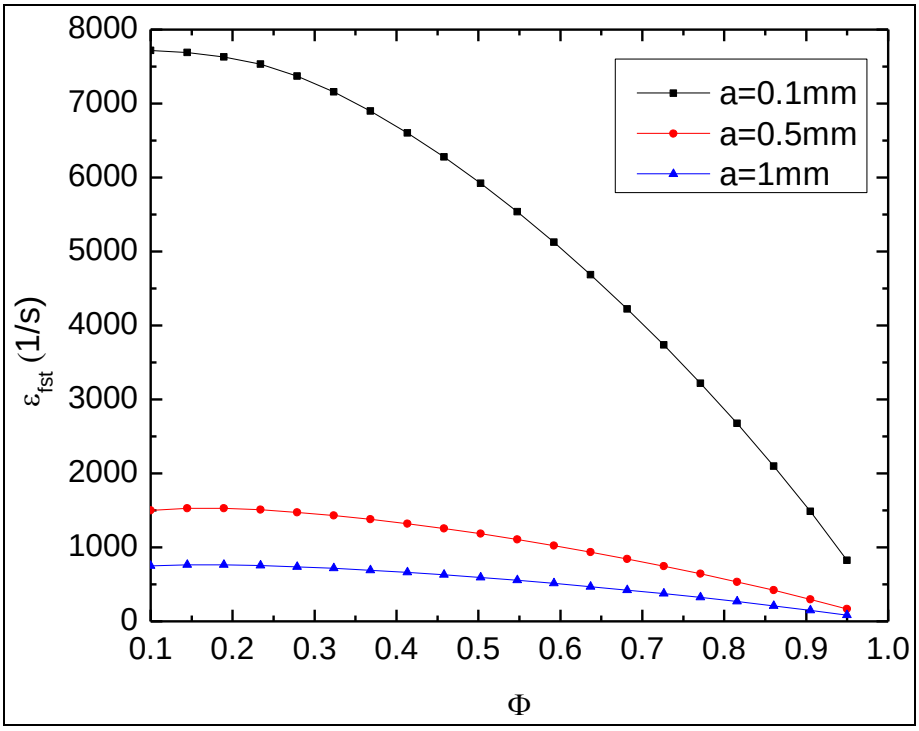

Figure 4.15 Predicted values of the mass transfer conductance

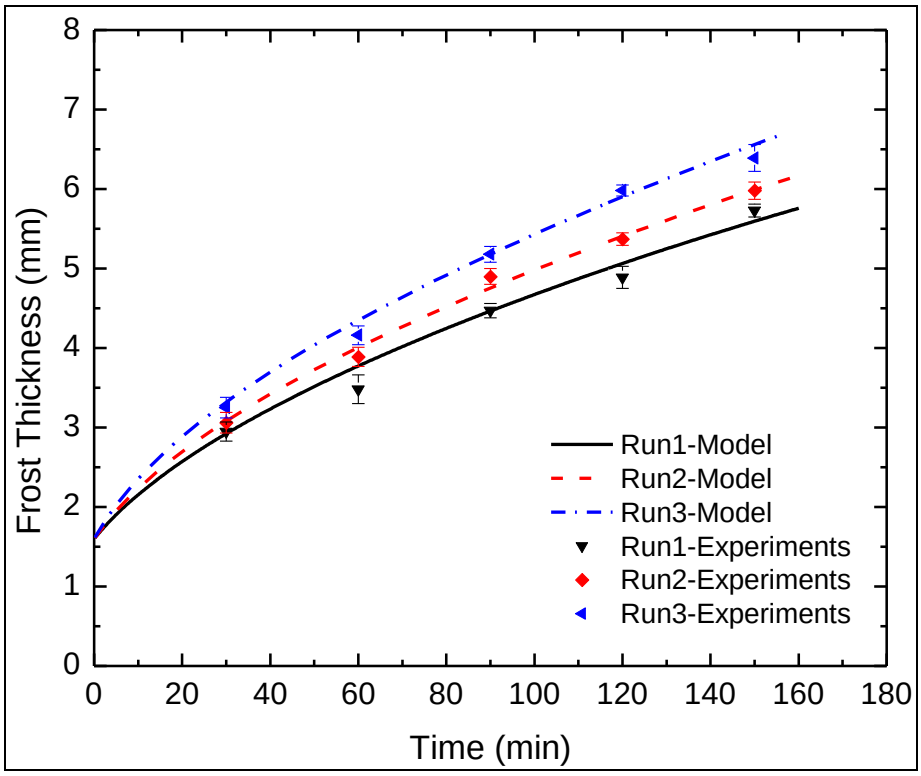

Figure 4.16 Frost thickness at various environmental conditions

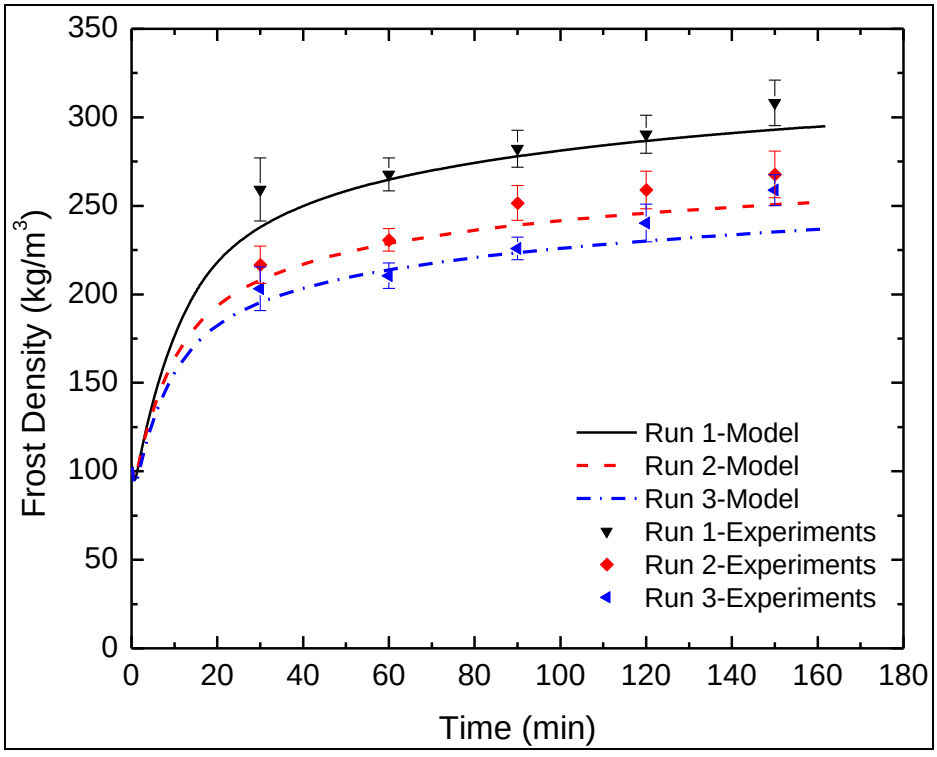

Figure 4.17 Frost density at various environmental conditions

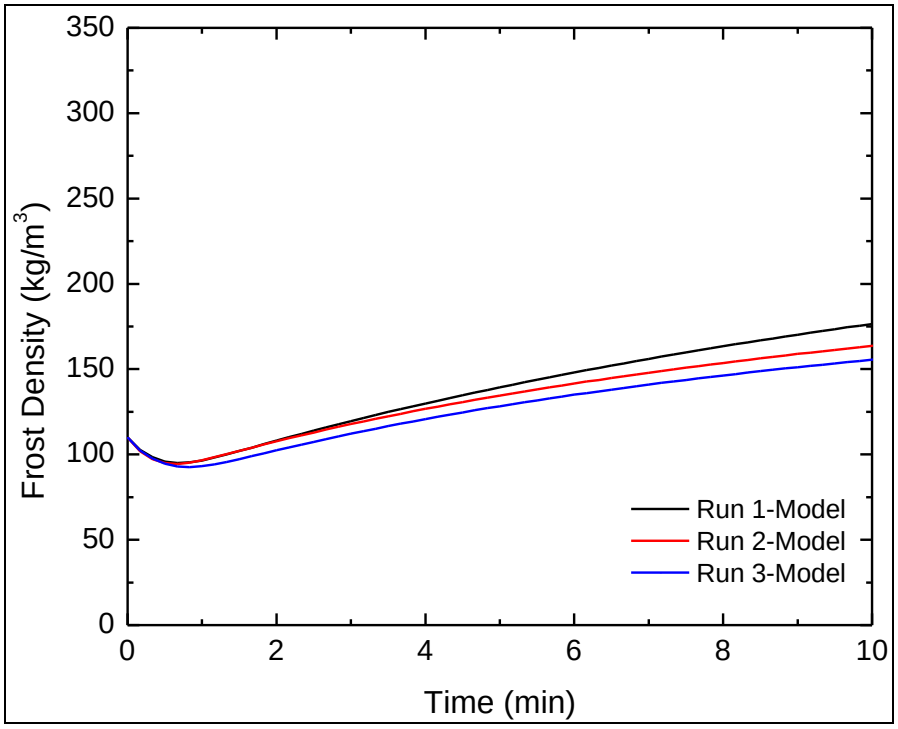

Figure 4.18 Frost density during early frost growth period

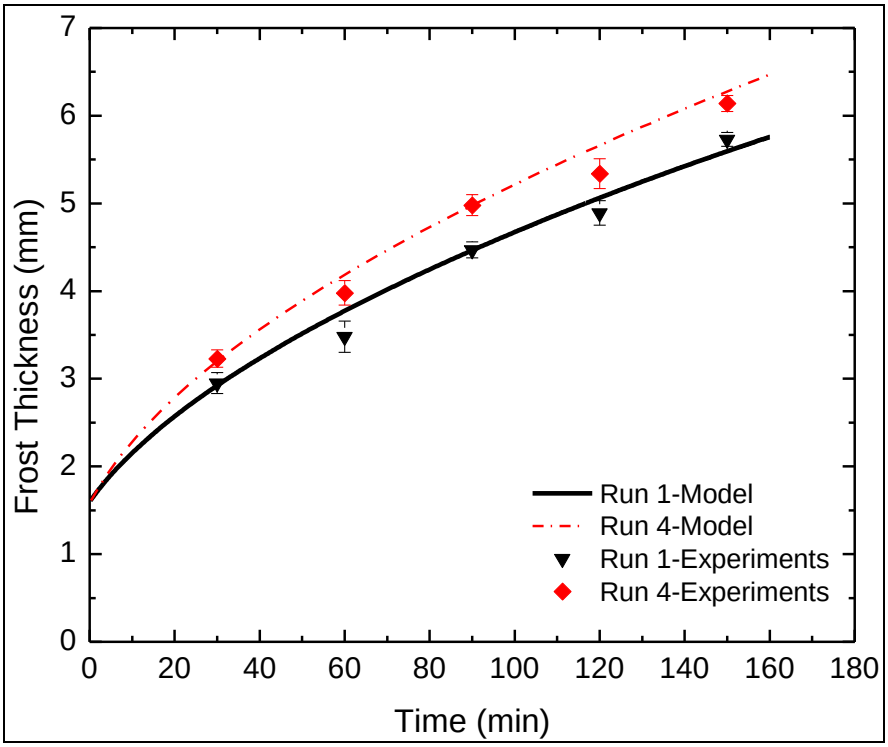

Figure 4.19 Effect of plate temperature on thickness at conditions of run 1(Table 4.1)

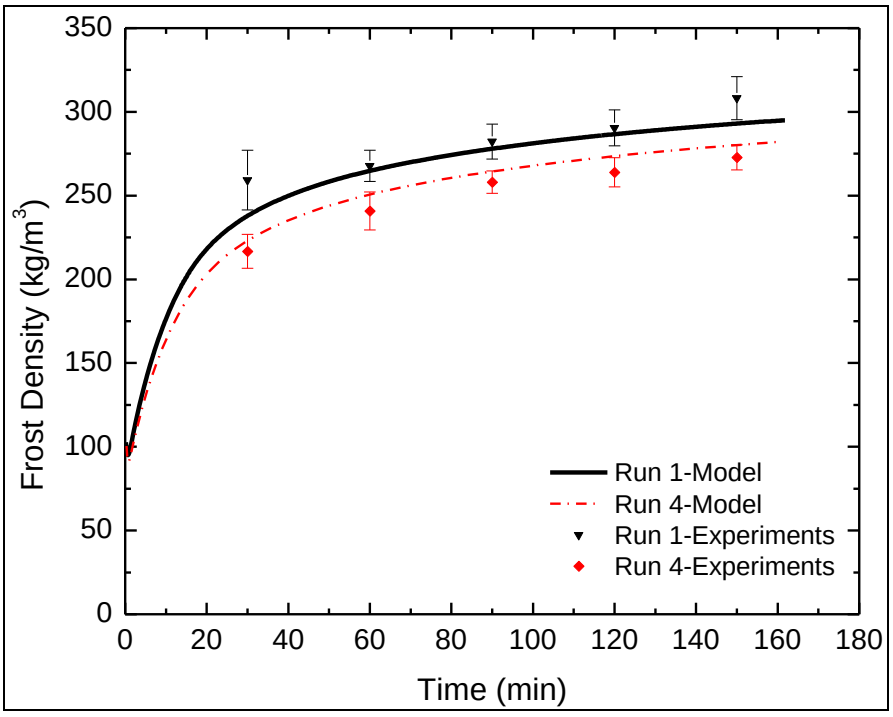

Figure 4.20 Effect of plate temperature on frost density at conditions of run 1 (Table 4.1)

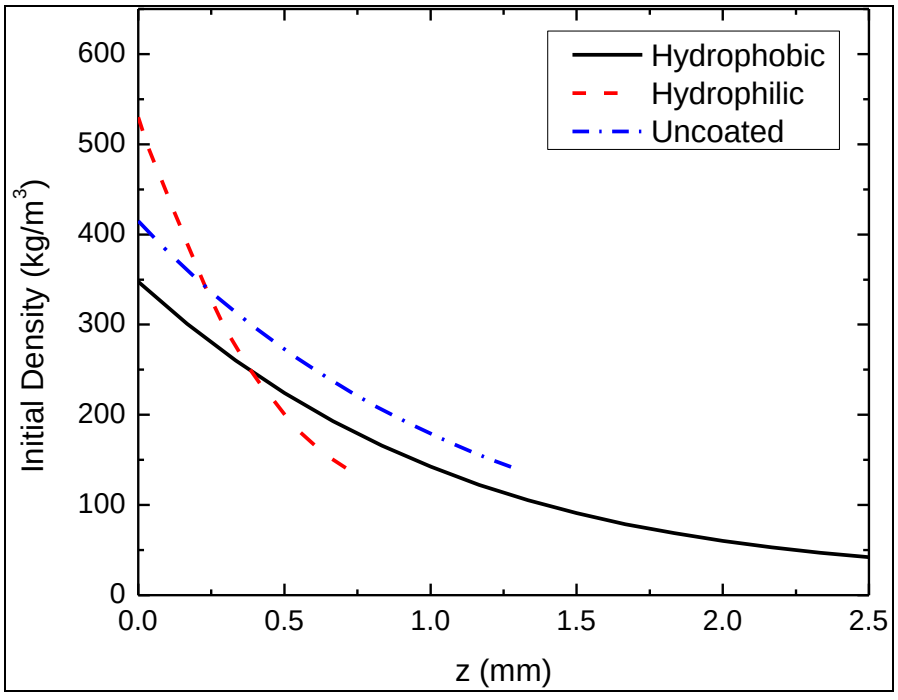

Figure 4.21 Initial frost density for hydrophilic, hydrophobic and uncoated surfaces

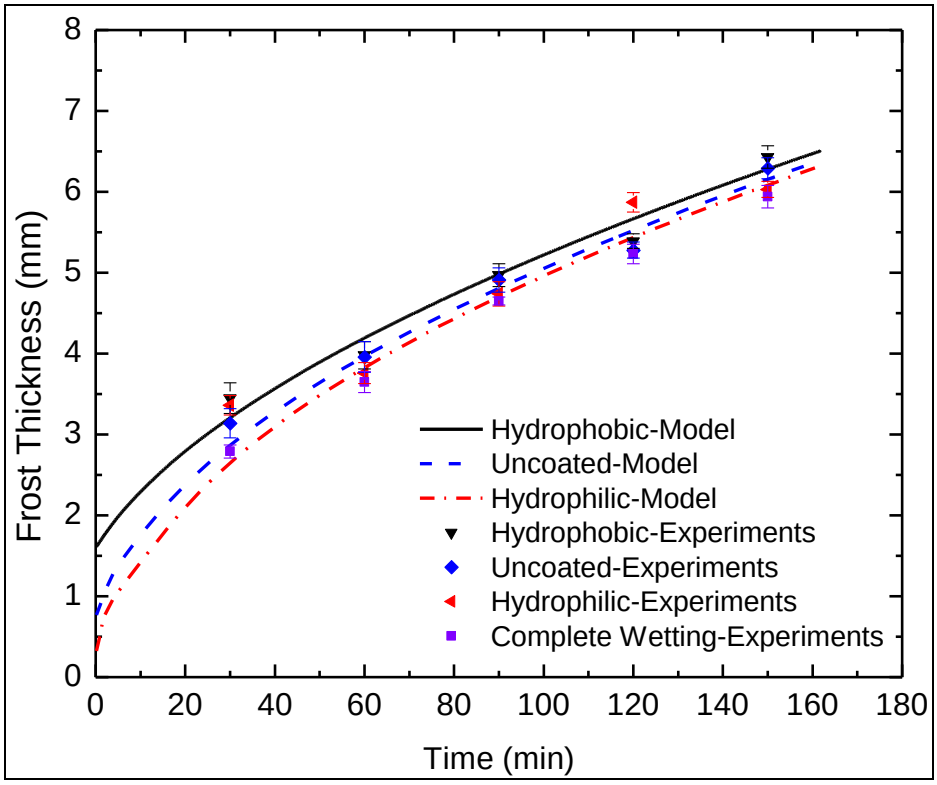

Figure 4.22 Effect of surface wettability on frost thickness at conditions of run 1 (Table 4.1)

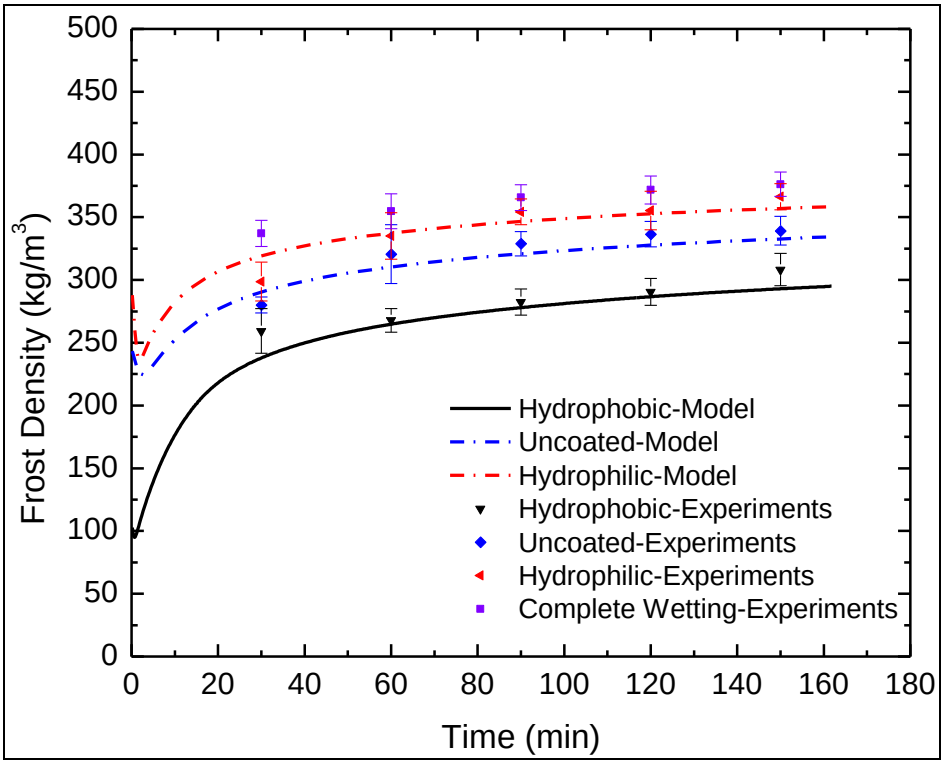

Figure 4.23 Effect of surface wettability on frost density at conditions of run 1 (Table 4.1)

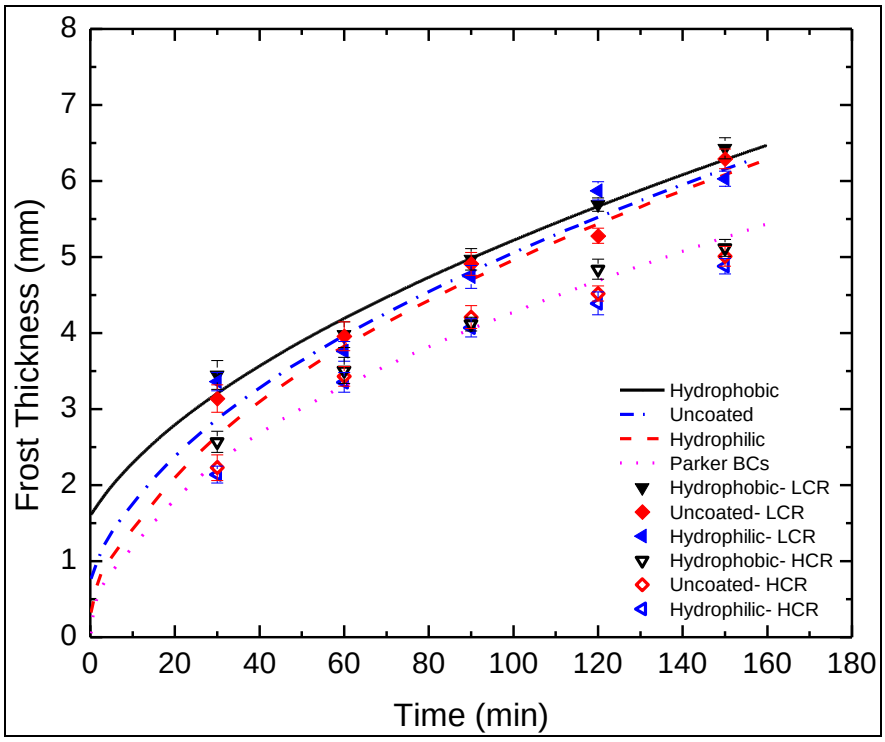

Figure 4.24 Effect of surface wettability on frost thickness at high and low cooling rates at conditions of run 1(Table 4.1)

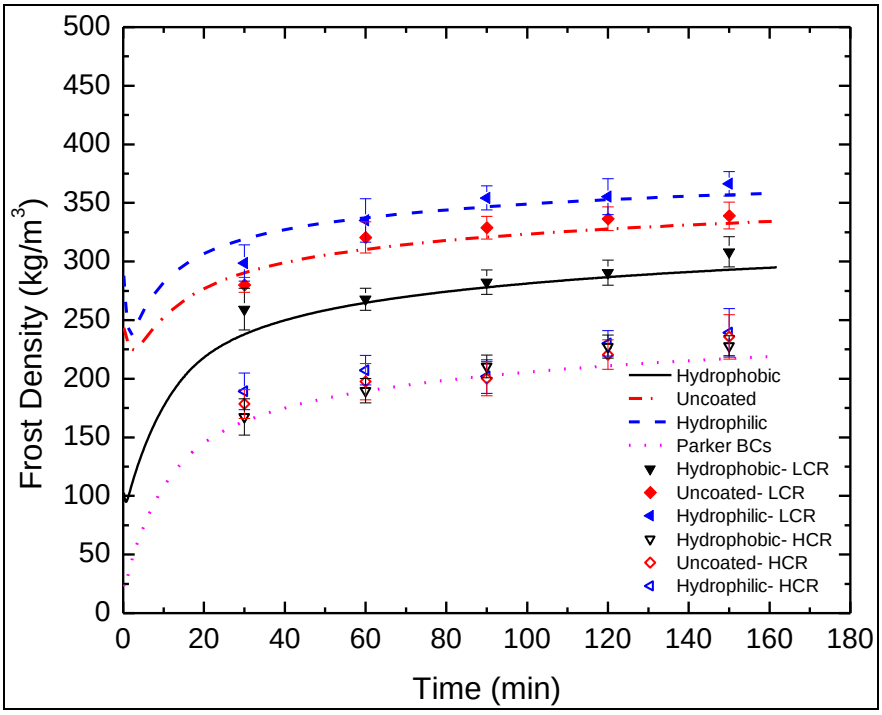

Figure 4.25 Effect of surface wettability on frost density at high and low cooling rates at conditions of run 1(Table 4.1)

Table 4.1 Experimental conditions used to validate the model

Run	**1**	**2**	**3**	**4**
Air Temperature (ºC)	**17**	**17**	**12**	**17**
Relative Humidity (%)	**60**	**78**	**78**	**60**
Plate Temperature (ºC)	**-15**	**-15**	**-15**	**-18**
Air Velocity (m/s)	**1.1**	**1.1**	**1.1**	**1.1**

Table 4.2 Experimental conditions for the frost crystal shape experiments

Run	**a**	**b**	**c**	**d**	**e**
Air Temperature (ºC)	**19**	**19**	**19**	**19**	**19**
Relative Humidity (%)	**60**	**78**	**60**	**78**	**60**
Plate Temperature (ºC)	**-15**	**-15**	**-5**	**-5**	**-18**

CHAPTER 5

CONCLUSIONS

5.1 Summary of Results

The frost growth and densification rates on vertical flat plates with manipulated wettability were studied. The effect of surface wettability on frost thickness and density was experimentally investigated. A mathematical model based on the assumption of dropwise condensation on the surface was developed. The impact of the surface wettability was included in the model through initial conditions for frost thickness and density. The study can serve to guide the design of heat exchangers operating under frosting conditions.

5.1.1 Wettabiliy Impact on Frost Thickness and Density

Through wind-tunnel experiments with flat aluminum plates of identical size and geometry but with differing surface wettability, it was observed that under the same operating conditions, a denser frost layer grows on more hydrophilic surfaces. The surface wettability impact was more significant when the condensation period was long and condensed droplets on the surface were allowed to grow and coalesce before freezing occurred. Moreover, the surface wettability impact decreased with time, but remained significant after more than 2 hours of the frosting cycle.

5.1.2 Prediction of Frost Growth on a Flat Plate

A mathematical model for frost growth on vertical flat plates was developed. In the model, the heat flux and the mass transfer conductance inside the frost layer were used as

substitution to the saturation boundary conditions to calculate the water vapor density at the cold plate and the frost surface. A parametric study was undertaken to find an appropriate range for the mass transfer conductance. A simple model for the frost layer as a porous medium was used to find the mass transfer conductance and the model predictions were in the expected range found in the parametric study. Moreover, the surface wettability impact was included in the model through initial conditions of frost thickness and density. The frost growth model successfully predicted the frost properties on surfaces with varying wettabilities when frosting was preceded by a high-cooling-rate condensation period. In addition, the same model used with initial conditions suggested by Jones and Parker (1975) predicted frost thickness and density with reasonable accuracy from the high-cooling-rate condensation phase experiments.

For the design of evaporators operating under frosting conditions, it is recommended to use a hydrophilic coating for the fins, since the denser frost layer has a higher thermal conductivity and is not as thick. Therefore, it results in slower heat transfer degradation with time. In addition, the lower thickness results in a lower pressure drop caused by frost layer blocking the air flow. Moreover, due to the superior water drainage behavior of hydrophilic surfaces, the increase in frost thickness and density during the second frosting cycle is insignificant. Nevertheless, more work should be done on the long-term performance of super-hydrophilic surfaces after successive frosting and defrosting cycles.

5.2 Future Research Recommendations

Recent technologies have made possible the manipulation of surface wettability through chemical coating or surface morphology (nanostructures and microstructures). The heat exchanger fin design can benefit from such technologies to control the frost growth and therefore reduce the

necessity of frequent defrosting. The model developed in this work can be used to predict the frost layer growth on a heat exchanger fin. Therefore, the next proposed step is developing a model for to predict the thermal-hydraulic performance of evaporators with varying surface wettabilities under frosting conditions.

Karmouch and Ross (2010) conducted an experimental study of the evolution of water contact angle with temperature near the freezing point. During their experiments, no change in the advancing and receding contact angles as a function of temperature was observed for polished silicon, polished aluminum, roughened silicon, gold, high density polyethylene, PTFE (polytetrafluoroethylene), and PMMA (poly(methyl methacrylate)). On the other hand, both the advancing and receding contact angles decrease and the hysteresis increases at temperatures below 5°C for all nanostructured materials used in their study. Therefore, since the suggested model in this work that does not take into account the changes in contact angle near the freezing point, it does not work for nanostructured surfaces. Developing a similar model for nanostructured superhydrophobic surfaces would also be beneficial for designing heat exchangers operating under frosting conditions.

The absence of detailed studies of the frost layer morphology and frost crystal shapes and sizes, poses challenges in modeling heat and mass transfer coefficients inside a frost layer. In this work, the frost layer was modeled as a porous medium consisting of ice rods separated by moist air. However, this approach oversimplifies the structure of the frost layer and neglects the branching from the main rods during the mature frost growth period. Therefore, it is recommended to study the morphology of the frost layer and develop more accurate models for frost thermal conductivity and heat and mass transfer coefficients inside a frost layer.

BIBLIOGRAPHY

Barzanoni, Y., Basirat Tabrizi, H., Noorshams, O., and Eftekhari, H., 2012, Correlation for frost properties on a cold cylinder surface in cross flow, *Heat Mass Transfer*, 48, pp. 1477-1484.

Bauer, T.H., 1993, A general analytical approach toward the thermal conductivity of porous media, *Int. J. Heat Mass Transfer*, 36 (17), pp. 4181-4191.

Cai, L., Wang, R., Hou, P., and Zhang, X., 2011, Study on restraining frost growth at initial stage by hydrophobic coating and hygroscopic coating, *Energy and Buildings*, 43, pp. 1159-1163.

Cheng C.H., Cheng Y.C., 2001. Predictions of frost growth on a cold plate in atmospheric air, *Int. Commun. Heat Mass Transfer*, 28, pp. 953-962.

Cheng, C.H, and Wu, K.H, 2003, Observations of early-stage frost formation on a cold plate in atmospheric air flow, *Int. J. Heat Tansfer*, 125 (1), pp. 95-102.

El-Sherbini, A. I. and Jacobi, A. M., 2003, Modeling condensate drops retained on the air-side of heat exchangers, *Technical report*, University of Illinois, Urbana-Champaign.

Fossa, M., and Tanda, G., 1988, Prediction of growth rate and density of frost layer developing under forced convection, Wfirme- und Stoffiibertragung, 22, pp. 285-290.

Fossa, M., and Tanda, G., 2002, Study of free convection frost formation on a vertical plate, *Experimental Thermal and Fluid Science*, 26, pp. 661-668.

Graham, C., and Griffith, P., 1973, Drop size distribution and heat transfer in dropwise condensation, *Int. J. Heat Mass Transfer*, 16, pp. 337-346.

Han, H.D, and Ro, S.T, 1999, The characteristics of frost growth on parallel plates, Lecture Notes in Physics, Springer, Germany, 533, pp. 55-64.

Hayashi, Y., Aoki, A., Adashi S., and Hori, K., 1977, Study of frost properties correlating with frost formation types, *ASME Journal of Heat Transfer*, 99, pp. 239-245.

Hermes, C.J.L., Picucco, R.O., 2009, Barbosa, R. J., and Melo, C., A Study of frost growth and densification on flat Surfaces, *Experimental Thermal and Fluid Science*, 33, pp. 371-379.

Hoke J. L., Georgiadis, J. G., and Jacobi, A. M., 2000, The Interaction between the Substrate and Frost through Condensate Distribution, *Technical report*, University of Illinois, Urbana-Champaign.

Hoke, J.L., Georgiadis, J.G., and Jacobi, A.M., 2004, The effect of substrate wettability on frost properties, *Journal of Thermophysics and Heat Transfer*, 18 (2), pp. 228-235.

http://www.its.caltech.edu/~atomic/snowcrystals/primer/primer.htm.

Huang, L., Liu, Z., Liu, Y., Gou, Y., and Wang, J., 2009, Experimental study on frost release on fin-and-tube heat exchangers by use of a novel anti-frosting paint, *Experimental Thermal and Fluid Science*, 33, pp. 1049-1054.

Incropera, F.P., DeWitt, D.P., 2002, Fundamentals of heat and mass transfer, John Wiley and Sons, New York, USA, pp. 981.

Jhee, S., Lee, K. S., and Kim, W. S., 2002, Effect of surface treatments on the frosting/defrosting behavior of a fin-tube heat exchanger, *Int. J. Ref.*, 25, pp. 1047-1053.

Jones, B.W., and Parker, J.D., 1975, Frost formation with varying environmental parameters, *J. Heat Transfer*, 97, pp. 255-259.

Kandula, M., 2011, Frost growth and densification in laminar flow over flat surfaces, *Int. J. Heat Mass Transfer*, 54, pp. 3719-3731.

Karmouch, R., and Ross, G. G., 2010, Experimental study on the evolution of contact angles with temperature near the freezing point, *J. Phys. Chem. C*, 114, pp. 4063-4066.

Kim, K., and Lee, K. S., 2011, Frosting and defrosting characteristics of a fin according to surface contact angle, *Int. J. Heat Mass Transfer*, 54, pp. 2758-2764.

Kim, K., and Lee, K. S., 2012, Characteristics and performance evaluation of surface-treated louvered-fin heat exchangers under frosting and wet conditions, *Int. J. Heat Mass Transfer*, 55, pp. 6676-6681.

Kim, K., Kim, J. S., and Lee, K. S., 2010, Characteristics of frost formation on two-dimensional fins and its empirical correlations, *Int. J. Heat Mass Transfer*, 53, pp. 2670-2675.

Kobayashi, T., Kuboda, T., and Sungagawa, I., Snow Crystals, Morphology of Crystals, *Terra Scientific Publishing Company*, Tokyo, 1987, pp. 649–743.

Le Fevre, and E.J., Rose, J.W., 1965, An experimental study of heat transfer by dropwise condensation, *Int. J. Heat Mass Transfer*, 8, pp. 1117-1133.

Le Gall, R., and Grillot, J.M., 1997, Modeling of frost growth and densification, *Int. J. Heat Mass Transfer*, 40 (13), pp. 3177-3187.

Lee K.S., Kim W.S., Lee T.H., 1997, A one-dimensional model for frost formation on a cold flat surface, *Int. J. Heat Mass Transfer*, 40 (18), pp. 4359-4365.

Lee Y. B., Ro S. T., 2001, An experimental study of frost formation on a horizontal cylinder under a cross flow, *Int. J. Refrig.*, 24, pp. 468-474.

Lee, H., Shin, J., Ha, S., Choi, B., and Lee, J., 2004, Frost formation on a plate with different surface hydrophilicity, *International Journal of Heat and Mass Transfer*, 47, pp. 4881–4893.

Lee, K.S., Jhee, S., and Yang, D.K., 2003, Prediction of the frost formation on a cold flat surface, *Int. J. of Heat Mass Transfer*, 46 (20), pp. 3789-3796.

Lee, Y.B., and Ro, S.T., 2005, Analysis of the frost growth on a flat plate by simple models of saturation and supersaturation, *Exp. Thermal Fluid Sc.*, 29, pp. 685-696.

Liu, L., and Jacobi, A. M., 2006, The effects of hydrophilicity on water drainage and condensate retention on air-conditioning evaporators, *11th International Refrigeration and Air Conditioning Conference at Purdue*, West Lafayette, IN.

Liu, Z., Wang, J., Zhang, X., Meng, S., and Ma, C., 2006, An experimental study on minimizing frost deposition on a cold surface under natural convection conditions by use of a novel anti-frosting paint. Part II. Long-term performance, frost layer observation and mechanism analysis, *Int. J. Ref.*, 29, pp. 237-242.

Maa, J.R., 1978, Drop size distribution and heat flux of dropwise condensation, *The Chemical Engineering Journal*, 16 pp. 171-176.

Marion, A., 1991, An Introduction to image processing, Chapman and Hall, London, UK, Chap. 5.

Mills, A.F., 2001, Mass Transfer, Prentice Hall PTR, New Jersey, USA, pp. 984.

Moallem, E., Cremaschi, L., Fisher, D. E., and Padhmanabha, S., 2012, Experimental measurements of the surface coating and water retention effects on frosting performance of microchannel heat exchangers for heat pump systems, *Experimental Thermal and Fluid Science*, 39, pp. 176-188.

Na, B., and Webb, R., 2004a, Mass transfer on and within a frost layer, *International Journal of Heat and Mass Transfer*, 47, pp. 899-911.

Na, B., and Webb, R., 2004b, New model for frost growth rate, *Int. J. Heat Mass Transfer*, 47, pp. 925-936.

Nawaz, K., Bock, J., and Jacobi, A.M., 2012, Thermal-hydraulic performance of metal foam heat exchangers, *14th International Refrigeration and Air Conditioning Conference*, West Lafayette, IN.

Nikulshina, D.G., Popova, E.M., Dol'skaya, V.I, Izotov, V.N., Luchin, V.A., and Starikh, Y.V., 1979, The study of the influence of hydrophobic coating on thermal and aerodynamic charactersitics of air coolers, *Refrigerating Technique,* 6, pp. 28-30.

O'Neal, D.L., and Tree, D.R, 1985, A review of frost formation in simple geometry, ASHRAE Trans, 91, pp. 267-281.

Östin, R. and Anderson, S., 1991, Frost growth parameters in a forced air stream, *International Journal of Heat and Mass Transfer*, pp. 1009- 1017.

Ostin, R., and Anderson, S., 1991, Frost growth parameters in a forced air stream, *Int. J. Heat Mass Transfer*, 14, pp.1009-17.

Phanikumar, M. S., and Mahajan R. L., 2002, Non-Darcy natural convection in high porosity metal foams, *Int. J. Heat Mass Transfer*, 45, pp. 3781-3793.

Rose, J.W., and Glickman, L.R., 1973, Dropwise condensation-The distribution of drop sizes, *Int. J. Heat Mass Transfer*, 16, pp. 411-425.

Sahin, A, 1994, An experimental study on the initiation and growth of frost formation on a horizontal plate, *Experimental Heat Transfer*, 7, pp. 101-119.

Sanders, C.T., 1974, The influence of frost formation and defrosting on the performance of air coolers, *Ph.D. Thesis*, Technische Hogeschool, Delft, Netherlands.

Seki, N., Fukusako,, S., Matsuo, K., and Uemura, S., 1984, Incipient phenomena of frost formation, Bull. JSME, 27, pp. 2476–2482.

Sherif, S. A., Raju, S. P., Padki, M. M., and Chan, A. B., 1993, A semi-empirical transient method for modelling frost formation on a flat plate, *Rev. Int. Froid,* 16, pp. 321-329.

Shin, J., Tikhonov, A. V., and Kim, C., 2003, Experimental study on frost structure on surfaces with different hydrophilicity: Density and thermal conductivity, *Journal of Heat Transfer*, 125, pp. 84-94.

Tao, Y.X., Besant, R.W., and Rezkallah, K.S., 1993, A mathematical model for predicting the densification and growth of frost on a flat plate, *Int. J. Heat Mass Transfer*, 36 (2), pp. 353-363.

Tokura, I., Saito, H., and Kishinami, K., 1983, Study on properties and growth rate of frost layers on cold surfaces, *J. Heat Transfer*, 105, pp. 895-901.

Wang, W., Guo, Q.C., Lu, W.P., Feng, Y.C., and Na, W., 2012, A generalized simple model for predicting frost growth on cold flat plat, *Int. J. Ref*., 35, pp. 475-486

Wu, W.H., and Maa, J.R., 1976, On the heat transfer in dropwise condensation, *The Chemical Engineering Journal*, 12, pp. 225-231.

Wu, Y. T., Yang, C. X., and Yuan, X. G., 2001, Drop distributions and numerical simulation of dropwise condensation heat transfer, *Int. J. Heat Mass Transfer*, 44, pp. 4455-4464.

Xianghong, G., 2008, Dimensionless correlations of frost properties on a cold plate, The 3rd International Conference on Innovative Computing Information and Control.

Yang, D. K., and Lee K.S., 2005, Modeling of frosting behavior on a cold plate, *Int. J. Refrigeration*, 28, pp. 396-402.

Yang, D. K., and Lee, K. S., 2004, Dimensionless correlations of frost properties on a cold plate, *Int. J. Refrig.*, 27, pp. 89-96.

Yonko, J. D., and Sepsy, C. F., 1967, An investigation of the thermal conductivity of frost while forming on a flat horizontal plate, *ASHRAE Transactions*, 73, pp. 1.1-1.11.

Yun, R., Kim, Y., and Min, M.K., 2002, Modeling of frost growth and frost properties with air flow over a flat plate, *Int. J. Ref.*, 25, pp. 362-371.

Zukauskas, A., convective heat transfer in cross-flow, In: Handbook of single-Phase heat transfer, S. Kakac, *et al.*, 1987, Wiley, New York.

Appendix A: Image Processing

A.1 Image Processing Methodology

In order to detect the edges of the frozen droplets and calculate their projected areas on the cold plate, the "Threshold" tool in Photoshop was used. This tool is used to convert a grayscale image to a binary image. In the output image, all pixels in the input image with luminance greater than the threshold are replaced with the value 1 (white) and all other pixels with the value 0 (black). Changing the threshold value can significantly affect the output image. Therefore, obtaining accurate values of the traced droplet area highly depends on finding the appropriate threshold value. A histogram can be used to decide what value of threshold to use when converting a grayscale image to a binary one by thresholding. If the image is suitable for thresholding, then the histogram will be *bi-modal* (i.e. the pixel intensities will be clustered around two well-separated values) (Marion, 1991) and a suitable threshold will be found somewhere in between the two peaks of the histogram. Otherwise, it is unlikely that a good segmentation can be produced by thresholding.

Figure A.1 shows an original image of a layer of frozen droplets at the beginning of the frosting cycle. The histogram for this image obtained in Photoshop is shown in Figure A.2. A range of threshold values was tried and the output images are shown in Figure A.3. Since the original image histogram is not bi-modal, it was expected that tracing the droplet contours by thresholding is not accurate. The main reason for this inaccuracy is the three-dimensional nature of the droplets. Due to curvature effects, the bottom part of the droplet was under shadow and therefore was transformed to a "black" area in the output binary image in contract with the remaining parts of the droplet.

The method used for the droplet count in this work is outlined in Figure A.4. The thresholded and original images were opened simultaneously as 2 separate layers in Photoshop. The opacity of the thresholded image was reduced so that the original image could be seen through it. A brush tool was used to adjust the edge of the frozen droplets, especially from the bottom part which is under shadow as shown in figure A.4.

The impact of the accuracy in tracing the frost edge on the droplet area obtained from counting "white" pixels in the binary image was investigated. For this purpose, several attempts to adjust a droplet edge were made and the resulting areas in pixels and mm^2 were measured and summarized in Table A.1. The maximum difference in the calculated area resulting from the image adjustment error is approximately 9%. Therefore, the method accuracy is satisfactory for droplet counting purposes since all droplets with diameters within 20% of the selected diameter were considered to be of that size.

A.2 Figures and Tables

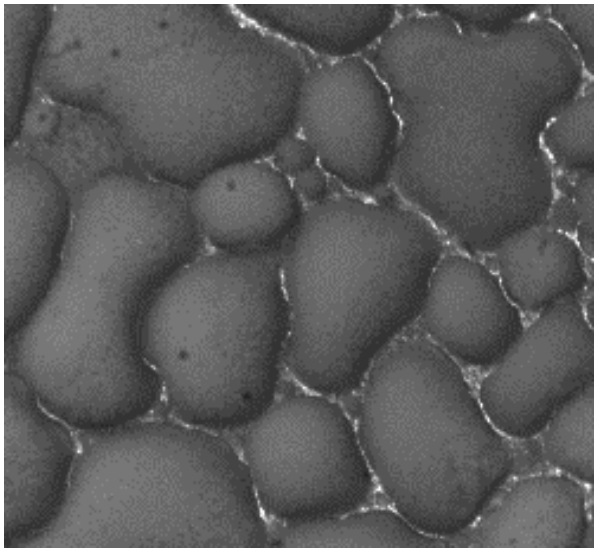

Figure A.1 Image of frozen droplets on an uncoated aluminum surface

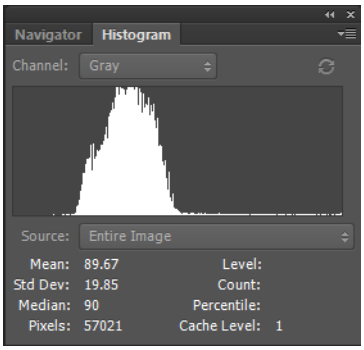

Figure A.2 Image histogram obtained in Photoshop

Figure A.3 Image after segmentation with a threshold of 80 (left) and 90 (right)

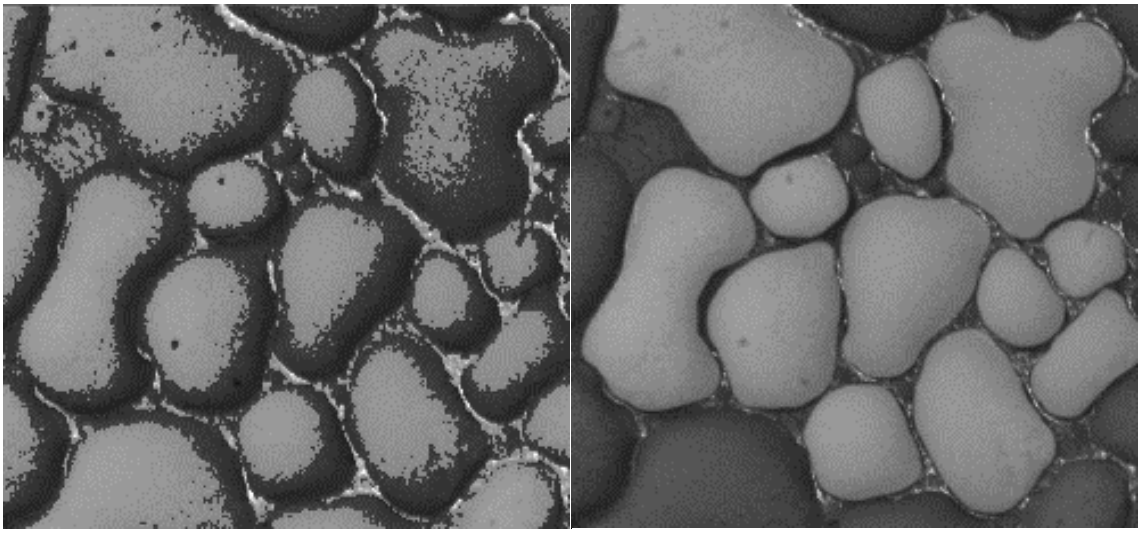

Figure A.4 Binary image with the original image as a background, before (left) and after (right) adjustments

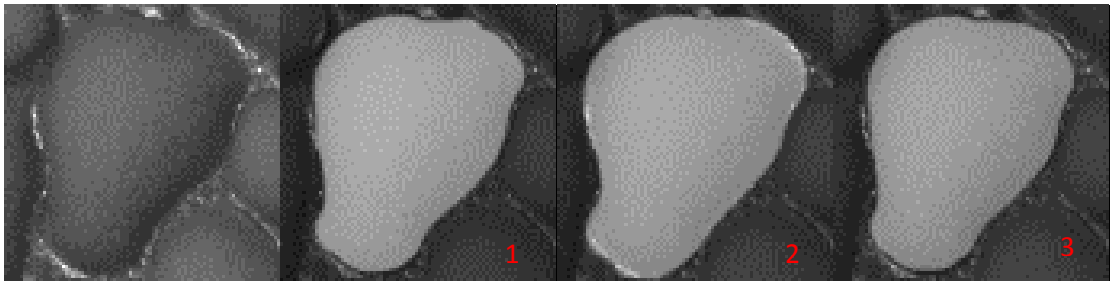

Figure A.5 Binary images of a droplet

Table A.1 Effect of droplet tracing accuracy of the calculated droplet area

Adjustment	Area (pixels)	Area (mm^2)
1	**3826**	**73.58**
2	**4083**	**78.52**
3	**3765**	**72.40**

Appendix B: Program to Calculate Initial Frost Density

```
SUBPROGRAM n_d(D_max, A_cov_s, A_cov_b, B_s: Q_s,Q_b,B_b)
{--Findings constants defining size-distribution functions--}
{Units: D_max is input in mm, D_m is in microns}
D_m=D_max*1000
Q_s=4*10^8*(B_s+3)*A_cov_s/(pi*((0.2*D_m)^(B_s+3)- 20^(B_s+3)))
Q_b=Q_s*(0.2*D_m)^(B_s-B_b)
Q_b=4*10^8*(B_b+3)*A_cov_b/(pi*(D_m^(B_b+3)- (0.2*D_m)^(B_b+3)))
END

{--Findings volume of a droplet--}
MODULE V(alpha_rad, theta_Arad, D: Vol, theta_min )
$COMMON rho, g, Gamma
{--Volume of a drop using the two-circle method--}
Bo=rho*g*sin(alpha_rad)*D^2/Gamma*1e-3 {Bo is non-dim}
theta_min_rad=( 0.01*Bo^2 - 0.155*Bo + .97)*theta_Arad
theta_min_rad=theta_min*pi /180  {radians}
Beta=1+0.096*Bo
L=Beta^.5*D/2

{--Theta Function---}
A=-(2*theta_min_rad-2*theta_Arad)/pi^3
B=-(3*theta_Arad-3*theta_min_rad)/pi^2
zeta=L/(cos(phi)^2+Beta^2*sin(phi)^2)^.5
L_factor=sin(theta_1)/sin(theta_2)*(1-cos(theta_2))/(1-cos(theta_1))
theta_1=A*phi^3+B*phi^2+theta_Arad
theta_2=A*(pi-phi)^3+B*(pi-phi)^2+theta_Arad
```

```
L_1=2*zeta/(1+1/L_factor)

L_2=L_1/L_factor

ub=L_1/sin(theta_1)

ua=ub*cos(theta_1)

Xo=zeta-L_1

T_111=L_1^3*(2-3*cos(theta_1)+cos(theta_1)^3)/(3*sin(theta_1)^3)

T_112=Xo*(ub^2*theta_1-ua*ub*sin(theta_1))

T_11=T_111+T_112

yb=L_2/sin(theta_2)

ya=yb*cos(theta_2)

yc=(yb^2-Xo^2)^.5

sininv=arcsin((1-Xo^2/yb^2)^.5)

T_121=Xo^2*(yb-ya)

T_122=2/3*yb^3-2/3*yb^2*yc+Xo^2*yb-1/3*Xo^2*yc-Xo*yb^2*(pi/2-sininv)

T_1=T_11+T_121-T_122

V_1=integral(T_1,phi,0,pi/2)

T_211=yc*(2/3*yb^2+Xo^2/3)

T_212=yb^2*ya-ya^3/3

T_21=T_211-T_212

T_22=-Xo^2*yc+Xo*ya*yb*sin(theta_2)-Xo*yb^2*(sininv-pi/2+theta_2)

T_23=Xo^2*(yc-ya)

T_2=T_21+T_22+T_23

V_2=integral(T_2,phi,0,pi/2)

Vol=V_1+V_2

END
```

{--Findings maximum droplet height--}

```
SUBPROGRAM h_m(alpha_rad, theta_Arad, phi, D_max: h_max)
$COMMON rho, g, Gamma
{--Volume of a drop using the two-circle method--}
Bo=rho*g*sin(alpha_rad)*D_max^2/Gamma*1e-3 {Bo is non-dim}
theta_min_rad=( 0.01*Bo^2 - 0.155*Bo + .97)*theta_Arad
theta_min_rad=theta_min*pi /180  {radians}
Beta=1+0.096*Bo
L=Beta^.5*D_max/2
{--Theta Function---}
A=-(2*theta_min_rad-2*theta_Arad)/pi^3
B=-(3*theta_Arad-3*theta_min_rad)/pi^2
zeta=L/(cos(phi)^2+Beta^2*sin(phi)^2)^.5
L_factor=sin(theta_1)/sin(theta_2)*(1-cos(theta_2))/(1-cos(theta_1))
theta_1=A*phi^3+B*phi^2+theta_Arad
theta_2=A*(pi-phi)^3+B*(pi-phi)^2+theta_Arad
L_1=2*zeta/(1+1/L_factor)
L_2=L_1/L_factor
{Xo=zeta-L_1}
yb=L_2/sin(theta_2)
ya=yb*cos(theta_2)
h_max=yb-ya
END

SUBPROGRAM finda(alpha_rad, theta_Arad, phi, y, D: a_4 )
$COMMON rho, g, Gamma
{--Volume of a drop using the two-circle method--}
Bo=rho*g*sin(alpha_rad)*D^2/Gamma*1e-3 {Bo is non-dim}
```

```
theta_min_rad=( 0.01*Bo^2 - 0.155*Bo + .97)*theta_Arad
theta_min_rad=theta_min*pi /180  {radians}
Beta=1+0.096*Bo
L=Beta^.5*D/2
{--Theta Function---}
A=-(2*theta_min_rad-2*theta_Arad)/pi^3
B=-(3*theta_Arad-3*theta_min_rad)/pi^2
zeta=L/(cos(phi)^2+Beta^2*sin(phi)^2)^.5
L_factor=sin(theta_1)/sin(theta_2)*(1-cos(theta_2))/(1-cos(theta_1))
theta_1=A*phi^3+B*phi^2+theta_Arad
theta_2=A*(pi-phi)^3+B*(pi-phi)^2+theta_Arad
L_1=2*zeta/(1+1/L_factor)
L_2=L_1/L_factor
Xo=zeta-L_1
yb=L_2/sin(theta_2)
ya=yb*cos(theta_2)
yc=(yb^2-Xo^2)^.5
Yo=yb-L_1/sin(theta_1)
sininv=arcsin((1-Xo^2/yb^2)^.5)
h=yb-ya
R_1=yb-Yo
a_2=IF(y, h , abs((ya-Yo+y)^2-R_1^2)^0.5, 0, 0)
a_3=IF(y, h , abs((ya+y)^2-yb^2)^0.5, 0, 0)
a_4=a_2+a_3
END

SUBPROGRAM A_ice(alpha_rad, theta_Arad, y, Q_s, B_s,i1,i2: A_i )
call finda(alpha_rad, theta_Arad, 0, y,D: a_2 )
```

```
call finda(alpha_rad, theta_Arad, pi/2, y,D: a_3 )
n_s=Q_s*(D*1000)^(B_s)*1000 {number of drops per cm^2 per mm; D in mm}
A_i=integral(n_s*pi*a_2*a_3/4, D, i1, i2) {total Area of ice in mm^2/cm^2}
END

{--Finding the density at any  height delta from the cold surface--}

SUBPROGRAM rho(alpha_rad, theta_Arad, f, delta, Q_s, B_s,i1,i2: rho_fst)
{--Total volume of drops for a given portion (small/big)--}
call  A_ice(alpha_rad, theta_Arad, y, Q_s, B_s,i1,i2: A_i )
rho_fst=integral(A_i, y, f, delta) {total Area of ice in mm^2/cm^2}
END

FUNCTION rho_fun(alpha_rad, theta_Arad, f, delta, Q_s, B_s, D1, D2, x3)
{call h_m(alpha_rad, theta_Arad, phi, D_max: h_max)}
if (x3<10^(-4)) then
rho:=0
else
call rho(alpha_rad, theta_Arad, f, delta, Q_s, B_s,D1,D2: rho)
ENDIF
ENDIF
rho_fun:=rho
END

{--Inputs: surface orientation (alpha in degrees), ACA (theta_A in degrees), area ratios covered by big
and small droplets (A_cov_b, A_cov_s), water density (rho in kg/m3), Surface tension of water (Gamma in
mN/m), minimum and maximum droplet diameters (D_min, D_max), ice temperature (T_i in Celsius),
```

gravitational acceleration (g in m/s2), Total surface area (A in cm2), Coefficient of the small droplet distribution (B_s=-2.73 according to the distribution by Tanassawa)--}

{--Frost density--}

rho_i=Density(Ice,T=T_i,P=101)

call n_d(D_max, A_cov_s, A_cov_b, B_s: Q_s, Q_b, B_b)

call h_m(alpha_rad, theta_Arad, 0, D_max: h_max)

f=tablevalue(row-1,#delta)

x=tablevalue(row-1,#rho_small)

x2=tablevalue(row-1,#rho_big)

rho_s=rho_fun(alpha_rad, theta_Arad, f, delta, Q_s, B_s, D_min, 0.2*D_max, x)

rho_small=rho_s*rho_i/(delta*100)

rho_big=rho_b*rho_i/(delta*100)

rho_b=rho_fun(alpha_rad, theta_Arad, f, delta, Q_b, B_b, 0.2*D_max, D_max, x2)

rho_sum=tablevalue(row-1,#rho_sum)+rho_s+rho_b

rho_fst=(rho_sum)*rho_i/(delta*100) {kg/m^2}